الجمهورية الجزائرية الديمقراطية الشعبية

République Algérienne Démocratique et Populaire
وزارة التعليم العالي و البحث العلمي
Ministère de l'enseignement supérieur et de la recherche scientifique

Université Mohamed Khider – Biskra
Faculté des Sciences et de la technologie
Département : Génie Electrique
Ref :………………

جامعة محمد خيضر بسكرة
كلية العلوم و التكنولوجيا
قسم :الهندسة الكهربائية
المرجع : ....

Thèse présentée en vue de l'obtention
du diplôme de

Doctorat LMD en Electronique

Spécialité (Option) : **Micro-électronique, Micro-informatique et Instrumentation**

Intitulé

Numerical simulation of the performance of solar cells formed by nanostructures based on II-VI semiconductors

(Simulation numérique des performances des cellules solaires formées par des nanostructures à base des semi-conducteurs II-VI)

Présentée par :

TINEDERT Imad Eddine

Soutenue publiquement le 30/06/2022

Devant le jury composé de :

TIBERMACINE Toufik	**Professeur**	**Président**	**Université de Biskra**
SAADOUNE Achour	**Professeur**	**Rapporteur**	**Université de Biskra**
DEHIMI Lakhdar	**Professeur**	**Examinateur**	**Université de Batna**
BEKHOUCHE Khaled	**Maitre de conférences A**	**Examinateur**	**Université de Biskra**

Acknowledgement

First of all, praise is to Almighty God who has given me the strength, faith, health, courage, guidance at every step, and patience to complete this present thesis. It has been a long journey finishing this thesis, and it would have been much more difficult without the help of many excellent people.

I would like to express my sincerest gratitude to my supervisor Pr. Saadoune Achour, for his continuous support and critical guidance throughout my PhD period. Without his careful reading and constructive comments, the completion of this work would not have been possible.

Next, I would like to thank the director of the Laboratory of Metallic and Semiconductor Materials (LMSM) Pr. Tibermacine Toufik, for the best conditions he has reserved for us to finish this work and for having accepted the presidency of the jury.

Furthermore, my appreciation and thanks are extended to the rest of my thesis committee: Pr. Dehimi Lakhdar and Dr. Bekhouche Khaled, who honoured me with their acceptance to examine and read my thesis.

I will also take this opportunity to acknowledge Pr. Suleyman Ozcelik at Photonics department of Gazi University in Turkey for his warm reception and cooperation.

My greatest gratitude goes to Dr. Megherbi Mohamed Larbi at the University Mohammed Khider Biskra, Pr. Pezzimzenti Fortunato of Mediterranea University of Reggio Calabria in Italy, Pr. Bouchama Idris at University of M’sila, Pr. Saeed Mohammad Alam at the Department of Physic University of Education in Pakistan, for the many improvements they had to make and for their valuable contributions to the publication of my articles.

Obviously, I cannot close these lines without addressing my thanks to all the Electrical Engineering department staff and my colleagues.

Finally, I thank my parents, my brother, my sisters and my friends for their endless love and support that have made the hard times so much easier, as well as to everyone who helped me without exception, with a smile, with encouragement, with information, to everyone who had confidence in me and this gave me the energy to assume myself and succeed.

Dedication

This thesis is dedicated to the wonderful
persons who deserve a lot of love and respect:
To my dear parents,
إلى عمي مصطفي رحمه الله,
To my brother and sisters,
To all my teachers and administrative staff,
To all those who supported me and helped
me to get my PhD without hesitation,

Thank you very much indeed.

ملخص

في السنوات الأخيرة، إزداد استخدام الأغشية الرقيقة لأشباه الموصلات II-VI مثل CdTe و CdS في الخلايا الشمسية بشكل كبير بسبب كفاءة الجهاز العالية، والاستقرار في الأداء والتكلفة. في هذه الأطروحة، تم دراسة الخلية الشمسية CdS/CdTe بواسطة محاكاة رقمية ثنائية الأبعاد باستخدام برنامج المحاكاة TCAD Silvaco-Atlas.

في الخطوة الأولى من هذا العمل، تمت دراسة ومحاكاة هيكل مرجعي للخلية الشمسية $FTO/i\text{-}SnO_2/CdS/CdTe$ بناءً على البيانات التجريبية للتحقق من صحة المحاكاة ومدى توافق النتائج المتحصل عليها مع البيانات التجريبية. تم افتراض كتلة هوائية 1.5 طيف عالمي (AM1.5G) بإشعاع ساقط $1000\ W/m^2$ خلال عمليات المحاكاة : كفاءة التحويل التي تم الحصول عليها هي 13.96٪. تتفق نتيجة المحاكاة هذه بشكل جيد مع البيانات التجريبية المأخوذة كمرجع في هذا العمل.

في الخطوة الثانية، من أجل تحسين أداء الخلايا الشمسية CdTe، تم اقتراح هيكل جديد يتمثل في دمج طبقة أكسيد النحاس (p-type Cu_2O) عند الاتصال الخلفي كطبقة حجب إلكترونات-نقل ثقب (HT-EBL)، بهدف تقليل خسائر إعادة تركيب الناقلات الأقلية. تم الحصول على أداء عالٍ من خلال إضافة تحسين لمعلمات الخلية من حيث السماكة وتركيز التطعيم وعمر الناقل. هذه التحسينات أدت الى زيادة كفاءة الخلية بنسبة 10.35٪ مقارنة بالنتائج الأخيرة حيث تحصلنا على نسبة كفاءة التحويل 24.35٪ للهيكل الأمثل $FTO/i\text{-}SnO_2/CdS/CdTe/Cu_2O$ في درجة حرارة الغرفة (300K)، كثافة التيار للدائرة القصيرة $27.59\ mA/cm^2$، جهد الدائرة المفتوحة 1.03V وعامل التعبئة 85.83٪.

قمنا بدراسة تأثير سمك الطبقة الشفافة العالية المقاومة HRT واستخدام i-ZnO كبديل لمادة $i\text{-}SnO_2$ حيث أظهرت النتائج أن مادة SnO_2 أكثر فعالية من ZnO في جهاز الخلايا الشمسية CdTe. أخيرًا، درسنا تأثير درجة الحرارة على أداء الخلية الشمسية المثلى CdTe في المجال المحصور بين 330-270K. وقد بينت نتائج المحاكاة أن كفاءة الخلية تنخفض خطيا مع زيادة درجة الحرارة.

الكلمات المفتاحية : النمذجة، المحاكاة، الخلايا الشمسية، CdS/CdTe، ZnO ، SILVACO.

Abstract

In the recent years, the use of II-VI semiconductors thin-films like CdTe and CdS in solar cells has significantly augmented due to high device efficiency, stability in the performance, and cost-effectiveness. In this thesis, a CdS/CdTe solar cell has been investigated employing 2-dimensional numerical simulations using TCAD Silvaco-Atlas simulator.

In the first step of the work, a reference structure of FTO/i-SnO_2/CdS/CdTe solar cell was studied and simulated based on experimental data for the validity of the simulation and the extent to which present results agree with the experimental data. An air mass 1.5 global spectrum (AM1.5G) with an incident irradiance of 1000 W/m^2 was assumed during the simulations: the conversion efficiencies obtained are 13.96%. This simulation result is in good agreement with experimental data reported in the literature.

In the second step, in order to optimize CdTe solar cell performances, a new structure is proposed by incorporation of a cuprous oxide (p-type Cu_2O) layer at back-contact as a Hole transport-Electron blocking layer (HT-EBL), with the aim of minimizing the minority carrier recombination losses. High performance has been obtained by optimizing the cell parameters in terms of thickness, doping concentration and carrier lifetime. Using the optimal parameters on which the optimal structure depends, the efficiency of the structure is increased by 10.35% compared to the reference cell. The simulation results have a high conversion efficiency of 24.35%, with short-circuit current density of 27.59 mA/cm^2, an open-circuit voltage of 1.03 V and a fill-factor of 85.83%. The simulated efficiency of 24.35% was obtained for the optimized structure of FTO/i-SnO_2/CdS/CdTe/Cu_2O at room temperature (300 K).

The next step was to investigate the thicknesses of the high-resistivity transparent (HRT) layer and the use of i-ZnO as an alternative to i-SnO_2 material. The results showed that SnO_2 film is more effective than ZnO in the CdTe solar cell device. Finally, we study the influences of temperature on the optimized CdTe solar cell performance in the range 270-330 K. The simulation results have shown a linear decrease in the device's efficiency with increasing temperature.

Key words: Modeling, Simulation, solar cell, CdS/CdTe, ZnO, SILVACO

Résumé

Au cours des dernières années, l'utilisation des semi-conducteurs II-VI en couches minces tels que les CdTe et CdS dans les cellules solaires a considérablement augmenté en raison de l'efficacité élevée du dispositif, la stabilité des performances et le rapport coût-efficacité. Dans cette thèse, la cellule solaire CdS/CdTe a été étudiée en utilisant des simulations numériques bidimensionnelles à l'aide du simulateur TCAD Silvaco-Atlas.

Dans un premier temps, nous avons étudiée et simulé une structure de référence, une cellule solaire FTO/i-SnO_2/CdS/CdTe, à partir de données expérimentales pour la validité de la simulation et l'étendue dans laquelle les résultats présentés sont en accord avec les données expérimentales. Un spectre global de masse d'air 1,5 (AM1.5G) avec une irradiance incidente de 1000 W/m^2 ont été pris lors de simulations : le rendement de conversion obtenue est de 13,96 %. Ce résultat de simulation est en bon accord avec les données expérimentales obtenues dans la littérature.

Puis dans la deuxième étape, afin d'optimiser les performances de la cellule solaire CdTe, nous avons proposé une nouvelle structure par incorporation d'une couche d'oxyde cuivreux (p-type Cu_2O) au contact arrière comme couche de blocage d'électrons et transport de trous (HT-EBL), afin de minimiser les pertes de recombinaison des porteurs minoritaires. Par l'optimisation des paramètres de la cellule en termes d'épaisseur, concentration de dopage et durée de vie des porteurs, nous avons obtenu des performances élevées. A travers l'utilisation des paramètres optimaux dont dépend la structure optimale, le rendement de la structure a été augmenté de 10,35% par rapport à la cellule de référence. Les résultats de la simulation ont donné un rendement de conversion égale à 24,35 % avec une densité de courant de court-circuit de 27,59 mA/cm^2 ainsi qu'une tension en circuit ouvert de 1,03 V et un facteur de forme de 85,83 %. Le rendement de conversion simulée de 24,35 % a été obtenu pour la structure optimisée de FTO/i-SnO_2/CdS/CdTe/Cu_2O à température ambiante (300 K).

L'étape suivante était l'étude de l'effet de l'épaisseur de la couche transparent haute résistance (HRT) et l'utilisation de i-ZnO comme matériau alternatif au i-SnO_2. Les résultats ont montré que le film SnO_2 est plus efficace que le ZnO dans le dispositif de cellule solaire CdTe. Enfin, nous avons étudié l'influence de la température sur les performances de la cellule solaire optimisées dans l'intervalle 270-330 K. Les résultats de simulation ont indiqué une diminution linéaire dans le rendement de conversion de dispositif avec l'augmentation de la température.

Mots clés: Modélisation, Simulation, cellule solaire, CdS/CdTe, ZnO, SILVACO

Table of contents

CHAPTER 4: Numerical simulation results and interpretation 90

List of figures

List of tables

List of acronyms

Symbol	Explanation
CB	Conduction Band
VB	Valence Band
E_F	Fermi energy
EHP	Electron hole pair
GBs	Grain boundaries
Cd	Cadmium
Te	Tellurium
Si	Silicon
Zn	Zinc
Sn	Tin
Cu	Copper
Au	Gold
S	Sulfide
O	Oxygen
SnO_2	Tin oxide
FTO	fluorine-doped tin oxide
AZO	Aluminum doped zinc oxide
ZnO	Zinc Oxide
CdS	Cadmium sulfide
CdTe	cadmium telluride
Cu_2O	Cuprous Oxide
SLG	Soda-lime glass
ASG	Aluminosilicate glass
BSG	Borosilicate glass
TCO	Transparent conduction oxide
HRT	High-resistive transparent

i-SnO_2	Undoped Tin Oxide
i-ZnO	Undoped Zinc Oxide
HT-EBL	Hole transport-electron blocking layer
BSF	Back surface field
CBD	Chemical bath deposition
GaAs	Gallium arsenide
CIGS	Copper indium gallium selenide
CSS	Close space sublimation
MOCVD	Metal-organic chemical vapour deposition
VTD	Vapor transport deposition
PLD	Pulsed laser deposition
PV	Photovoltaic
2GEN	Second-Generation
3GEN	Third-Generation
4GEN	Fourth-Generation
DSSCs	Dye-sensitized solar cells
TCAD	Technology computer aided design
Silvaco	Silicon valley corporation
SCAPS	Solar Cell Capacitance Simulator
AMPS	Analysis of Microelectronics and Photonics Structures
AFORS-HET	Automat FOR Simulation of HETero structures
ASA	Amorphous Semiconductor Analysis
AM	Air-mass
SRH	Shockley-Read-Hall
NREL	National Renewable Energy Laboratory
AIST	Japanese National Institute of Advanced Industrial Science and Technology
SEM	Scanning electron microscope
DC	Direct current
AC	Alternative current
IR	Infrared
t_m	Thickness

List of Symbols

Symbol	Explanation	Unit
η	Conversion efficiency	%
FF	Fill factor	%
J_{sc}	Short-circuit current density	mA/cm^2
V_{oc}	Open-circuit voltage	V
P_{in}	Input power	mw/cm^2
P_m	Maximum power	mw/cm^2
ρ	Resistivity	Ω cm
σ	Conductivity	Ω^{-1} cm^{-1}
E_g	Band gap energy	eV
χ_e	Electron affinity	eV
E_{ps}	Dielectric ratio	-
μ_n	Electron mobility	$cm^2/V\,s$
μ_p	Hole mobility	$cm^2\,/V\,s$
N_v	Valence band effective density of states	cm^{-3}
N_c	Conduction band effective density of states	cm^{-3}
N_D	Donor Carrier concentration	cm^{-3}
N_A	Acceptor Carrier concentration	cm^{-3}
k	Boltzmann constant (1.38×10^{-23})	J/K
E_C	Conduction band energy	eV
E_V	Valance band energy	eV
$\boldsymbol{\tau_p}$	Hole Lifetime	ns
$\boldsymbol{\tau_n}$	Electron Lifetime	ns
B_r	Radiative recombination coefficient	cm^3/s
c	Speed of light (2.998×10^{8})	m/s
α	Absorption coefficient	cm^{-1}
n	Refractive index	-

K	Extinction coefficient	-
T	Temperature	K
EQE	External quantum efficiency	%
IQE	Internal Quantum Efficiency	%
h	Planck constant (6.626×10^{-34})	$J.s$
n_i	Intrinsic carrier concentration	cm^{-3}
E_i	Intrinsic Fermi level	eV
$\mathbf{E_F}$	Fermi level	eV
I_{diff}	Diffusion current	A
I_{drift}	Drift current	A
V_{bi}	Built-in voltage	V
λ	Optical wavelength	µm
I_{sc}	Short circuit current	A
I_{ph}	Photo-generated current	A
$\emptyset_{\mathbf{m}}$	Metal work function	eV
n	Electron concentration	cm^{-3}
p	Hole concentration	cm^{-3}
D_n	Electron diffusion coefficient	$cm^{-3}s^{-1}$
D_p	Hole diffusion coefficients	$cm^{-3}s^{-1}$
$\vec{\mathbf{J}}_{\mathbf{n}}$	Electron total current density	$mA\ cm^{-2}$
$\vec{\mathbf{J}}_{\mathbf{p}}$	Hole total current density	$mA\ cm^{-2}$
S_n	Surface recombination velocities for electrons	$cm\ s^{-1}$
$\mathbf{S_p}$	Surface recombination velocities for holes	$cm\ s^{-1}$
R	Reflectance coefficient	%
T	Transmittance coefficient	%
α	Varshni coefficient	$eV\ K^{-1}$
β	Varshni coefficient	K
R_s	Series resistance	Ω
R_{sh}	Shunt resistance	Ω

GENERAL INTRODUCTION

General Introduction

The world witnesses a huge increase in the electricity energy consumption from year to the next. Indeed, the global electricity consumption in 2020, which was estimated at 23,177 TWh, is over double what it was in 1990 [1]. This is due to a number of reasons among which are the following: increasing world's population, development of transportation systems such as hybrid electric vehicles as well as modern means of communication, which have become indispensable tools. In addition, the evolution of different industries and various other fields have also contributed to this increase. However, this increasing consumption requires increased investments in the construction of additional power stations to provide the necessary electricity. Solar PV is one of the sources of electrical energy in our daily life, and reliance on it has witnessed an exponential growth as can be seen in Figure A.1, which gives the cumulative installed Solar PV Capacity in the world from 2010 to 2020. The figure indicates that the production capacity of electricity using Solar PV has evolved from 39.2 Gigawatts (GW) to 767.2 GW (i.e., more than 700 GW).At the end of 2020 alone, the total solar PV capacity added (new installations) in the world was 145.2 GW [2], China alone 48 GW, European Union (EU) countries 19.8 GW, and the United States (USA) 19.7 GW.[2].

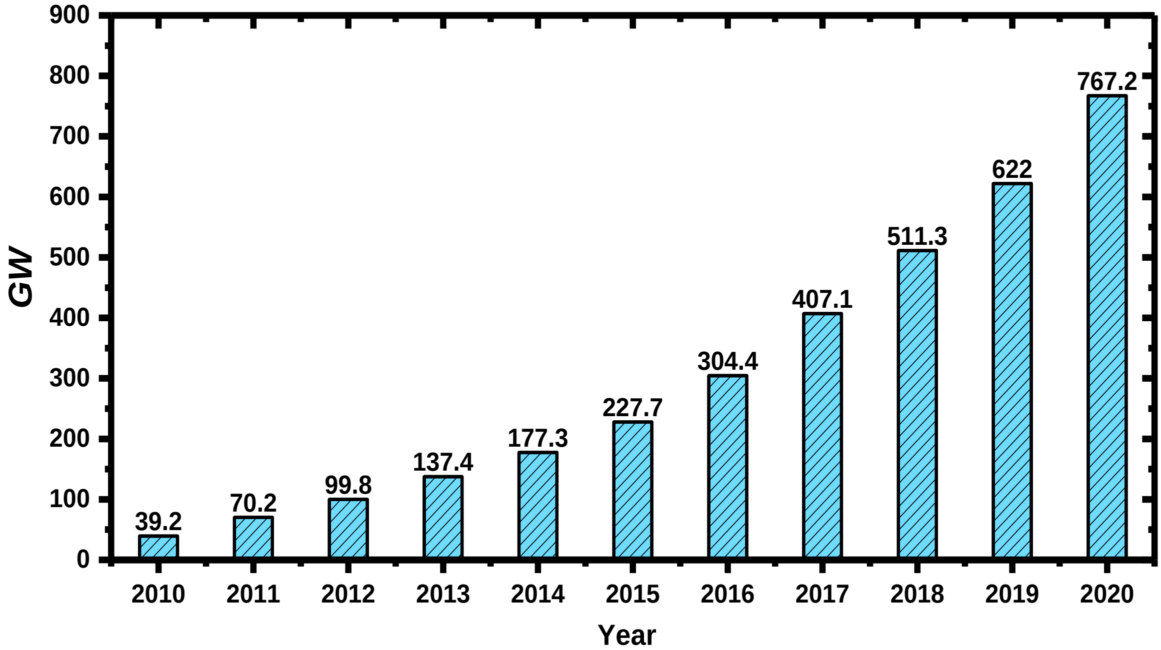

Figure A.1: Global Solar PV Capacity [2].

In general, as of 2020 the global net electricity capacity additions using various renewable energy technologies reached 200 GW, with solar PV accounting for nearly 60% of total renewable energy additions as shown in Figure A.2 (a). In light of the increasing reliance on renewable energy sources, especially solar and wind energy, the International Energy Agency (IEA) expects that in 2023 the capacity of electricity produced by wind and solar PV energy will for the first time exceed the capacity of electricity produced by natural gas, and will also surpasscoal in 2024 (see Figure A.2 (b)).

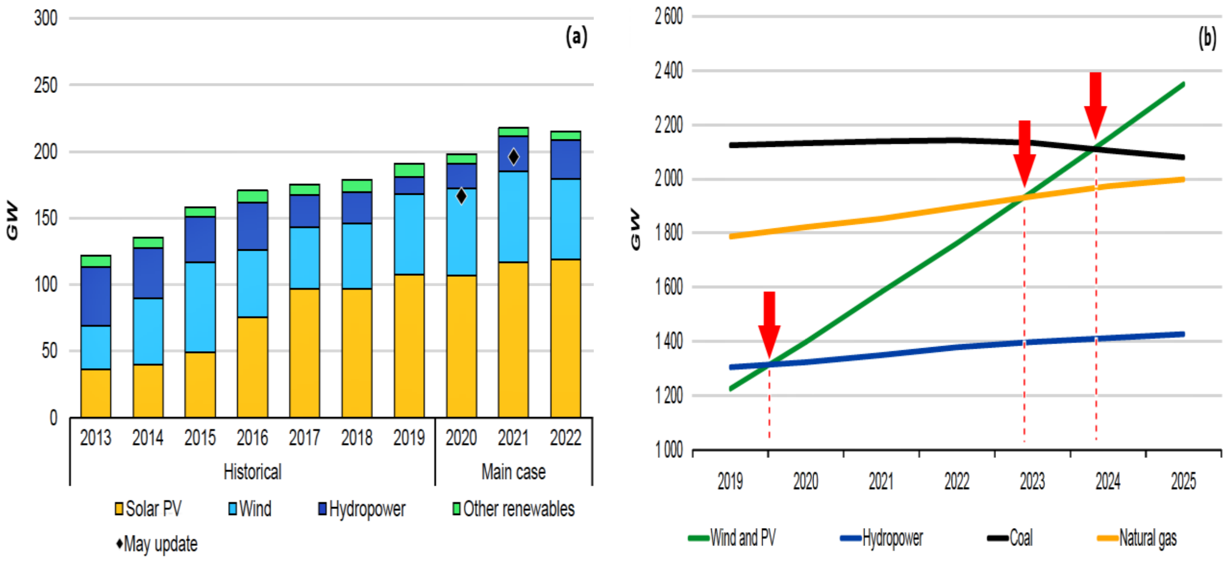

Figure A.2: (a) Renewable electricity net capacity additions by technology from 2013 to 2022, (b) Total installed power capacity by fuel and technology between 2019 and 2025 [3].

This evolution is largely due to shrinking of cost, where the solar energy produced using solar panels technology during the period from 1975 to 2020 witnessed an exponential decline in price, which decreased more than 500 times as shown in Figure A.3 where the price was equal to 105.7 USD per Watt, and decreased to about only 0.2 USD per Watt [4]. In addition to the price, the traditional energy sources such as fossil fuels (gas, coal...) are geographically limited, and will be exhausted over time. Furthermore, fossil fuels power plants have adverse effects on the environment: they contribute significantly to CO_2 emissions in the atmosphere, which lead to increased global warming, and increased risks to human health. All of these reasons explain the increased reliance on solar cells and wind at the expense of fossil fuels in general. This reality requires a transition to renewable energies that are more environmentally friendly and sustainable.

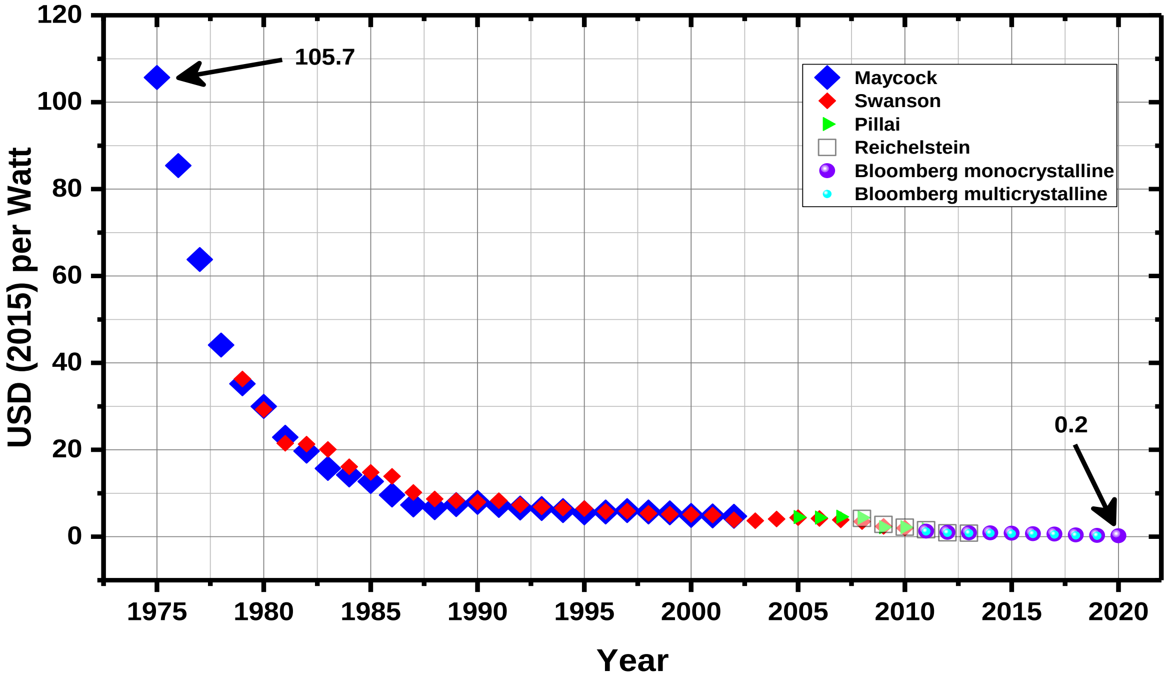

Figure A.3: Evolution of solar PV cost by data source, 1970-2020 [4].

Solar PV have the potential to meet the world's energy demands, like other renewable energy sources such as wind, biomass, hydroelectric, wave energy, and geothermal. In this context and according to the World Energy Council, the total amount of energy reaching the surface of the earth each year is 3,400,000 EJ. This is between 7000 and 8000 times the annual global primary energy consumption. If 0.1% of this energy was converted into electricity with 10% efficiency, it will provide twice the global needs of the world [5].

Despite the dominance of silicon solar cells for a long time in the market, over time and with the evolution of technology new alternatives have emerged and more effective materials have broken that dominance and become competitive in the global market. Thin-film solar cells are one of those new materials, which, beside their reduced thickness, are more economical, unlike conventional first-generation (Si) cells. II-VI compounds are one of the common thin films that are widely used, especially in the field of solar cells. The latter are advantageous due to their high absorption coefficient. Indeed, with only 1 μm of thickness, they can absorb 99% of the incoming radiation with photon energy greater than the bandgap energy. Thus, II-VI materials are very suitable for thin-film optical devices [6]. Additionally, in spectral regions where Si and III-V devices cannot provide the required bandgap, we find that the II-VI group offers a wide range of bandgap energies from 0.02 eV to 4 eV with a mainly direct band gap [7]. II-IV materials like Cadmium Telluride (CdTe) and Cadmium Sulfide (CdS) are used extensively in solar cell devices which are usually formed as a pn junction, Zinc Oxide (ZnO) thin-films are also used as transparent conducting oxide (TCO), or as High-resistivity transparent (HRT) buffer layer. There are different Thin-film solar cells commercially used such as cadmium telluride (CdTe), copper indium gallium diselenide (CIGS), and amorphous silicon (a-Si). CdTe cells are currently the thin film solar cells with the most potential that has translated into increased production in recent years, contrary to the reverse trend of other thin film technologies, as can be seen in Figure A.4. The production of CdTe modules has reached 6.1 GWp in 2020, more than that of CIGS and a-Si combined. In fact, this success is driven by high device efficiency, long-term performance stability and cost-effectiveness [8]. Since the middle of the last century, research is ongoing to find out ways to increase the efficiency of thin-film solar cells based on Cadmium Telluride (CdTe) for a better exploitation of solar energy. The great interest of this type of cells is its excellent performances. The recent studies have shown that the efficiency of this kind of cell exceeds 22% with low energy costs (~0.0387 $/kWh) [9,10].

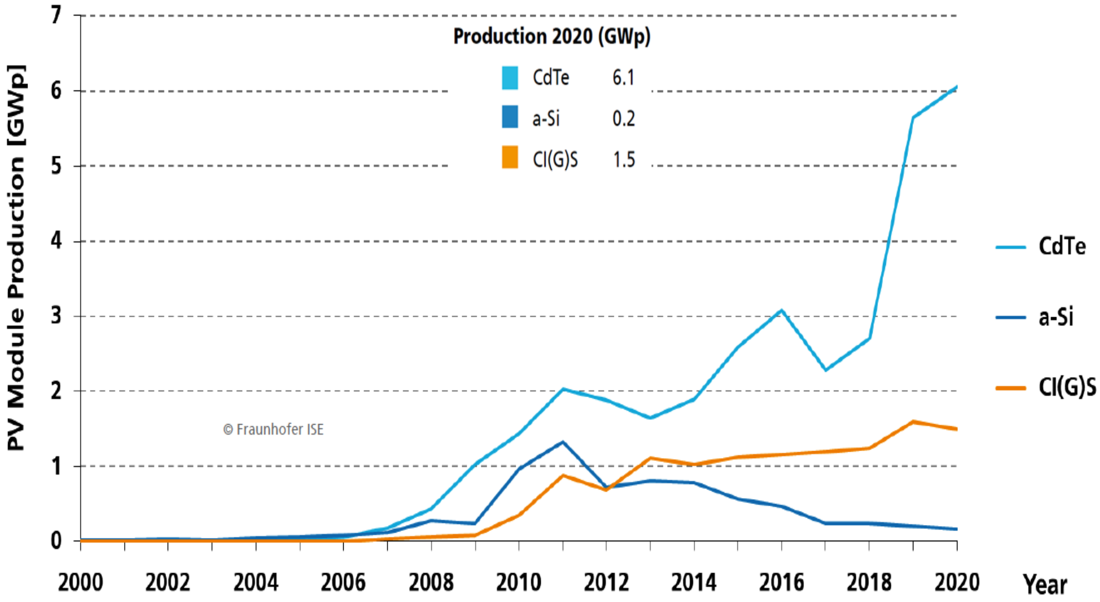

Figure A.4: Annual global Thin-Film PV module production [11].

Since the actual fabrication of solar cells requires effort, money, and time, it is useful and necessary to optimize cell performance via simulation before fabrication. Physics-based environments for modeling the semiconductor devices such as Silvaco ATLAS provide a tool to explore the photovoltaic cell design space to maximize PV cell efficiency (η) prior to device manufacturing. Therefore, this thesis is aimed at optimization of CdTe thin-film solar cells through numerical modeling by SILVACOATLAS software in order to find the technological and electrical parameters of the optimal structure that offers the best efficiency possible. In addition to investigating the effectiveness of some materials, and reducing the problems of recombination at the back contact, we propose to incorporate an interlayer at the back contact as Hole Transport-Electron Blocking Layer (HT-EBL) to help in the formation of an Ohmic contact at the back of the CdTe device.

This thesis is structured in six main parts:

The first part reviews a brief introduction of electrical energy and its consumption around the world, with a focus on renewable energy sources especially solar PV energy, as well as thin film solar cells and appraises the II-IV materials, and modeling. Finally, it presents the objectives and a structure of this thesis.

Chapter 1: This chapter consists of background information about semiconductors and p-n junctions, solar radiation and the photovoltaic effect, solar cell basics with their working principle, and the loss mechanisms in solar cells. At the end of this chapter, the different types of solar cells and the latest results reached so far are presented.

Chapter 2: Contains a description of the physical properties of II-VI semiconductors namely CdTe, CdS, and ZnO which are at the center of our thesis work, in addition toSnO_2 and CuO_2 materials. The second part of this chapter discusses the common structures of CdS/CdTe solar cells, which are used in a large fraction of current CdTe solar cells research, along with losses mechanisms in the CdS/CdTe structure and the recent methods used to reduce these losses with a particular focus on the back contact problems.

Chapter 3: The third chapter is devoted to explaining the simulation software SILVACO ATLAS and the different commands (instructions) necessary for programming in ATLAS, plus the physical models and the fundamental equations that cover the electrical behavior of a semiconductor device, with a special focus on the solar cell.

Chapter 4: In this chapter, and after presenting comparison and validation of FTO/i-SnO_2/CdS/CdTe simulated cell with an experimental cell, and to reduce problems of back contact such as recombination losses, we propose a new structure by incorporation of the cuprous oxide (p-type Cu_2O) layer at the back-contact as a hole transport-electron blocking layer (HT-EBL). To constitute the cell structure of FTO/i-SnO_2/CdS/CdTe/Cu_2O and determine the optimal parameters of the solar cell, we will show the influence of the thickness, doping concentration, and carrier lifetime of layers on the photovoltaic conversion efficiency of a

CdS/CdTe/Cu_2O cell with the aim of optimizing the cell. Also, as an alternative to the SnO_2 layer, we will investigate the effect of ZnO as an HRT layer with different thicknesses and compare both materials. Finally, we show the effect of temperature on the optimized CdTe solar cell performance.

Finally, presents an overall conclusion summarizing the work done in this thesis and the recommendations for future works intended for the further development of CdTe solar cells.

CHAPTER 1: Basics of photovoltaic cells

1.1 Introduction

In this chapter, introductory concepts and information about semiconductor materials and their basic equations are presented, and a detailed explanation is provided for the p-n junction, which is the basis of nearly every photovoltaic device. Also, among the concepts we focused on are solar radiation and the photovoltaic effect. All this to make it easier for the reader to understand how solar cells work and how sunlight is converted into electricity. After that, the equivalent diagrams of the solar cell are presented and the most important basic performance characteristics of the solar cell are reported and how they are calculated. Additionally, we illustrate the loss mechanisms in solar cells. At the end of this chapter, the types of solar cells and the latest results reached so far for each type are compiled.

1.2 Semiconductors

Any material has the ability or (lack of ability) to conduct electrical current, and on this basis, materials are classified into Metals, semiconductors, and insulators (dielectrics). The property we are talking about is conductivity σ, which is one of the important properties that we should know about a material. The opposite of conductivity is resistivity ρ that is $\rho = 1/\sigma$, where σ (Ω^{-1} cm^{-1}). The conductivity σ of different materials at room temperature spans more than 25 orders of magnitude as shown in Figure 1.1 [12]. The figure reveals that Insulator materials have a conductivity between 10^{-21} and 10^{-8} (Ω^{-1} cm^{-1}), as for Semiconductor materials, it ranges from 10^{-7} to 10^{3} (Ω^{-1} cm^{-1}) while for Metals it is in the range 10^{3} to 10^{6} (Ω^{-1}cm^{-1}).

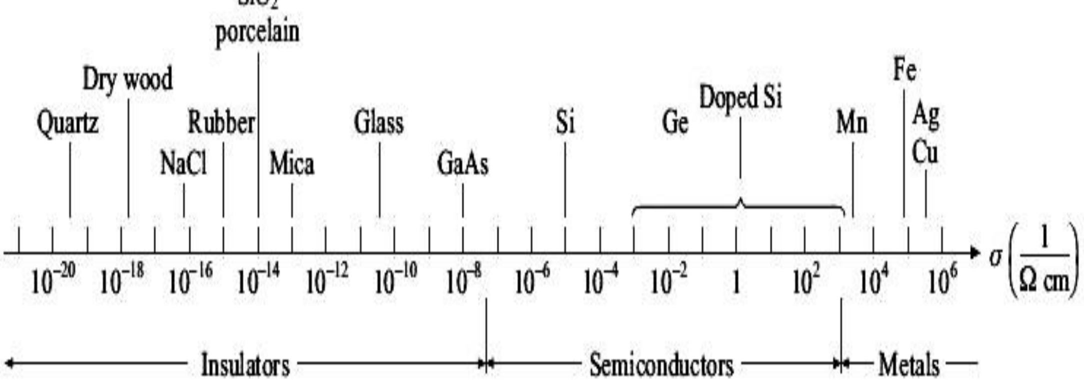

Figure 1.2: Conductivity scale of materials **[**12].

So, if we want to define semiconductors, we say it is a substance with electrical properties between those of conductors (generally metals) and those of insulators. Band theory is a quantum model in solid-state physics which gives an understanding of electrical conductivity by describing the possible energies for electrons in a solid. The schema consists of two energy bands valence and conduction band (VB and CB) and the band gap (see Figure 1.2). The valence electrons - which serve as charge carriers - are located in the valence band; in the ground state, the conduction band is occupied with no electrons. Between the two energy bands lies the band gap, and its width E_g affects the conductivity of materials.

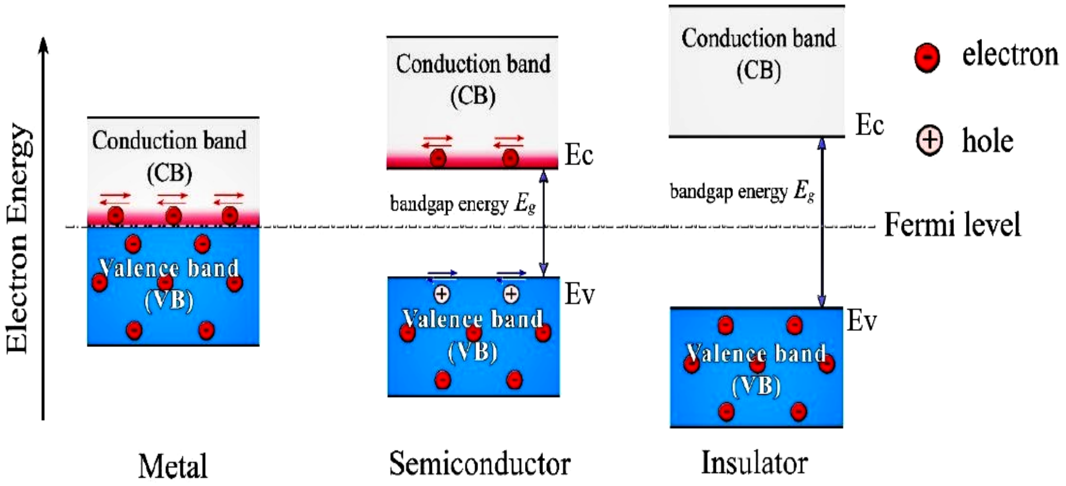

Figure 1.3: Energy Band of materials [13].

Each of these two bands (VB and CB) is characterized by a quantity that is dependent on energy E called the density of states N_v and N_c; they correspond to the space available for the holes (in the VB) and electrons (in the CB), and its mathematical equations are:

$$N_V(E) = \frac{1}{2\pi^2}\left(\frac{2m_v}{\hbar^2}\right)^{3/2}(E_V - E)^{1/2} \tag{1.1}$$

$$N_C(E) = \frac{1}{2\pi^2}\left(\frac{2m_c}{\hbar^2}\right)^{3/2}(E - E_c)^{1/2} \tag{1.2}$$

Where E is Energy [eV], E_c and E_v is Energy of (CB and VB) respectively [eV], $\hbar = h/2\pi$ with h is the Planck constant defined to have the exact value of 6.626×10^{-34} [$J.s$] and m_c, m_v is the Effective mass for density of states in CB and VB, respectively [Kg].

1.2.1 Fermi-Dirac statistics

Electrons in thermal equilibrium at temperature T with a semiconductor lattice obey Fermi-Dirac statistics. That is the probability $f(E)$ that an available electron state with energy E is occupied by an electron [14], where it takes on the form of:

$$f(E) = \frac{1}{1+e^{(E-E_F)/KT}} \qquad (1.3)$$

Where E_F is a spatially independent reference energy known as the Fermi level [*eV*], k is Boltzmann's constant equal 1.38×10^{-23} [$J.K^{-1}$] and T is the absolute temperature [*K*].

The kinetic energy of the electron increases as the temperature is augmented; some energy levels, are occupied which were vacant at absolute zero, and some levels are vacant which were occupied at absolute zero Figure 1.3.

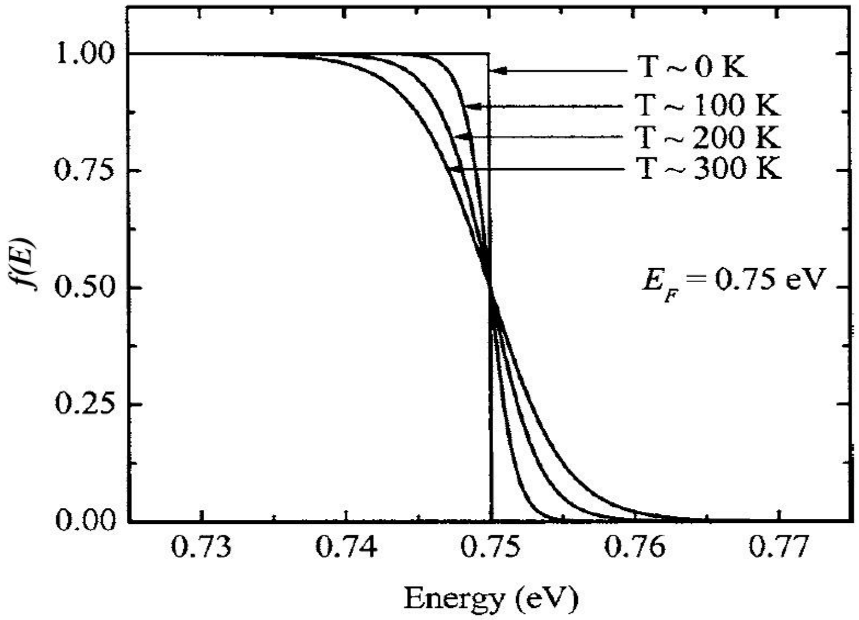

Figure 1.4: Fermi-Dirac function plotted as a function of energy for four different temperatures [15].

1.2.2 Direct and Indirect semiconductors

Knowledge of the nature of the band gap of semiconductor materials is essential for the selection of the appropriate material for many electronic devices, solar cells, and lasers...

Semiconductors are divided in terms of band gap into materials that have a direct band gap and others that have an indirect one. Direct band gap materials include CdTe, InAs, GaAs, and CIGS whereas in direct band gap materials comprise Si, Ge, and AlSb. The minimal-energy state in the

CB and the maximal-energy state in the VB are each distinguished by a certain crystal momentum (*p*-vector) in the Brillouin zone. When the crystal momentum *p*-vectors are different, the material has an "indirect gap" (see Figure 1.4 (a)). In this case, a photon cannot be emitted and this is due to the fact that the electron should pass through a middle state and transfer momentum to the crystal lattice. And, if the *p*-vectors of electrons and holes is the same in both the CB and the VB, the material has a "direct gap" (see Figure 1.4 (b)); an electron can directly emit a photon [16].

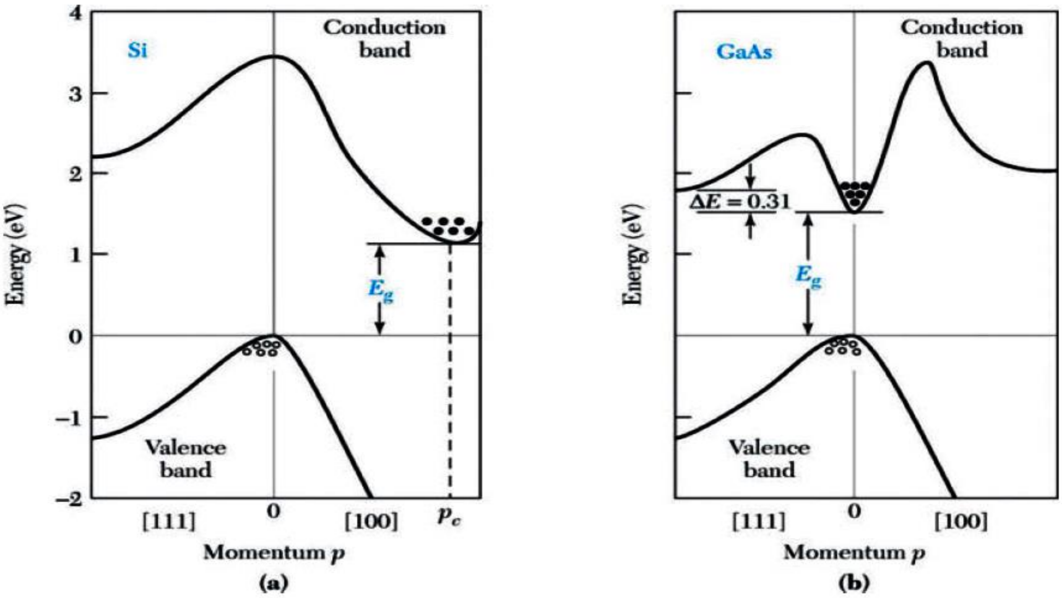

Figure 1.5: Energy band structures of (a) Si and (b) GaAs [17].

1.2.3 Types of semiconductors

1.2.3.1 Intrinsic semiconductors

An intrinsic semiconductor, also called an undoped semiconductor or i-type semiconductor, is a pure material to which no impurities were added to change the carrier concentrations. In this case, the number of electrons in the CB is equal to the number of holes in the VB. In fact, there are no pure substances without impurities in nature but is called intrinsic semiconductors to those containing relatively small amounts of impurities compared with the thermally generated electrons and holes.

The carrier concentration is said to be in the thermal equilibrium condition, when it is instable-state condition at a given temperature without any external excitations such as electric field, illumination or a pressure. At a given temperature, continuous thermal agitation results in the excitation of electrons from the VB to the CB and leaves an equal number of holes in the VB (creates free carriers). The concentration of carriers that created is called the intrinsic carrier concentration, denoted by n_i. In this case of intrinsic $n=p=n_i$, where n and p are the number of electrons in the CB and the number of holes in the VB respectively and calculate by relations (1.4) and (1.5):

$$n = N_C e^{\left(-\frac{E_C - E_F}{KT}\right)} \tag{1.4}$$

$$p = N_v e^{\left(-\frac{E_F - E_V}{KT}\right)} \tag{1.5}$$

The n_i is obtained from Eq (1.6), (1.7)

$$np = n_i^2 \tag{1.6}$$

$$n_i^2 = N_C N_v e^{\left(-\frac{E_g}{KT}\right)} \tag{1.7}$$

Where $E_g = E_c - E_V$

Also, in this case, the E_F equal to

$$E_F = \frac{E_C + E_V}{2} + \frac{KT}{2} \ln\left(\frac{N_C}{N_V}\right) = E_i \tag{1.8}$$

To clarify further, Figure 1.5 shows schematically from left to right the band diagram, the density of states, which varies as E for a given electron effective mass, the Fermi-Dirac function, and the carrier concentrations for an intrinsic semiconductor.

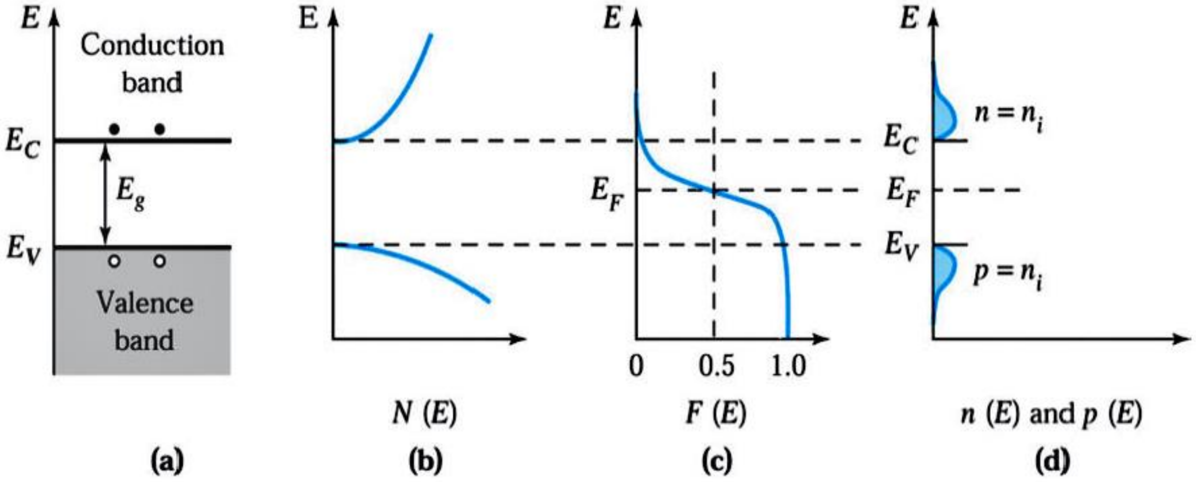

Figure 1.6: Intrinsic semiconductor (a) Schematic band diagram (b) Density of states, (c) Fermi-Dirac function, (d) Carrier concentration [17].

1.2.3.2 Extrinsic semiconductors

Intrinsic semiconductors do not conduct current well and are of limited value in their intrinsic state. Intrinsic semiconductor must be modified by increasing the number of free electrons or holes to increase their conductivity and make it useful in electronic devices. This is achieved by adding impurities to intrinsic semiconductors. This operation, called doping, consists in increasing the numbers of current carriers (holes or electrons) and thereby rendering the semiconductor extrinsic. In this state, if the number of electrons is increased in CB, we say that it is n-type doping; forming the n-type semiconductor, but if the number of holes is increased in VB, it is called p-type doping; forming the p-type semiconductor.

1.2.3.2.1 N-type semiconductor

To increase the number of CB electrons in intrinsic material, pentavalent impurity atoms are added. These are atoms with five valence electrons such as antimony (Sb), phosphorus (P), arsenic (As), etc. For example, in a pure (intrinsic) Si or Ge semiconductor, each ionic core consists of a nucleus surrounded by four valence electrons. If one of the atoms in the semiconductor lattice is replaced by an element with five valence electrons, such as antimony (Sb), as illustrated in Figure 1.6 (a) below. In this case, four of the antimony atom's valence electrons are used to form the covalent bonds with silicon atoms, leaving one extra electron. This extra electron becomes a conduction electron because it is not involved in bonding. Since the pentavalent atom gives up an electron, it is often called a donor atom, and it is called an N-type semiconductor relative to the negative charge of the free-electron. The number of conduction electrons (MAJORITY CARRIERS) can be carefully controlled by the number of impurity atoms added to the silicon.

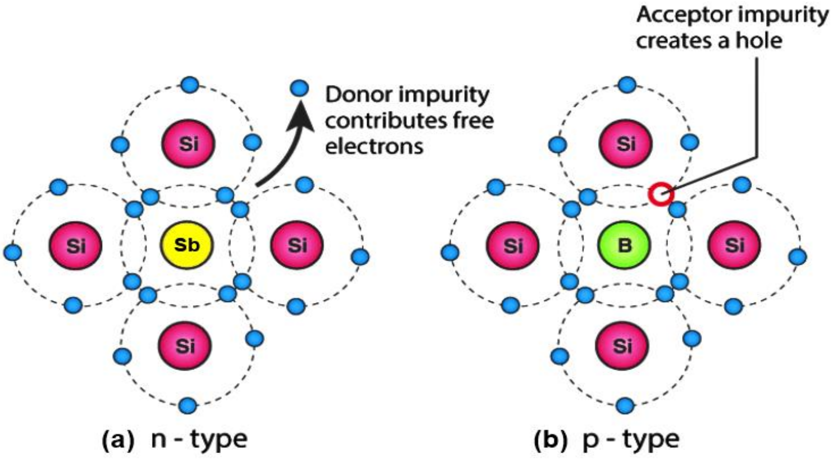

Figure 1.7: Classification of Extrinsic Semiconductor [18].

In this case $$n = N_D \tag{1.8}$$

Where N_D is the donor concentration and from Eqs (1.6), (1.8)

$$p = \frac{n_i^2}{N_D} \tag{1.9}$$

Also from Eq (1.4), (1.8) the Fermi level equal

$$E_C - E_F = KT\ln\left(\frac{N_C}{N_D}\right) \tag{1.10}$$

In addition, from Eq (1.11) we obtain the expression of electron densities in terms of intrinsic carrier concentration n_i and intrinsic Fermi level E_i

$$n = N_D = n_i e^{\frac{E_F - E_i}{KT}} \quad \text{or} \quad E_F - E_i = KT\ln\frac{N_D}{n_i} = \Delta E_n \tag{1.11}$$

Figure 1.7 illustrates the procedure for getting the carrier concentrations for an n-type semiconductor. This figure is similar to that shown in Figure 1.5. Nevertheless, the Fermi level is nearer to the bottom of the CB, and the electron concentration (upper shaded area) is far wider than the hole concentration (lower shaded area).

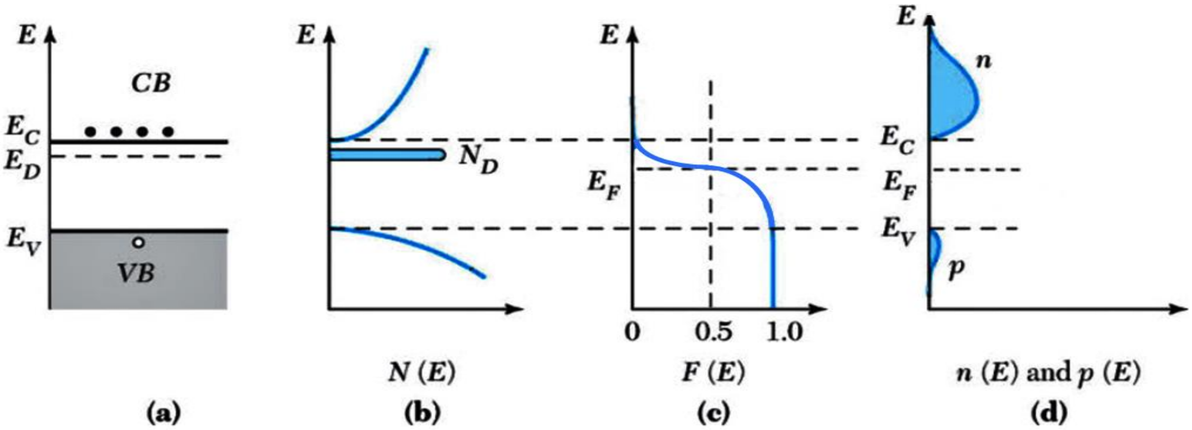

Figure 1.8: N-Type semiconductor (a) Schematic band diagram, (b) Density of states, (c) Fermi-Dirac function, (d) Carrier concentration [17].

1.2.3.2.2 P-type semiconductor

In addition to replacing one of the lattice atoms with a pentavalent atom, we can also replace it by a trivalent atom, such as indium (Tin), gallium (Ga), boron (B), etc. In this case, this impurity will only be able to contribute three valence electrons to the lattice, therefore leaving one excess hole (see Figure 1.6 (b)). Because the trivalent atom can take an electron, it is often referred to as an acceptor atom and it is called a P-type semiconductor relative to the positive charge of an excess hole. The number of holes (MAJORITYCARRIERS) can be carefully controlled by the number of trivalent impurity atoms added.

In this case
$$p = N_A \tag{1.12}$$

Where N_A is the acceptor concentration and from Eq (1.6), (1.12)

$$n = \frac{n_i^2}{N_A} \tag{1.13}$$

Also from Eq (1.5), (1.8) the Fermi level equal

$$E_F - E_V = KT \ln\left(\frac{N_V}{N_A}\right) \tag{1.14}$$

We can also by Eq (1.15) obtain the formula of hole densities in terms of intrinsic carrier concentration n_i and intrinsic Fermi level E_i

$$p = N_A = n_i e^{\frac{E_i - E_F}{KT}} \quad \text{or} \quad E_i - E_F = KT \ln\frac{N_a}{n_i} = \Delta E_p \tag{1.15}$$

Figure 1.8 illustrates the procedure for obtaining the carrier concentrations for a p-type semiconductor. This figure is similar to that shown in Figure 1.5. However, the Fermi level is closer to the top of the VB, and the hole concentration (lower shaded area) is far wider than the electron concentration (upper shaded area).

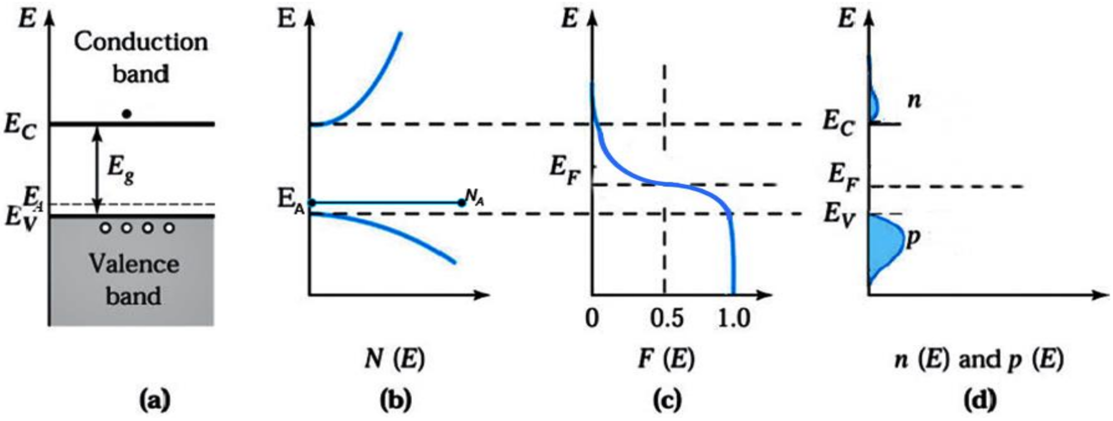

Figure 1.9: P-Type semiconductor (a) Schematic band diagram, (b) Density of states, (c) Fermi-Dirac function, (d) Carrier concentration [17].

1.2.3.3 Degenerate semiconductor

In the previous explanation we presented, we have assumed that the electron or hole doping concentration (N_D or N_A)is much lower than the effective density of states in the conduction band or the valence band (N_C or N_V), respectively. In this case, we found that the Fermi level was close to the majority carrier band. But when the doping concentration becomes greater (very heavily doped), the corresponding effective density of states E_F will be above E_C for n-type and below E_V for p-type. Thus, this type is called degenerate semiconductors. Also, a high level of doping concentration results in a lower band gap [19].

1.3 p-n junction

The p-n junction resulting from the juxtaposition between n- and p-type semiconductors is the basis for all modern transistors and nearly all photovoltaic devices. So, to comprehend these devices we require a basic understanding of the p-n junction. In order to explain the behavior of the p-n junction, we suppose that both the n- and p-type semiconductors have just been combined, free electrons diffuse from the n-type side to the p-type side and leave many positive donor ions (N_D +) in the neighborhood of the junction. Similarly, holes from the p-side diffuse into the n-side and leave the negative acceptor ions (N_A –) in the junction neighborhood [20]. To illustrate the image well, see Figure 1.9.

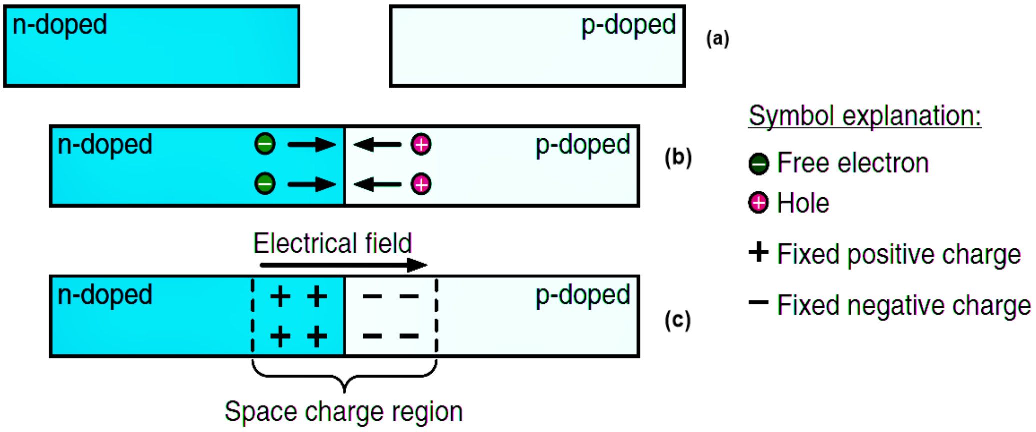

Figure 1.10: (a) The n- and p-type semiconductors before jointing, (b) At the instant of junction formation, electrons diffuse from the n-type side to p-type side, and similarly holes diffuse from p-type side to n-type side, (c) a negative space charge forms near the p-side of the junction and a positive space charge forms near the n-side; they create a space charge zone [20].

Because of the rising number of superfluous fixed charges (N_D+ and N_A –) in the junction region, a space charge region eventually comes into existence. This space charge region creates an electric field that is directed from the positive charge toward the negative charge, as indicated in the upper illustration of Figure 1.9. Lastly, a new balance is built up in which the drift current induced by the electric field (I_{drift}) exactly cancels the diffusion current (I_{diff}) of electrons and holes [20]. The electrostatic potential difference resulting from the electric field is called the built-in voltage V_{bi}. If we want to know the relationship of V_{bi}, we go back to the basis n and p semiconductor where Figure 1.10 (a) shows the energy band diagram with the Fermi level equation for both types as mentioned previously.

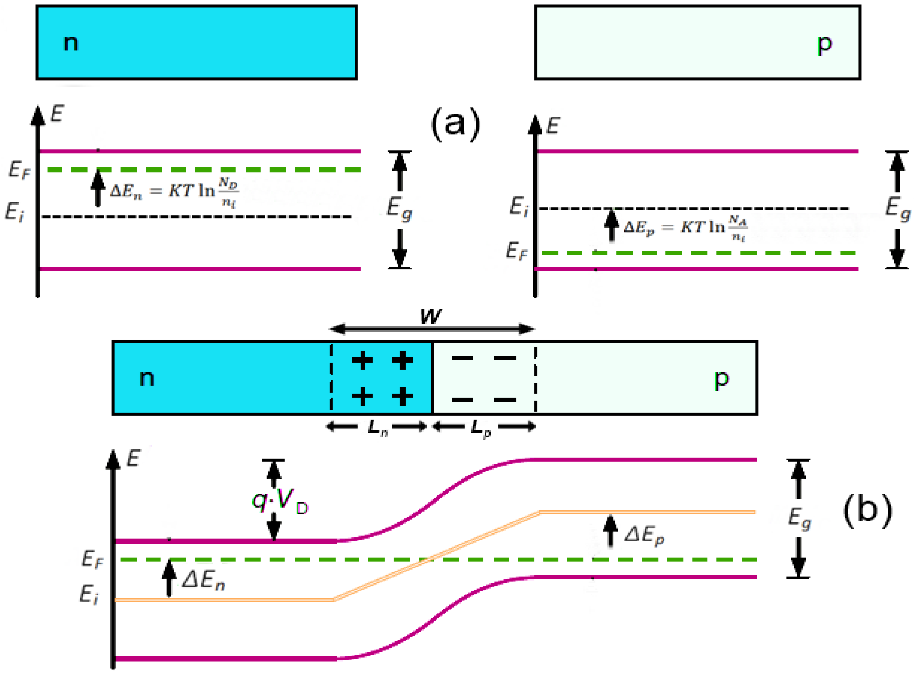

Figure 1.11: (a) the energy band diagram of n- and p-type semiconductors separated, (b) The energy band diagram of p and n linked [20].

After linking the p and n-type, the energy band diagram shape becomes like the one shown in Figure 1.10 (b). From this picture we note:

$$qV_{bi} = \Delta E_n + \Delta E_p \tag{1.15}$$

So, from Eq (1.11), (1.14) and (1.15) we deduce

$$V_{bi} = \frac{KT}{q} \ln \frac{N_D N_A}{{n_i}^2} \tag{1.16}$$

As for the total depletion layer width is [17]:

$$W = L_n + L_p = \sqrt{\frac{2\varepsilon_s}{q} V_{bi} \left(\frac{N_D + N_A}{N_D N_A}\right)} \tag{1.17}$$

The total current in p-n junction is zero at equilibrium $I_T = I_{diff} - I_{drift} = 0$, where $I_{diff} = -I_{drift} = I_s = I_0\, e^{\frac{V_{bi}}{V_T}}$ and the V_T is the Thermal voltage $\frac{KT}{q}$ [21].

Figure 1.11 depicts the form of space-charge distribution due to fixed ionized dopants and by the integration of the Poisson equation. We get the electric field distribution also with a second integration step, which results in the electrostatic potential of p-n junction under equilibrium.

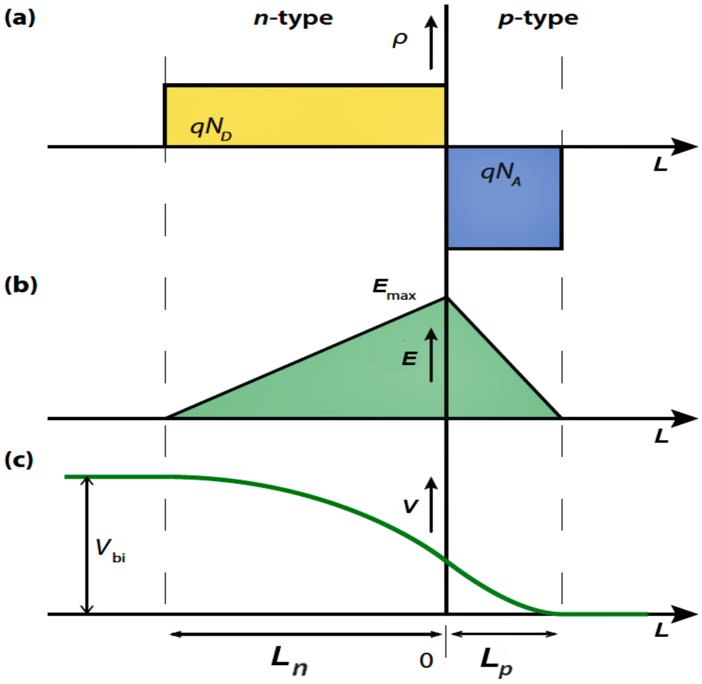

Figure 1.12: (a) A space-charge distribution due to fixed ionized dopants, (b) Electric field distribution, (c) Electrostatic potential [22].

1.3.1 The p-n junction under applied voltage

1.3.1.1 The forward-biased p-n junction

If we apply an external voltage source V to the p-n junction, where the positive terminal of the voltage source is connected to the p region and the negative is connected to the n region (see Figure 1.12 (a)). The negative side of the voltage source pushes the free electrons in the n region toward the pn junction. The same applies for the positive side, where the voltage pushes the holes toward the pn junction. As a result, the number of positive and negative ions presents in the space charge region decreases, hence the barrier decreases and with increasing voltage it reaches a limit where it finally completely fades. Then from this point on, the current I_d can flow. The voltage required for this point is compatible with the diffusion potential V_{bi} and thus this situation is called a p-n junction under a forward bias voltage. The relationship of current to external voltage becomes as follows:

$$I_D = I_S \left(e^{\frac{V_{bi}}{V_T}} - 1 \right) \tag{1.18}$$

(a) Forward voltage

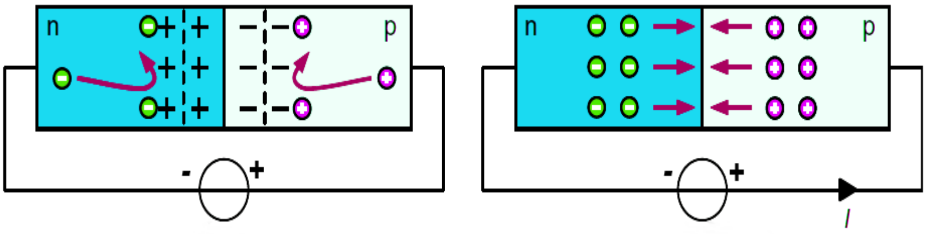

(b) Reverse voltage

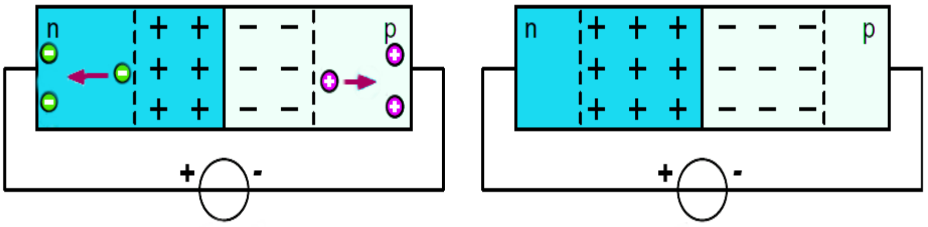

Figure 1.13: P-N junction behavior under applied external voltage: (a) when the external voltage V rises, the space charge zone W decreases until it finally fades and a current can flow, (b) In the case of reverse voltage, the space charge zone expands and therefore the current does not flow [20].

1.3.1.2 The reverse-biased p-n junction

The reverse-biased p-n junction is completely opposite of the forward bias so that the negative side of the voltage source is connected to the p region while the positive is connected to the n region (see Figure 1.12 (b)). In this case, because of the external voltage, the electrons of the n region will flow toward the positive terminal of the external voltage source and leave the positive ions in their place. As for the p region, the electrons flow from the negative terminal of the external voltage source and enter the P region. Then, these electrons move directly to combine with holes. Each occupied hole then becomes a negative charge ion. Due to the ions positive and negative that have been created, the width of the space charge region W increase and expands further with increasing external voltage until the potential across the space charge region equals the external voltage. After that, the transition current essentially stops except for a very weak reverse current I_S caused by the minority carriers in the n and p regions that are produced by thermally generated electron-hole pairs [23]. The equation of this reverse current is:

$$I_s = A.\left[\frac{q.n_i^2.D_n}{L_n N_A} + \frac{q.n_i^2.D_p}{L_p N_D}\right] \tag{1.19}$$

Where D_n , D_p is $\frac{KT}{q}\mu_n$, $\frac{KT}{q}\mu_p$ respectively and μ_n , μ_p is mobility of electrons and holes.

1.4 Solar radiation

The Sun is considered the closest star to the planet earth that we live on, and it is also at the center of the Solar System. A surface area of the sun is 1,200 times greater than that of earth, and the average distance between them is estimated at 149.6 million km. Hence, by light speed, it takes about 8 min 19 s for sunlight to reach the Earth. The solar continuously radiates an amount of P_{Sun}= 3846 .10^{23} (W) in all directions of which the Earth only receives only a little part. The radiation outside the Earth’s atmosphere is called the solar constant and has an estimate of 1367 $W.m^{-2}$.

Energy is emitted from the Sun's center to the outer regions in the form of electromagnetic radiation. This radiation is spread in the form of electromagnetic waves, and a particle of the electromagnetic radiation is known as a photon. According to Planck’s-Einstein, The energy associated with a single photon is given by $E = h.v$, where E is the energy, h is Planck's constant ($h \approx 6,626 \ . \ 10^{-34}$ J s), and ν is the frequency of the radiation (Hz). Frequency is related to wavelength by $v=c/\lambda$, where c, the speed of light, is $2,998.\ 10^8\ m.s^{-1}$. Thus, the energy of a photon has the wavelength λ is given by:

$$E = \frac{h.c}{\lambda} \tag{1.20}$$

The spectrum changes when sunlight passes through the atmosphere, and there are various reasons for this, including the reflection of light in the atmosphere and the absorption of light by molecules (CO_2, O_2, O_3, H_2O...). The longer is the path of sunlight passing through the atmosphere, the greater is the effect. Indeed, the latter translates into increased attenuation. To take into account the thickness of the atmosphere crossed by the solar radiation, the term:

$$AM = \frac{1}{\cos\theta} \tag{1.21}$$

Represents the air mass the sunlight travels through during the day. The air mass depends only on the zenith angle θ determined by the latitude, which is dependent on the trajectory of the sun. Figure 1.13 shows the principle:

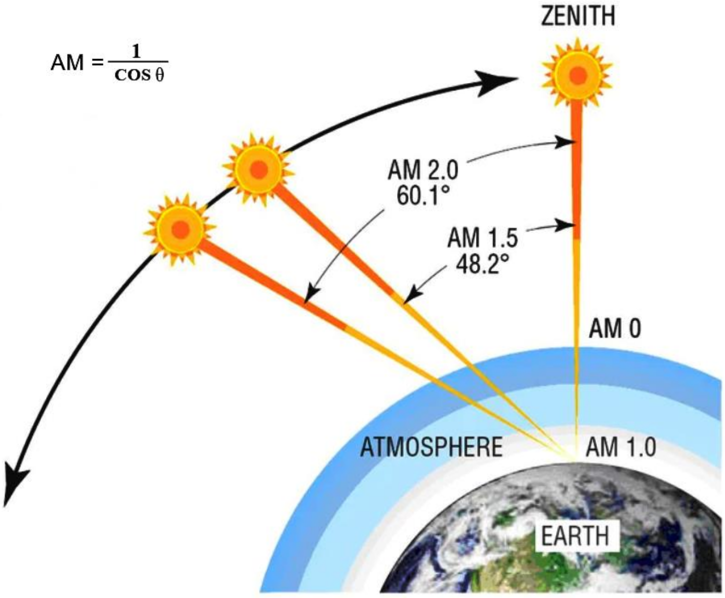

Figure 1.14: Explanation of the term Air Mass [24].

From Figure 1.13, AM0 is a reference to the radiation outside the atmosphere and the air mass is zero in this case. AM1 indicates the radiation when the sun is directly overhead and passes through the atmosphere at its exact thickness. AM1.5 is a reference to the radiation with a typical solar spectrum and is the standard usually used to characterize solar cells, where its angle in this case is 48.2^0. The letters D and G denote the direct radiation (does not include scattering) and the global radiation, respectively. The latter includes both direct and diffuse radiation as well as the radiation reflected by the external environment (the land or the sea). The direct AM1.5D radiation of 900 $W.\ m^{-2}$ and the global AM1.5 G radiation of 1000 $W.m^{-2}$ are shown in Figure 1.14, in addition to the AM0, which is the already-mentioned solar constant.

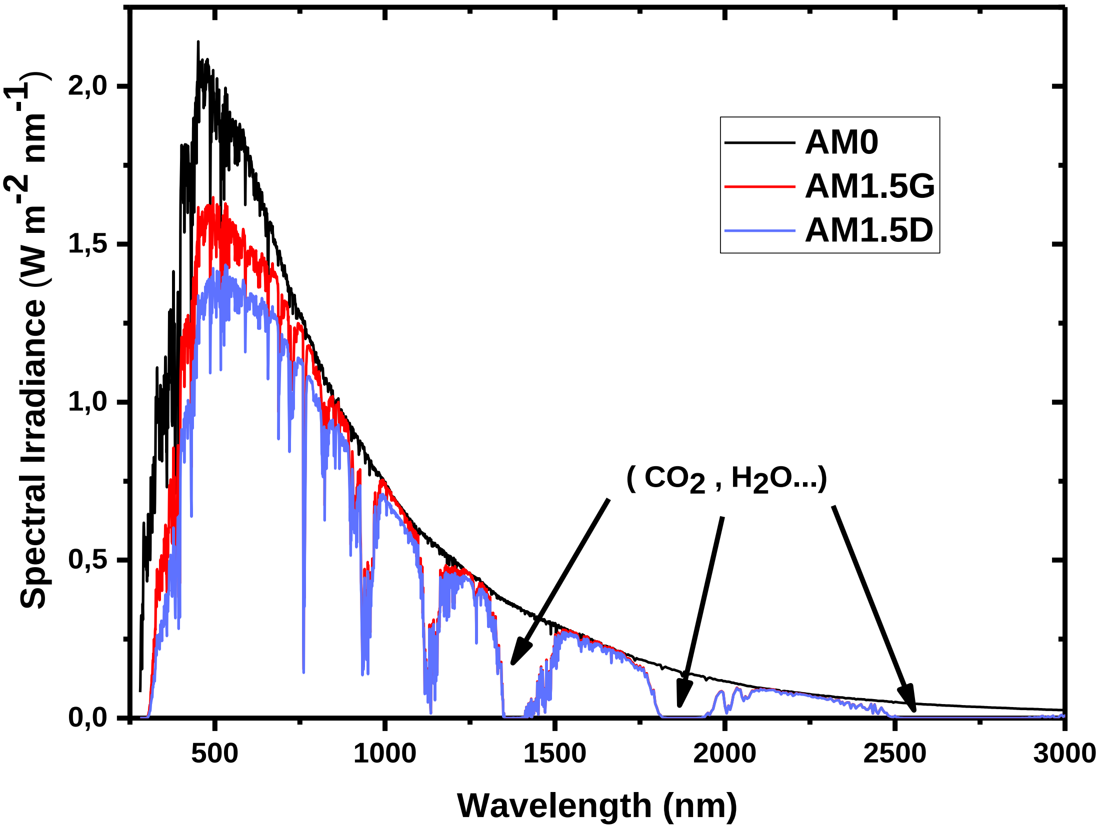

Figure 1.15: The solar spectrum AM0, AM1.5G (Global) and AM1.5D (Direct), obtained by the standard ASTM G173-03 at 37° [25].

1.5 Photovoltaic solar cells

1.5.1 Photovoltaic effect

The history of the discovering the photovoltaic effect dates back to 1839 by the French physicist Alexander Edmond Becquerel. When experimenting with electrolyte and platinum electrodes, he recognized that conductance increases when light struck the electrode. After that, Willoughby Smith appeared in 1873 and described the effect of illumination on selenium during the passage of an electric current where he also observed that the conductivity of the selenium rods augmented significantly under sunlight. Albert Einstein described the phenomenon in 1904. The first silicon mono-crystalline solar cell was constructed in 1941. In 1951, the first practical germanium solar cells were made. Bell's Laboratories reported the results of the solar cell operation with 4.5% efficiency [26].

The photovoltaic effect is a process of converting the energy of sunlight (photons) into electrical energy in some semiconductors. When the incident radiation in the form of photons reaches the material, the material absorbs the photons, which have more energy than their bandgap ($E_{photon} \geq Eg$).The absorbed photons cause electron-hole pairs (EHP) to be generated in the material, and then these electrons jump to the CB and become free. If these electron-hole pairs are not separated, their recombination occurs again very fast, resulting in a phonon release, depending on the energy absorbed [17,21]. The photo-generated EHP separation is achieved by differing carrier conductivities in the collectors adjacent to the absorber, and this property is available in the PN junction (the basic constituent of a solar cell): n- and p- doped regions serve as electron and hole collectors, respectively, enabling electron (hole) transport to the negative (positive) terminal, while inhibiting hole (electron) transport to the negative (positive) terminal (and thus limiting the recombination of electron/hole) [27].

1.5.2 P-N junction under illumination

Most solar cells are essentially p-n junctions. When light shines on it, penetrating photons are absorbed and generate free EHP (see Figure II.15). Hence the concentration of minority carriers in the n and p regions strongly increases in this situation, and this leads to the flow of the minority carriers across the depletion region toward the quasineutral regions. Electrons move from the p-type into the n-type region, and holes from the n-type to the p-type region. The movement of the photo-generated carriers causes the so-called photo-generation current I_{ph}, which adds to the thermal-generation current I_{gen}.

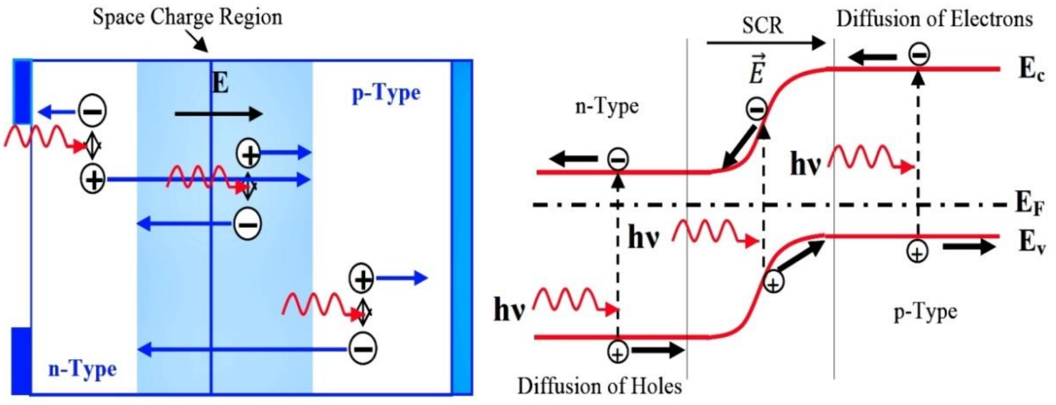

Figure 1.16: P-N junction under illumination (left) and the energy band diagram (right) [28,29].

When a load is linked between the electrodes of the illuminated p-n junction, some part of the photo-generated current will flow into the external circuit. The potential difference between the n- and p-type regions will be minimized by a voltage drop over the load. Furthermore, the electrostatic potential difference over the depletion region will also be diminished, which results in an increase in the recombination current [26]. As for the junction in the case of an open circuit, no net current can flow inside the p-n junction; thus, the current resulting from the flux of photo-generated and thermally generated carriers is balanced by the reverse recombination current.

1.5.3 Electrical characteristics of solar cells

1.5.3.1 The ideal solar cell

As a solar cell has similar properties to a diode, when a solar cell is not illuminated (in case dark), it will act as a diode. The current relationship of a solar cell can be expressed by the Shockley equation:

$$I = I_S \left(e^{\frac{qV}{K_B T}} - 1\right) \tag{1.22}$$

Where I is the cell current, I_S is the reverse saturation current, q is the electron charge (1.6×10^{-19} C), V is the voltage at the terminals of the cell, k_B is the Boltzmann constant (1.38×10^{-23} JK^{-1}), T is the absolute temperature. The simplified electrical equivalent model of the ideal solar cells consists of a direct current source connected in parallel with a diode as manifested in the equivalent circuit of Figure 1.16.

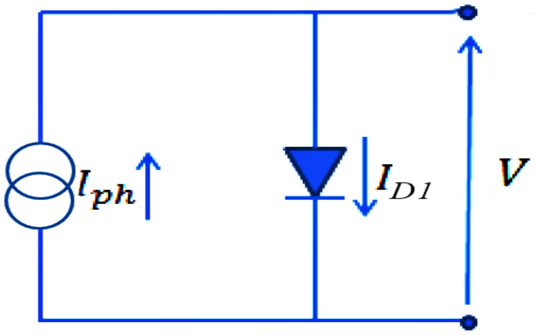

Figure 1.17: The equivalent circuit of an ideal solar cell [30].

The corresponding electrical behavior of the solar cell can be expressed by the Shockley equation (1.22) in combination with the photo-generated current:

$$I = I_{ph} - I_{D1} = I_{ph} - I_S \left(e^{\frac{qV}{K_B T}} - 1\right) \tag{1.23}$$

The dark and illuminated *I-V* characteristics of the solar cell are represented in Figure 1.17. Note that the superposition principle is reflected in Figure 1.17. The illuminated *I-V* characteristic of a solar cell is the same as the dark *I-V* characteristic (diode characteristic), but it is shifted down by the photo-generated current I_{ph}.

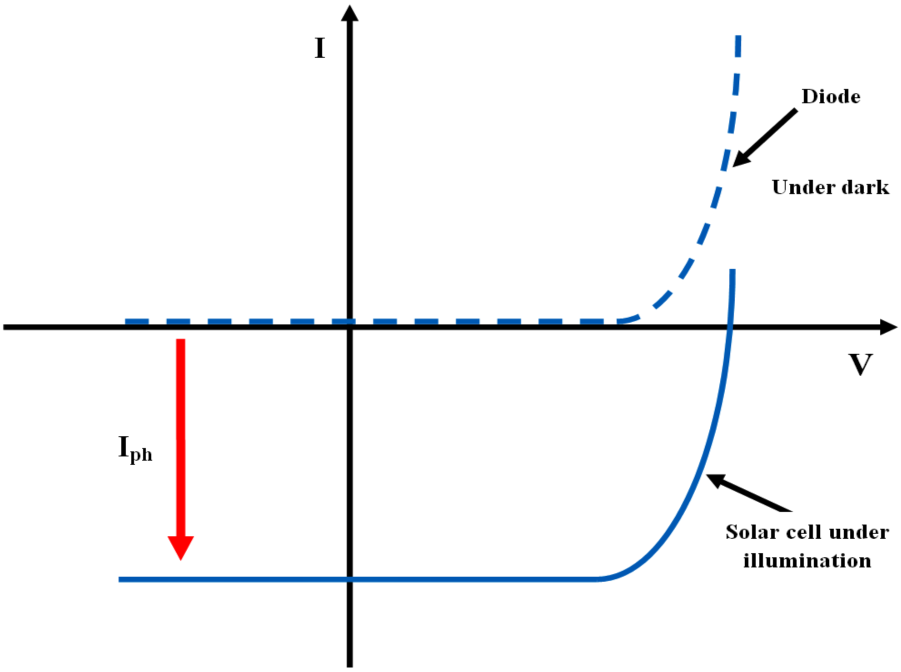

Figure 1.18: The dark and illuminated *I-V* characteristics of the solar cell [30].

1.5.3.2 Solar cell in practice

In fact, in practice no solar cell is ideal. So, we always find that the electrical characteristics of a solar cell in practice usually differ to some extent from the ideal characteristics. Therefore, the real model delves deeper into electrical losses in the solar cell. The non-ideal equivalent circuit of a solar cell is shown in Figure 1.18.

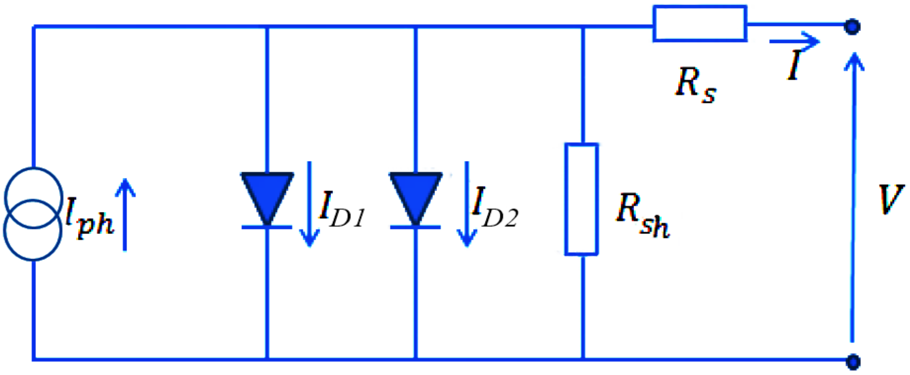

Figure 1.198: The equivalent circuit of a non-ideal solar cell [30].

In this case, one makes use of the two-diode model in which the diffusion current is modeled by means of a diode with an ideality factor of 1 and a recombination current through an additional diode with an ideality factor of 2. Also, the series resistance R_S describes especially the ohmic losses in the front contacts of the solar cell and at the metal-semiconductor interface. Conversely, leak currents at the edges of the solar cell as well as any point short-circuits of the p-n junction are modeled by the shunt resistance R_{Sh} [20]. So, the current relationship of the solar cell becomes as follows [30]:

$$I = I_{ph} - I_{D1}\left(e^{\frac{V+I.R_S}{K_B T}} - 1\right) - I_{D2}\left(e^{\frac{V+I.R_S}{2K_B T}} - 1\right) - \frac{V+I.R_S}{R_{Sh}} \tag{1.24}$$

The influence of the series and parallel resistances, on the *I-V* characteristic of the solar cell is shown in Figure 1.19 (a) and (b), respectively.

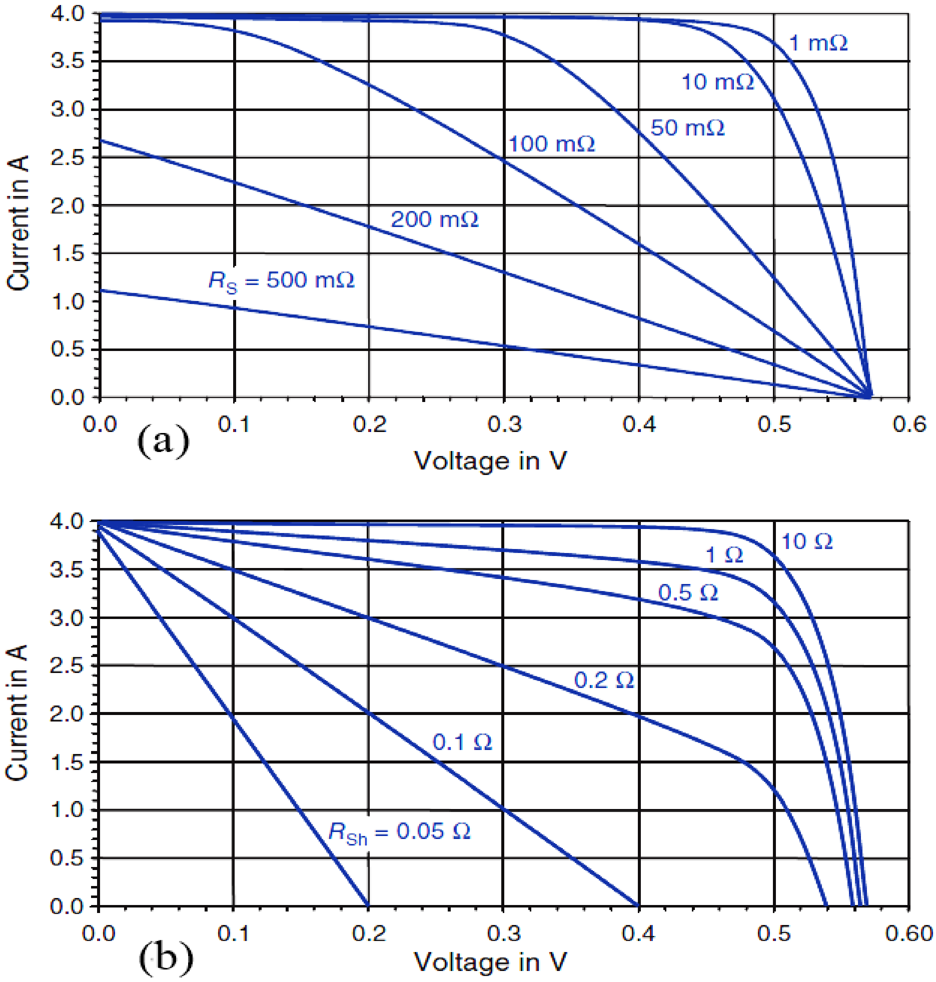

Figure 1.209: Influence of the series resistance (a) and parallel resistance (b) on the I-V characteristic of the solar cell [20].

2.5.3.3 The basic performance characteristics of solar cells

The fundamental performance characteristics of a solar cell are the short circuit current I_{sc}, open-circuit voltage Voc and the maximum power P_m, which takes place at V_m and I_m. These parameters are shown in Figure 1.20.

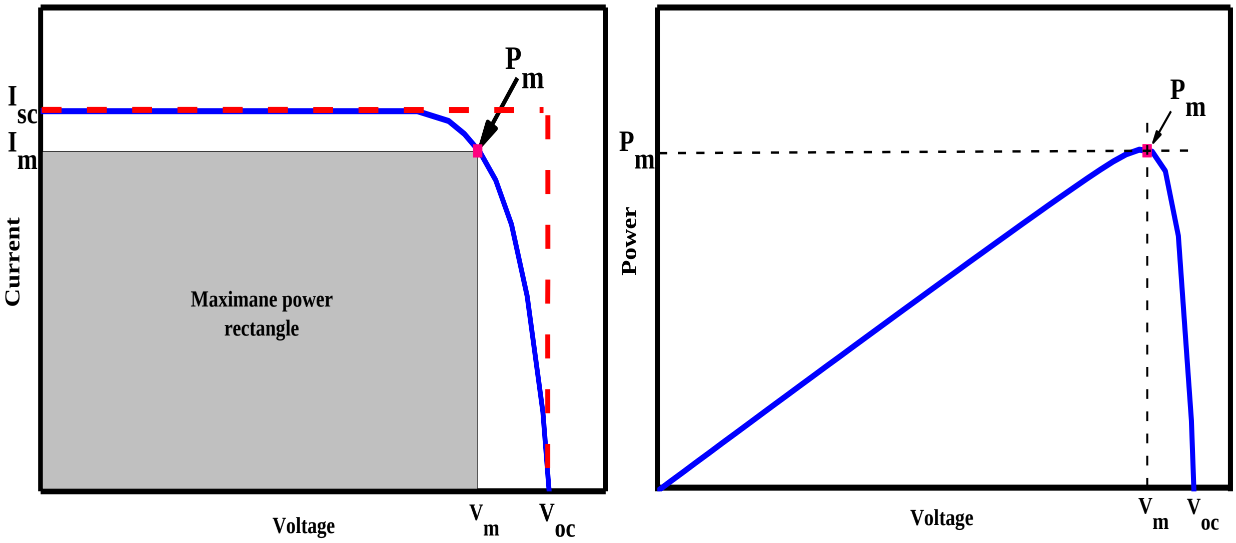

Figure 1.20: I-V characteristic of solar cell (Left) and the power produced by the cell (right), The power generated at the maximum power point is equal to the shaded rectangle in (right) [30].

1.5.3.3.1 Short circuit current I_{sc}

The short-circuit current is the current through the solar cell when the voltage across the solar cell is zero (that is when the cell is short-circuited). The short-circuit current is shown on the I-V curve Figure 1.20 (Left). In this condition and from equation (1.22), it can be shown that for an ideal solar cell, the short circuit current I_{sc} and photo-generated current I_{ph} are identical ($I_{sc}=I_{ph}$).

1.5.3.3.2 Open-circuit Voltage V_{oc}

Similarly, the open-circuit voltage is the voltage across the terminals of the cell when no load is connected to the cell (i.e., when the current becomes zero). To determine the open-circuit voltage, we resolve equation (1.22) while imposing $I=0$, which results in [30]:

$$V_{OC} = \frac{K_B T}{q} \ln\left(1 + \frac{I_{ph}}{I_s}\right) \tag{1.25}$$

1.5.3.3.3 Maximum power point P_m

The solar cell provides different capacities depending on the actual working point in which it is operated. The operating point at which the maximum power is provided is called the Maximum Power Point (P_m). The power $P = IV$ delivered by the cell is shown in Figure 1.20 (right). Maximum power will occur at the peak of the characteristic curve. The current and voltage values associated with the P_m are called I_m and V_m [20].

1.5.3.3.4 Fill Factor *FF*

The next parameter is the fill factor, which is the ratio of the maximum power from the solar cell to the product of V_{oc} and I_{sc} (See Figure 1.20 (Left)) so that [30]:

$$FF = \frac{I_m V_m}{I_{sc} V_{oc}} = \frac{P_m}{I_{sc} V_{oc}} \tag{1.26}$$

As depicted by the figure, *FF* shows the size of the area rectangle under the P_m working point compared to the rectangle area of $V_{oc}.I_{sc}$.

2.5.3.3.5 Efficiency η

The last basic parameter is the efficiency of a cell, which is defined as the ratio of energy output from the solar cell to input energy from the sun (see Figure 1.20 (Left)), calculated as [26]:

$$\eta = \frac{P_m}{P_{in}} = \frac{FF.I_{sc}.V_{oc}}{P_{in}} \tag{1.27}$$

Typically, the input power P_{in} (i.e., power of the sun) for efficiency calculations is 1000 W/m^2

2.5.4 Quantum efficiency

It is very important to know the quantum efficiency of a solar cell, where it indicates the amount of current that the cell will produce when irradiated by photons of a particular wavelength. There are two types of quantum efficiency:

2.5.4.1 External Quantum Efficiency *EQE*

EQE is the ratio of the number of charge carriers collected by the solar cell to the number of photons of a given energy shining on the solar cell from outside (incident photons). The reflection losses of the solar cell are taken into account in the value of the EQE:

$$EQE = \frac{Number\ of\ collected\ electron-hole\ pairs}{Number\ of\ incident\ photons} = \frac{I_{sc}}{P_{in}} \cdot \frac{hc}{q\lambda} \tag{1.28}$$

For example, Figure 1.21 shows the EQE of a typical production CdS/CdTe solar cell and the optical losses in each layer.

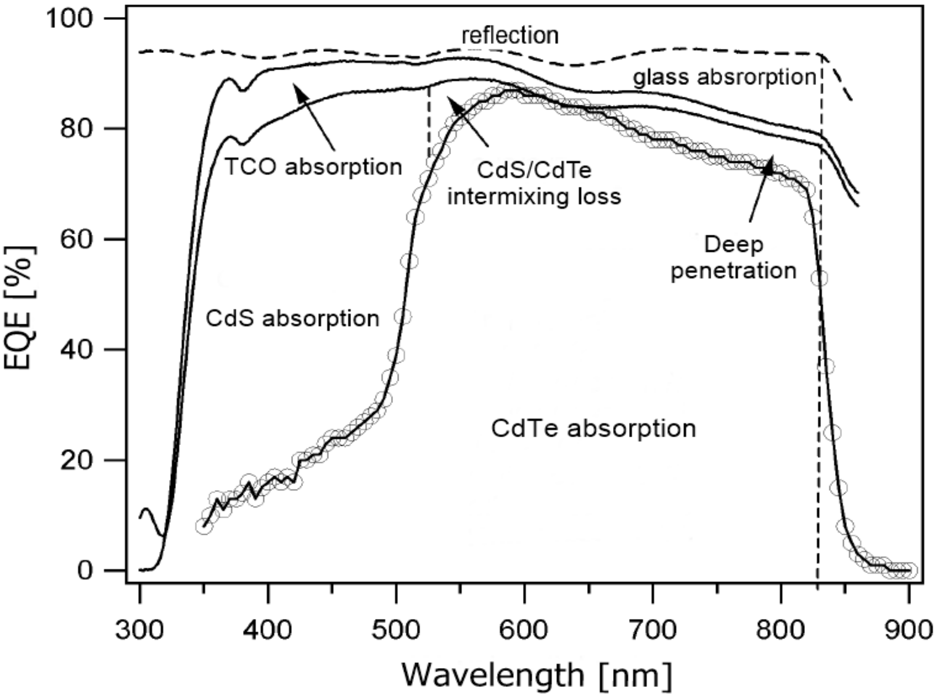

Figure 1.211: EQE and Photon loss of glass/TCO/CdS/CdTe solar cell [31].

1.5.4.2 Internal Quantum Efficiency *IQE*

IQE is the ratio of the number of charge carriers collected by the solar cell to the number of photons of a given energy that shine on the solar cell from outside and are absorbed by the cell. Contrary to the EQE, the losses caused by reflections are not considered in IQE:

$$IQE = \frac{Number\ of\ collected\ electron-hole\ pairs}{Number\ of\ absorbed\ photons} = \frac{EQE}{1-R} \tag{1.29}$$

where *R* is the reflection coefficient from the top surface of solar cell.

1.5.5 Loss mechanisms in Solar Cells

Losses in cells are a big problem, as they significantly reduce cell efficiency; some of these are avoidable but others are intrinsic to the system. Figure 1.22 summarizes most of these losses, as there are two fundamental types of losses: optical and electrical.

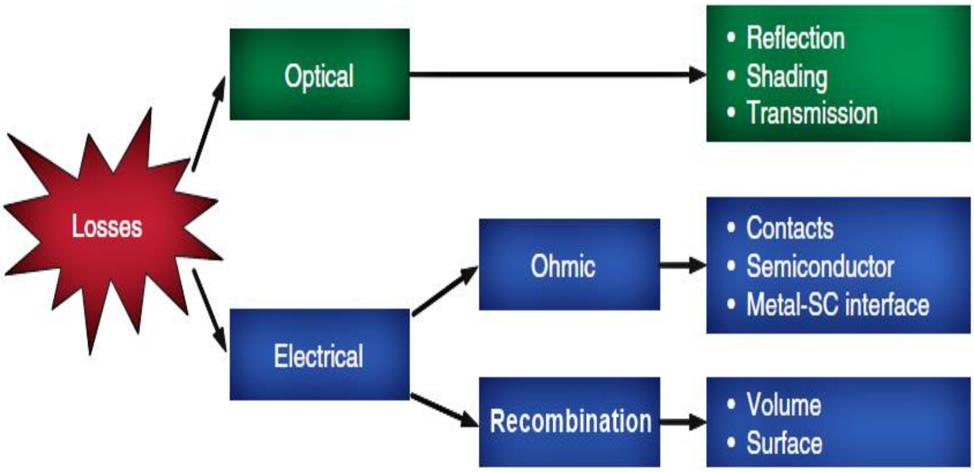

Figure 2.22: Different losses in the solar cell [20,32].

1.5.5.1 Optical losses

The optical losses are due to the reflection of part of the incident light from the front surface or the limited thickness of a solar cell that is insufficient to absorb most of the photons. Conversely, wide thickness deteriorates the solar cell performance. So, the appropriate thickness must be chosen very carefully. Add to this the transmission loss where a significant part of the solar spectrum is not utilized because of the incapability of the material to absorb the photons, which have energy less than the band gap energy $(E_{ph}<E_g)$. Therefore, these photons do not contribute to the generation of electron-hole pairs [32]. Also, if $E_{ph}> Eg$, the excess energy $(E_{ph}-E_g)$ is dissipated in the form of heat, this dissipated energy is called the thermalization loss.

1.5.5.2 Electrical losses

The Ohmic losses can happen in the doped regions of the device: emitter and base (absorber), as the conductivity of the doping material is limited. Also, in the contact fingers on the front side of the cell, this metallic front contact shadows some light. Furthermore, the metal-semiconductor junction in the case Schottky contact reduces the obtainable cell voltage.

The metal-semiconductor interface in the back contact of the cell poses a great risk for the generated EHP, as significant recombination can occur there, and thus the generated EHP does not contribute to solar cell current. Various mechanisms that minimize these recombinations exist, which we will mention it in subsequent chapters.

1.5.6 Types of solar cells

Currently, Solar cells are classified into four main categories (generations) depending on time and categories of materials used to manufacture them. Figure 1.23 summarizes the different generations of solar cells, and Figure 1.24 describes a chart of the highest confirmed conversion efficiencies for research cells for a range of photovoltaic technologies, plotted from 1976 to the present.

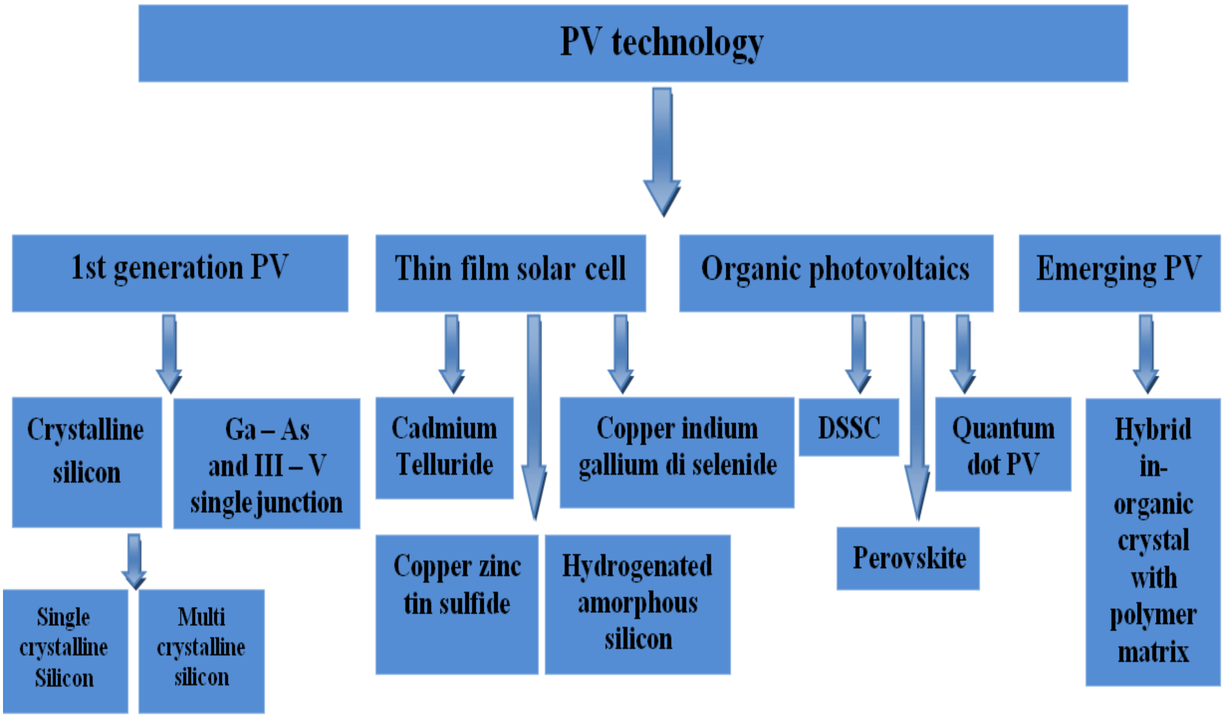

Figure 2.23: Various generations of solar cells [33].

1.5.6.1 First-generation solar cells

The first-generation is made up of three types: Mono-crystalline, Multi-crystalline silicon and Gallium Arsenide (GaAs) cells. These are considered one of the oldest and most common cells due to their high efficiency but are very costly to produce. Silicon is one of the most abundant materials in the Earth's crust, which implies that the availability of the raw material may be durable in the future and its acquisition cost could be reduced [34].

GaAs is particularly useful for multi-junction cells; those comprising multiple p–n junctions are made of different semiconductor materials. It allows a versatile cell design, since the incorporation of different dopant substances and the combination with other III-V materials within the cell structure significantly change the optoelectronic properties. Moreover, unlike Si-based cells, those based on GaAs have low-temperature coefficients, thus their performance is less affected by temperature [34]. In terms of cells performance, for single-junction, the best efficiency reached in the laboratory is 26.7 % for mono-crystalline, and 22.3 % for multi-crystalline silicon. For GaAs cells, it is between 18.4–29.1% depending on whether they have a crystalline structure or consist of a thin layer [9].

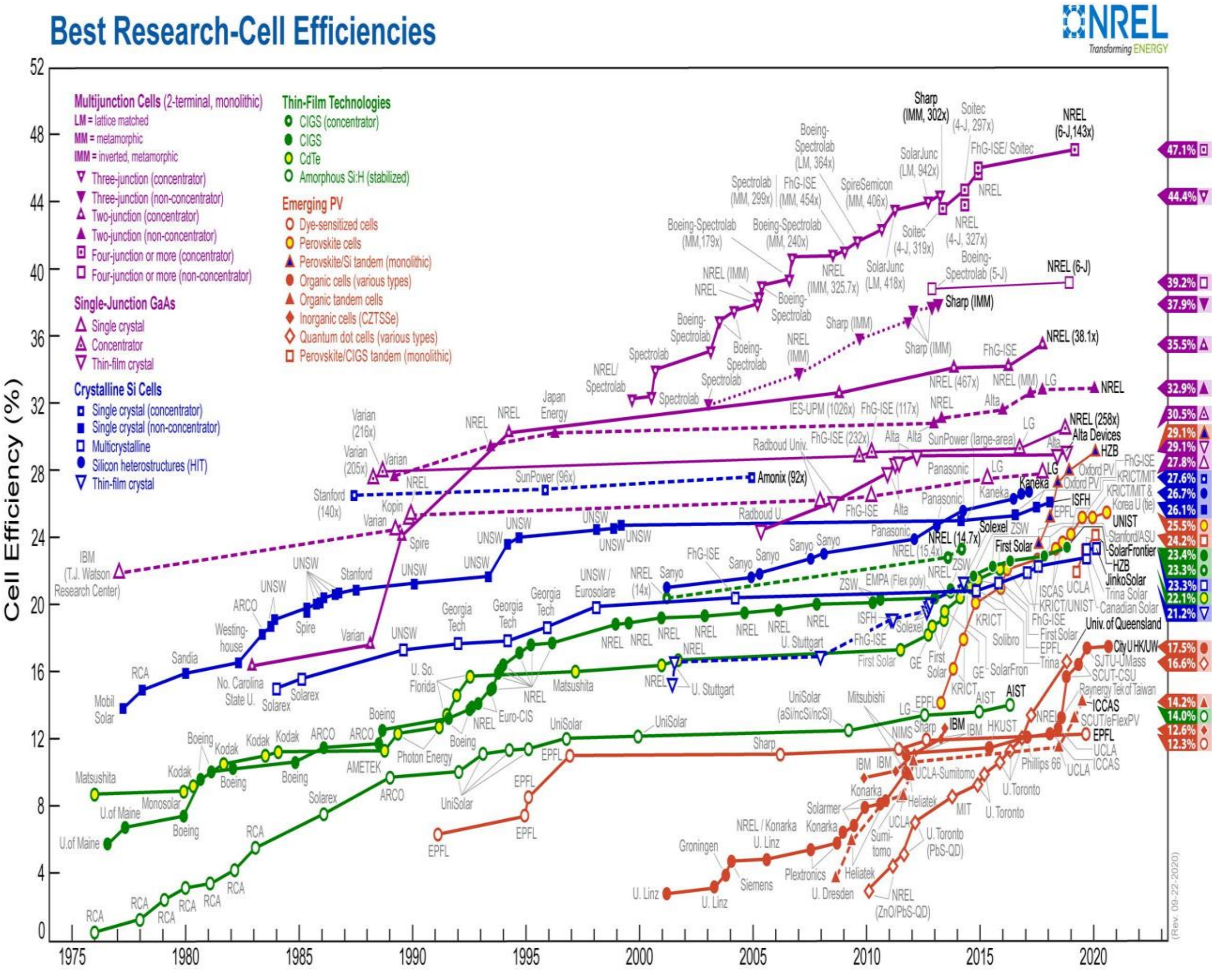

Figure 2.24: The best research-cell efficiencies. Taken from [35].

1.5.6.2 Second-generation solar cells

Thin-film solar cells (Figure 1.25) are the second-generation solar cells that have multiple thin-film layers of photovoltaic materials. Typically, it is made by depositing one or more thin layers, or thin film of photovoltaic material on a substrate, such as glass, plastic or metal. Thin-film solar cells have widespread commercial usage in several technologies such as copper indium gallium diselenide (CIGS), cadmium telluride (CdTe), Copper_zinc_tin_sulfide/selenide (CZTSSe), and amorphous thin-film silicon (a-Si).

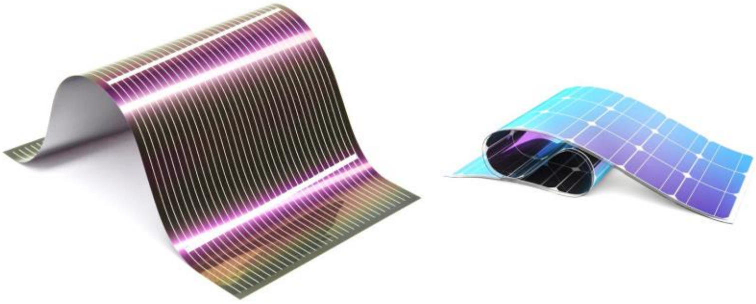

Figure 2.25: Thin films based solar cells.

Film thickness varies from a few nanometers (nm) to tens of micrometers (µm), much thinner than thin-films rival technology, the conventional, first-generation solar cell that uses wafers of up to 200 µm thick. This allows thin-film cells to be flexible and lower in weight. In addition, they are much more economical when compared to first-generation solar cells. These types of cells have a direct bandgap as opposed to the indirect bandgap of silicon and a high absorption coefficient. The table below illustrates the best efficiency of different types of 2GEN cells achieved until now (Table 1.1) [9]. We can observe that the efficiency of CIGS and CdTe cells are higher than that of the other three types. Besides, they are considered a strong competitor to other silicon cells on the world market.

Table 1.1: Efficiency of different types of 2GEN cells.

Types of 2GEN solar cells	Efficiency, %	Area, cm^2	Test Centre, Date
CIGS	23.35 ± 0.5	1.043	AIST (11/18)
CdTe	22.10 ± 0.5	0.4798	Newport (11/15)
CZTSSe	12.60 ± 0.3	0.4209	Newport (7/13)
CZTS	11.00 ± 0.2	0.2339	NREL (3/17)
Si (amorphous)	10.20 ± 0.3	1.001	AIST (7/14)

AIST: Japanese National Institute of Advanced Industrial Science and Technology

NREL: National Renewable Energy Laboratory

1.5.6.3 Third-generation solar cells

These third-generation solar cells are much different from the first and second generations as they do not rely on a conventional p-n junction for the separation of photogenerated charge carriers. Instead they consist of multiple energy levels, multiple carrier pair generation, and are capable of capturing carriers before thermalization [33]. Among the common technologies included in the third-generation solar cells are:

- Dye-sensitized solar cells (DSSCs), also known as "Grätzel cell".
- Perovskite cells.
- Quantum dot cells.
- Organic solar cells.

One of these technologies that have received tremendous attention recently from the public are perovskite cells; they are among the fastest-advancing solar technologies with high-efficiencies over 25% (see Table 1.2).

Table 1.2: Efficiency of different types of 3GEN cells.

Types of 3GEN solar cells	Efficiency, %	Area, cm^2	Test Centre, Date
Perovskite	25.2 ± 0.8	0.0937	Newport (7/19)
Organic	17.35 ± 0.2	0.862	NREL (10/19)
Quantum dot	16.6	0.1	NREL (/19)
DSSCs	12.25 ± 0.4	0.0963	AIST (8/19)

1.5.6.4 Fourth-generation solar cells

4Gen Solar cells, designated as Hybrid or "organic in inorganic" solar cells, are the emerging trend in cells technology. The cells fall into the class of conjectural generations consisting of composites. These composites are made out of polymers mixed with nanoparticles to have the properties of a single absorber layer. These can be further stacked to form thin multispectrum layers, which are cheaper and more efficient than any other generation of solar cells [33]. As an example of these inorganic nanoparticles, we mention quantum dots or nanowires and polymers like Perylene, PPV, PEDOT, etc. To date, the efficiency of this generation of cells is low and does not exceed 12%.

1.6 Conclusion

In the first chapter, and for a better understanding of the following work, we presented the solar cells basic information as semiconductor and their types, p-n junction and necessary calculations in this context such as the total depletion layer width and the built-in voltage, etc., the solar spectrum AM0, AM1.5G (Global) and AM1.5D (Direct), the photovoltaic effect and the working principle of solar cells. Also, we introduced the equivalent circuit of an ideal and non-ideal solar cell, and the basic performance characteristics of solar cells (I_{sc}, V_{oc}, P_m, *FF*, η, *EQE*, *IQE*), in addition to the optical and electrical losses in solar cells. Eventually, we touched on the different types of solar cells and the performance of every type.

CHAPTER 2: Physical Properties of semiconductors II-VI and the materials used in the design of CdS/CdTe solar cells

2.1 Introduction

For a long time, silicon has dominated the market as the main component in the manufacture of various electronic components. However, over time and with the evolution of technology, new alternatives and effective materials have broken that dominance and become competitive in the global market. Among these materials are the II-VI semiconductors. These components have remarkable physical properties, and play a major role in microwave applications, power electronics, and especially in the field of optoelectronics. In this chapter, we will focus on II-VI materials, and in particular on CdTe and CdS, which are at the center of this thesis work and which present several advantages with different physical and optical properties making them well suited to optoelectronic applications such as photovoltaics. We will define in this second chapter the II-VI semiconductors, especially those that will be used in the rest of this work to carry out our simulations. We will also present and discuss in the second part of this chapter the conventional structure of CdS/CdTe solar cells, which is used in a large fraction of current CdTe solar cells research. The losses mechanisms in the CdS/CdTe structure will be discussed and the recent methods used to reduce these losses with a particular focus on the back contact problems.

2.2 II-VI Semiconductors

II-VI semiconductor materials are compound bodies containing elements from groups II and VI in the periodic table (Figure 2.1). Different material systems combining these elements can be produced in the form binary or ternary compounds.

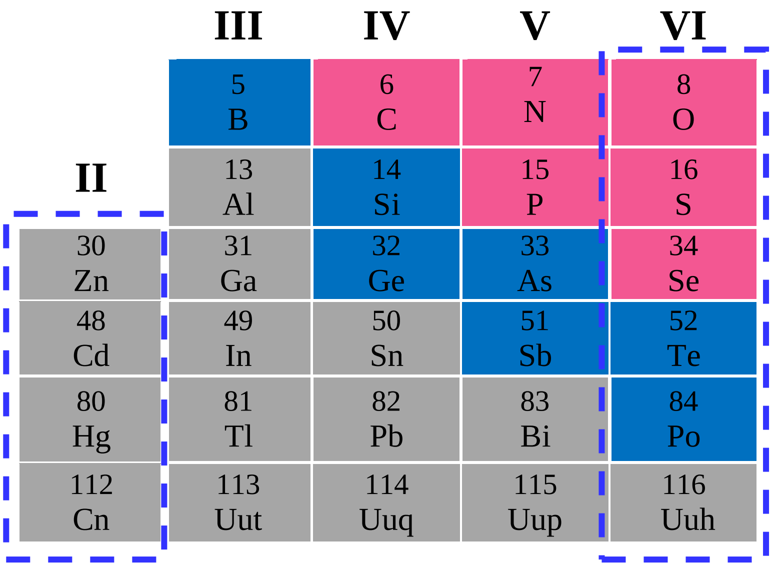

II	III	IV	V	VI
	5 B	6 C	7 N	8 O
	13 Al	14 Si	15 P	16 S
30 Zn	31 Ga	32 Ge	33 As	34 Se
48 Cd	49 In	50 Sn	51 Sb	52 Te
80 Hg	81 Tl	82 Pb	83 Bi	84 Po
112 Cn	113 Uut	114 Uuq	115 Uup	116 Uuh

Figure 2.1: II-VI semiconductor compounds [36].

II-VI semiconductor compounds can have different crystal structures but the two most commonly types are hexagonal wurtzite and cubic zinc-blende (see Figure 2.2). Binary compounds materials include Cadmium Telluride (CdTe), Cadmium Sulfide (CdS), Zinc Oxide (ZnO), Zinc Tellurium (ZnTe), Zinc Sulfide (ZnS), among others. Ternary compounds compriseMercury cadmium telluride ($Hg_{1-x}Cd_xTe$) and Cadmium Zinc Telluride ($Cd_{1-x}Zn_xTe$), etc.

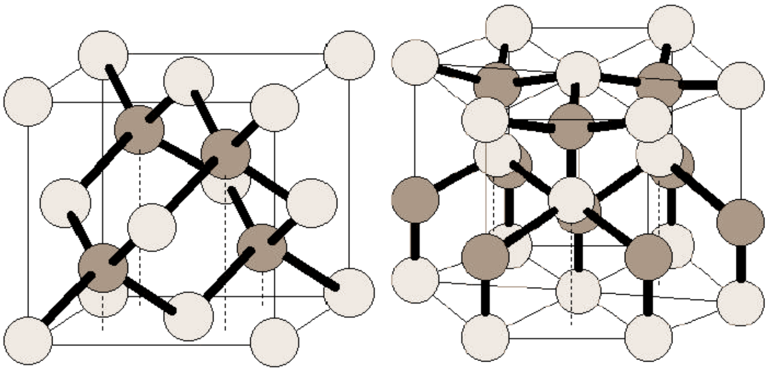

Figure 2.2: Cubic zinc-blende (left) and Hexagonal wurtzite (right) structures [37].

Bonding in II–VI compounds is a mixture of covalent and ionic types. This is because group-VI elements are considerably more electronegative than group II elements. The ionic character has the effect of binding the valence electrons rather tightly to the lattice atoms [36]. Thus, II-VI semiconductors offer a wide range of band gap energies from 0.02 eV to 4 eV with a mostly direct band gap, and are primarily used as optoelectronic devices in spectral regions where Si and III-V devices cannot provide the required band gap [7]. In terms of conductivity, several of the II-VI compounds possess n-type conductivity, others p-type conductivity and another set can possess both types of conductivity.

Compared to the III-V compounds, the effective mass of carriers in II-VI compounds is relatively high, the radiative carrier lifetime is small, and the carrier diffusion length is short. Due to the high absorption coefficient, a II-VI semiconductor of about 1 µm thickness is sufficient to absorb 99% of the impinging radiation with photon energy greater than the bandgap energy. Thus, they are very appropriate for thin-film optical devices. Besides, it has the advantage that they can be prepared in the form of high-quality polycrystalline films from low-cost raw materials by several low-cost techniques [6]. II-VI compounds are used to manufacture many devices as shown in Figure 2.3.

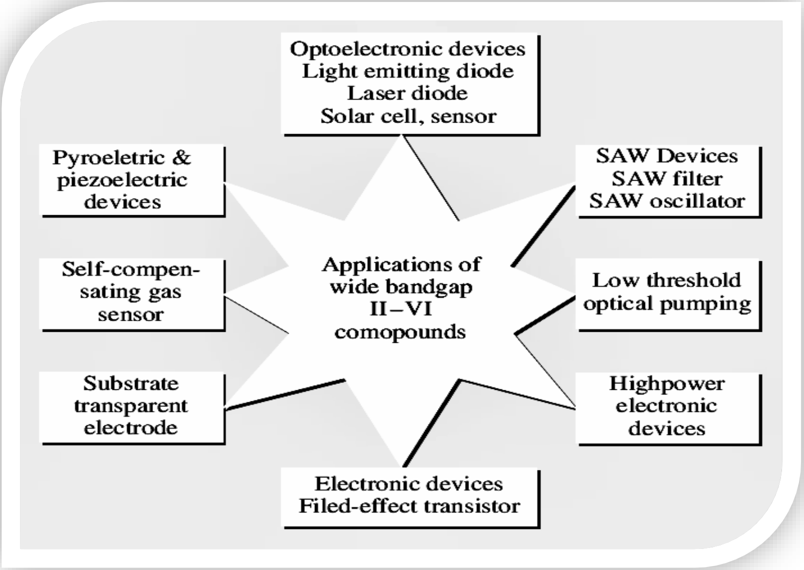

Figure 2.3: Application of II–VI compounds [38].

2.2.1 Cadmium sulfide CdS

Cadmium Sulfide (CdS) is considered one of the most attractive II-VI compounds. It has great application potential in the field of solar cells, photo sensors, optical detectors, transducers, and optoelectronic devices due to the physical and electrical properties of this material. CdS has a wide band gap of 2.42 eV at room temperature [39,40], usually, the undoped CdS has naturally n-type conductivity because of native defects of sulfur (S) vacancies [41,42]. CdS is found naturally in minerals greenockite and hawleyite in the form of wurtzite and hexagonal structure, respectively. These structures are shown in Figure 2.4 where it is clearly evident that the lattice parameter value of CdS is a = 5.8 Å and for Wurtzite phase a = 4.1 Å, c = 6.7 Å.

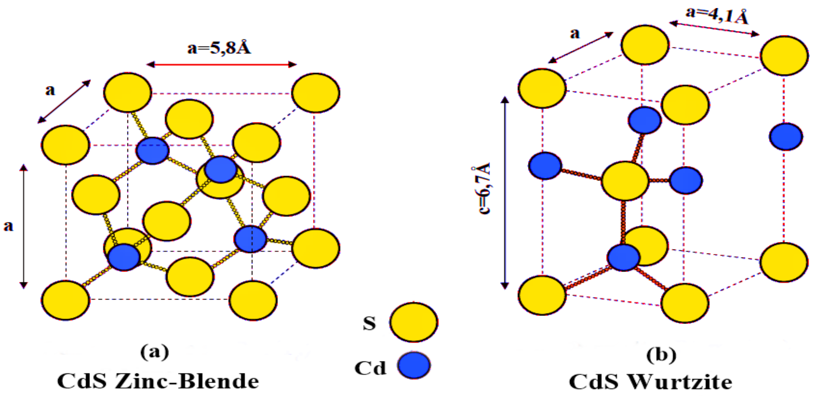

Figure 2.4 The crystal structure of CdS (a) cubic (b) Hexagonal [43].

CdS films are produced by different techniques including metal-organic chemical vapor deposition (MOCVD) [44], close space sublimation (CSS)[45], chemical bath deposition (CBD) [46] and sputtering [47], etc.

The dark resistivity of as-deposited CdS films is usually in the range of about 10^4 and 10^6 Ω.cm. These CdS films are suitable for solar cell purposes because they increase their conductivity under illumination [40]. In terms of optical properties, CdS thin films have a high optical transmittance (70– 80% in the visible range) [48] and a high refractive index equal 2.4289 at 0.5876µm [49]. In more detail, the table below summarizes some properties of CdS thin films.

Table 2.1: Several properties of CdS [38,43,50,51].

Material	**CdS**		
Crystal structure	**zinc-blende**	**wurtzite**	
	a	***a***	***c***
Lattice constant, (Å)	5.825	4.137	6.716
Crystal density, (g/cm^3)	4.855	4.8208	
Molecular weight, *M (amu)*	144.477		
Melting point, T_m *(k)*	2023		
Effective mass of electron, m_e^*	$0.19\ m_0$		
Effective mass of hole, m_h^*	$0.8\ m_0$		
Bandgap, *Eg* (eV)	2.42		
Electron affinity, χ_e (eV)	4.3		
spin-orbit coupling, Δ_{SO} (eV)	0.066		
Dielectric ratio, ε_r	10		
Electron mobility, μ_n (cm^2/Vs)	100		
Hole mobility, μ_p (cm^2/Vs)	25		
Electron Lifetime, (ns)	0.01		
Hole Lifetime, (ns)	0.01		

2.2.2 Cadmium telluride CdTe

Cadmium telluride CdTe is a stable crystalline compound formed from cadmium and tellurium. It is one of the few II–VI compounds that are usually used as absorbers for photovoltaic devices [52]. CdTe exhibits a forbidden gap of 1.5 eV and an absorption coefficient that exceeds 5 $\times 10^5$ cm^{-1} [53]. These two main factors make this material capable of absorbing the solar spectrum within a few micrometers thickness. Figure 2.5 shows the energy band structure of CdTe, where the lowest conduction band edge $\mathbf{\Gamma_6}$ and highest valence band edge $\mathbf{\Gamma_8}$ are both at $\mathbf{\Gamma}$ represent the direct energy gap of CdTe.

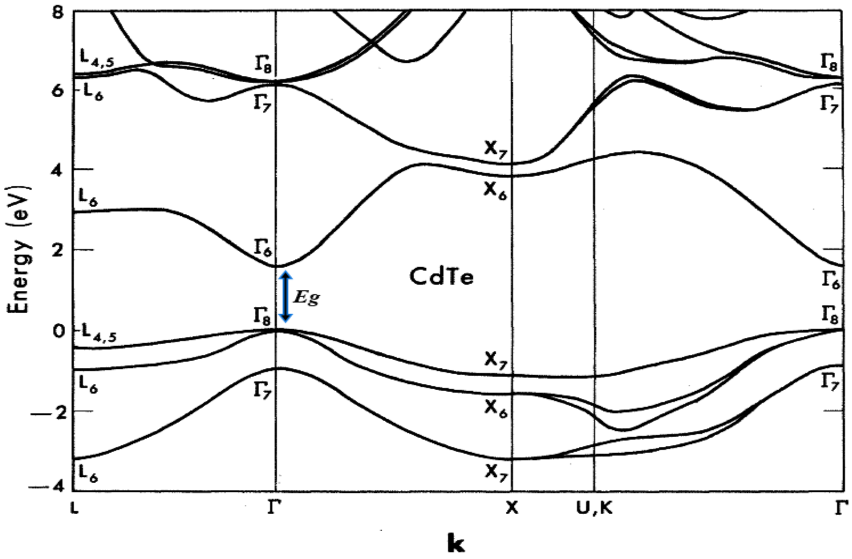

Figure 2.5: Energy bands structure of CdTe [54].

The lattice constant of CdTe is estimated a = 6.48 Å for zinc-blende (see Figure 2.6) and a = 4.57 Å, c =7.47 Å for wurtzite CdTe. Also, for the conductivity, CdTe can be prepared in both p- and n-type, with typical doping like P, Cu, Ag, As, and Li for p-type and Zn, I, In, and Al for n-type. However, the p-type CdTe is more difficult to produce, and this difficulty stems from both strong compensation effects and low solubility of the usual dopant species [55]. CdTe has a refractive index of 2.9589 at 0.5876 μm wavelength [49].

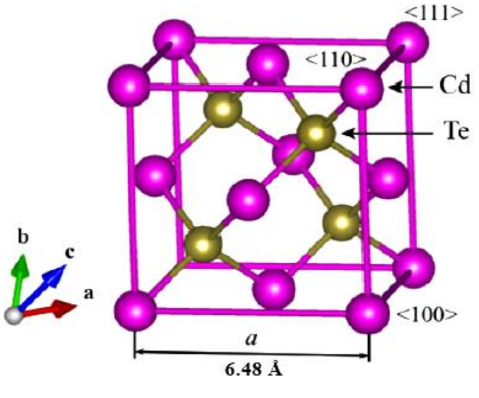

Figure 2.6: The crystal structure of cubic CdTe. a, b and c are primitive cell vectors directed along <110> and a is the lattice parameter [56].

Commercially, CdTe is available as a powder or as crystals. It can be made into nanocrystals. CdTe can be produced using a number of different low-cost techniques such as vapor transport deposition (VTD) [57], electrodeposition [58], sputtering [59], MOCVD [44], CSS [60] and thermal evaporation [61]. For further information about the properties of CdTe, Table 2.2 summarizes different parameters of this material.

Table 2.2: Different properties of CdTe [38,50,51,54,62,63].

Material	**CdTe**		
Crystal structure	**zinc-blende**	**wurtzite**	
	a	***a***	***c***
Lattice constant, (Å)	6.481	4.57	7.47
Crystal density, *g* (g/cm^3)	5.856	5.90	
Molecular weight, *M (amu)*	240.01		
Melting point, T_m *(k)*	1370		
Effective mass of electron, m_e^*	0.09 m_0		
Effective mass of hole, m_h^*	0.4 m_0		
Bandgap, *Eg* (eV)	1.5		
Electron affinity, χ_e (eV)	4.28		
spin-orbit coupling, Δ_{SO} (eV)	0.91		
Dielectric ratio, ε_r	9.4		
Electron mobility, μ_n (cm^2/Vs)	320		
Hole mobility, μ_p (cm^2/Vs)	40		
Electron Lifetime, (ns)	1		
Hole Lifetime, (ns)	1		

CdTe is more stable than its parent compounds cadmium and tellurium and most other Cd compounds, due to its high melting point of ≈1370 k and insolubility.

As it is known, Cd is considered a toxic material. Unfortunately, this fact has made CdTe also toxic in the view of many people. Despite the great expansion in the use of CdTe in the production of many photovoltaic devices, this negative perception has wrongly limited the use of this compound material in the manufacture of many devices, where these arguments have been used as a powerful weapon against these efficacious CdTe-based technologies. But the truth is a bit more complicated, and the environmental impact of CdTe is actually very much different from what one might think. This has been reported and proved by a large number of studies from different laboratories [64–72]. CdTe is actually not registered as a carcinogenic compound and results show it to be 100 times less toxic than elemental cadmium [71]. This allows us to say that the compound CdTe has different qualities than the two elements, Cd and Te, taken separately. In that regard, researchers from the U.S. Department of Energy's Brookhaven National Laboratory have found that large-scale use of CdTe PV modules does not present any risks to health and to the environment [64].

2.2.3 Zinc oxide ZnO

Besides CdTe and CdS, zinc oxide (ZnO) is also a member that belongs to the II-VI semiconductor family. It has a direct band gap of about 3.3 eV at room temperature [73,74] and a hexagonal structure (Figure 2.7) with lattice parameters of a = 4.57 Å and c = 7.47 Å [50]. This crystal structure is considered the most common because it is more stable at ambient conditions compared to the cubic structure. Pure ZnO is a white powder, but in nature it occurs as the rare mineral zincite, which usually contains manganese and other impurities that confer a yellow to red color [75].

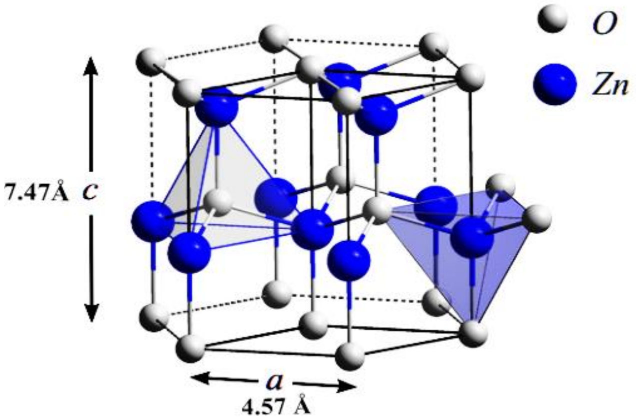

Figure 2.7: The crystal structure of hexagonal ZnO.

The undoped ZnO naturally is an n-type semiconductor due to the presence of intrinsic or extrinsic defects, which were generally attributed to native defects, such as the Zn interstitial, and the O vacancy, in addition to the hydrogen impurities in ZnO, which occurs exclusively in the positive charge state and is also responsible for the n-type conductivity [76]. Undoped crystals have a typical resistivity of 0.1-100 Ω.cm [38]. N-type conductivity of ZnO can be augmented by extrinsic doping using the III_group elements (B, Al, Ga, and In). For p-type, Group I elements (Li, Na, or K) in addition to Cu and Ag can be used [75]. Pertinent quantities of the ZnO are listed in Table 2.3.

Table 2.3: Some properties of ZnO [38,50,63,74,77,78].

Material	**ZnO**		
Crystal structure	**zinc-blende**	**wurtzite**	
	a	***a***	***c***
Lattice constant, (Å)	4.47	3.2495	5.2069
Crystal density, *g* (g/cm^3)	6.05	5.6768	
Molecular weight, *M (amu)*	81.39		
Melting point, T_m *(k)*	2248		
Effective mass of electron, m_e^*	$0.28m_0$		
Effective mass of hole, m_h^*	$0.59m_0$		
Bandgap, *Eg* (eV)	3.3		
Electron affinity, χ_e (eV)	4		
spin-orbit coupling, Δ_{SO} (eV)	-0.005		
Dielectric ratio, ε_r	9		
Electron mobility, μ_n (cm^2/Vs)	100		
Hole mobility, μ_p (cm^2/Vs)	25		
Electron Lifetime, (ns)	10		
Hole Lifetime, (ns)	0.1		
refractive index, *n*	2.029		
Electrical resistivity, ρ (Ω.cm)	From 10^{-1} up to 10^6		

Moreover, ZnO has one of the biggest electromechanical coupling factors. As a result of this property, zinc oxide is a well-known piezoelectric material, which has been used as a transducer for surface acoustic wave devices [40]. Besides, the high transparency of zinc oxide in the visible region made it a very sought-after material used as a transparent conductive oxide (TCO) or High-resistivity transparent (HRT) buffer layer, especially in thin-film solar cells such as CdTe, CIGS, and CZTS, etc. On the other hand, there are different growth techniques for ZnO such as reactive thermal evaporation and Chemical Bath Deposition (CBD), Chemical Vapor Deposition (CVD), D.C. reactive and R.F. magnetron sputtering [79–81].

2.3 Tin oxide SnO_2

Tin oxide (SnO_2) or so-called stannic oxide occurs in nature as the mineral cassiterite. It possesses the rutile crystal structure with a tetragonal unit cell and have lattice parameters a = b 4.738 Å, c =3.188 Å and *u* is approximately 0.307, which represents the distance between Sn and O atoms [82]. The crystal structure of SnO_2 is schematically shown in Figure 2.8 where it is clearly shown that each Sn atom has six nearest oxygen neighbors, which form a distorted octahedron. Sn atoms fill the center of the oxygen octahedron.

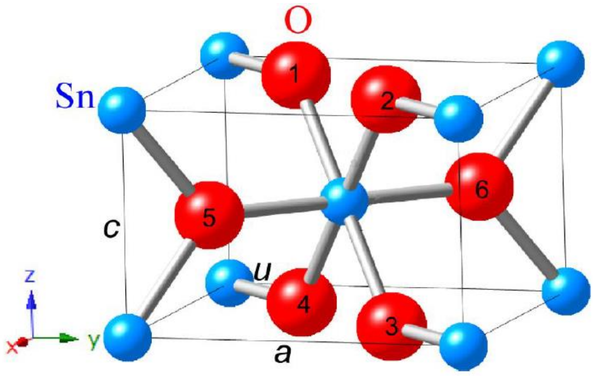

Figure 2.8: The crystal structure of unit cell of SnO_2 [83].

The SnO_2 band gap is estimated to be about 3.6 eV [73,82], as seen in Figure 2.9. SnO_2 is a transparent n-type semiconductor, and its conductivity is thought to be due to intrinsic defects formation in the material, which result from oxygen vacancies and tin interstitials [83,84]. Many dopants, such as fluorine (F), antimony (Sb), arsenic (As), phosphorus (P), molybdenum (Mo), etc., are employed to improve the electrical and optical properties of n-type SnO_2. Conversely, for the p-type SnO_2, doping like Aluminum (Al), gallium (Ga), Zinc (Zn), etc., are used.

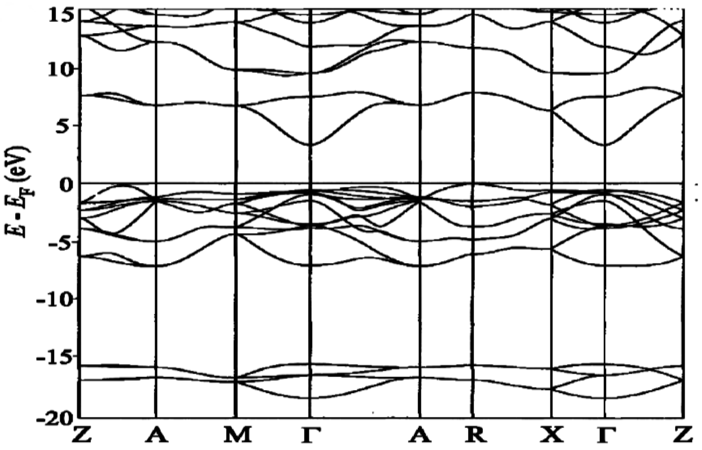

Figure 2.9: Band structure of SnO_2 [82].

SnO_2 is widely utilized as a base material in gas alarms on various buildings because it is highly sensitivity to small concentrations of gases. Also, like zinc oxide, tin oxide is too used in solar cells as a TCO or as an HRT layer. This is due to high transparency in the visible part of the light spectrum (more than 90%) and high reflectivity for infrared (IR) light. In this context, Figure 2.10 shows the optical transmittance curves as a function of the wavelength of the SnO_2 with different resistivities. Clearly, as the resistivity decline, the plasma edge moves to higher energy, and thus declining transmission in the IR. At short wavelengths (high energies), electron-inter band transitions from the valence band to the conduction band quell the transmission. However, long wavelengths (IR light) are reflected due to the plasma edge. The high transparency in the visible wavelength range of 380 to 740 nm (1.7 eV to 3.3 eV) was explained by the fact that the band gap of the material is higher than the maximum energy of the visible spectrum, so none of the light is absorbed and just passes through the material [82]. Particularly, they are stable up to high temperatures, have excellent resistance to strong acids and bases at room temperature as well as to mechanical wear, and have very good adhesion to many substrates [85].

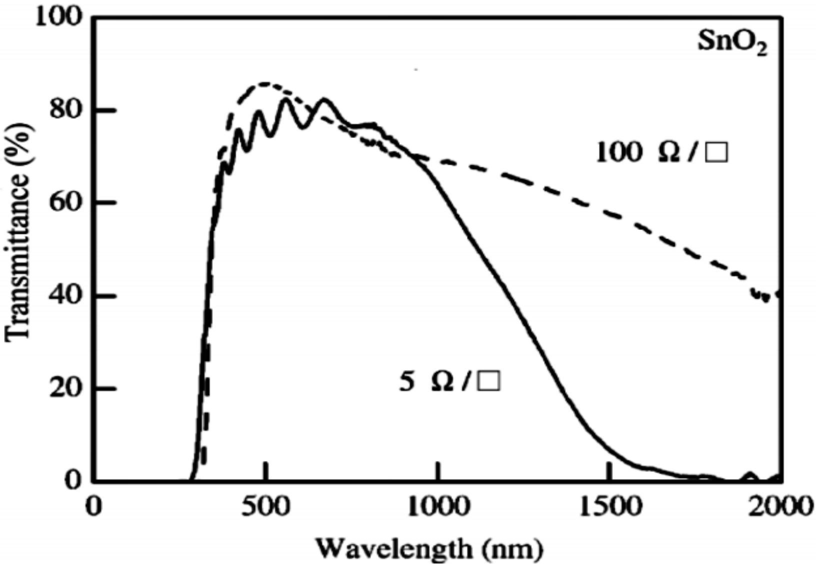

Figure 2.10: The optical transmittance spectra of SnO_2 films for different conductivity of the films [83].

SnO_2 thin films are deposited by several physical methods such as chemical vapor deposition [86], sputtering [87], sol–gel [85] and chemical spray pyrolysis [88], etc., each of these methods has advantages and disadvantages. To further understanding about the properties of SnO_2, the most important basic parameters are listed in Table 2.4.

Table 2.4: The different basic parameters of SnO_2 [51,62,82,88].

Material	**SnO_2**	
Crystal structure	Tetragonal	
	a, b	***c***
Lattice constant, (Å)	4.738	3.188
Crystal density, g (g/cm^3)	6.95	
Molecular weight, M (amu)	150.69	
Melting point, T_m (k)	2643	
Effective mass of electron, m_e^*	0.23 m_0	
Effective mass of hole, m_h^*	1.0 m_0	
Bandgap, Eg (eV)	3.6	
Electron affinity, χ_e (eV)	4.5	
Dielectric ratio, ε_r	9	
Electron mobility, μ_n (cm^2/Vs)	100	
Hole mobility, μ_p (cm^2/Vs)	25	
Electron Lifetime, (ns)	0.1	
Hole Lifetime, (ns)	100	
Refractive index, n	1.9	
Electrical resistivity, ρ (Ω.cm)	From 0.83×10^{-4} up to 10^6	

2.4 Cuprous oxide Cu_2O

When oxidized, copper can form a type of oxide, which is a cuprous oxide (Cu_2O). It has a direct band gap ranging from 2.0 to 2.6 eV depending on the preparation methods and conditions [89–92], Figure 2.11 displays the band structure.Cu_2O is distributed over the entire planet earth and has been mined since antiquity due to its high copper content (88.8%). The crystal structure in its cubic lattice is illustrated in Figure 2.12, with a lattice constant of 4.27 Å. O atoms occupy the body center and edges of the cubic unit cell, and each tetragonally coordinated to four Cu atoms, which are, in turn, linearly coordinated to two O atoms [93].

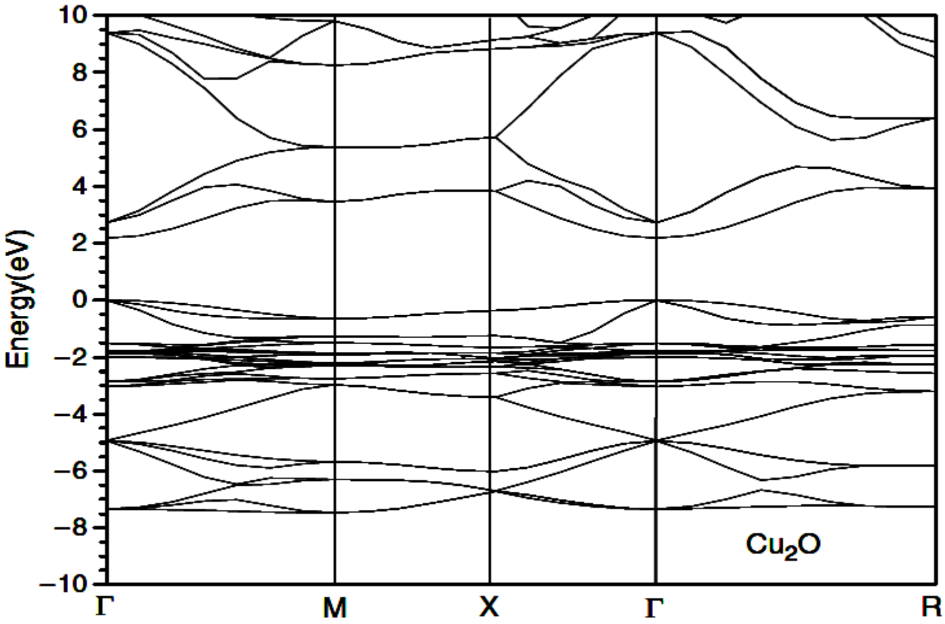

Figure 2.11: Energy bands structure of Cu_2O [82].

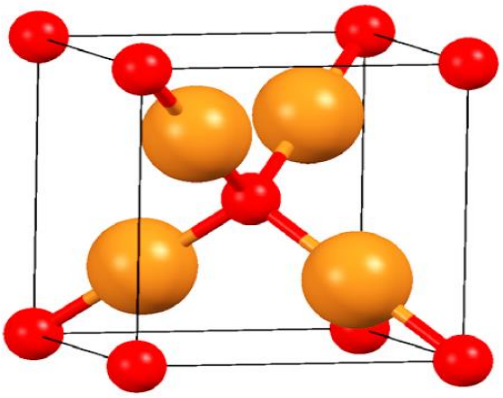

Figure 2.12: Crystal structure of Cu_2O. Oxygen atoms are depicted in red, and copper atoms are depicted in orange [93].

Naturally, Cu_2O is a p-type conductivity semiconductor as it contains negatively charged copper vacancies (V_{cu}) and most likely interstitial oxygen (O_i) [89,94]. To get a better p-type conductivity for Cu_2O, Magnesium (Mg), Sodium (Na), Nitrogen (N), or Manganese (Mn) are used as dopants, while for n-type, Chlorine (Cl), Fluorine (F), or Bromine (Br) are utilized. Concerning fabrication, various deposition methods are employed to prepare copper oxide thin films. These include reactive sputtering [95], pulsed laser deposition (PLD) [92], sol–gel [96] and thermal oxidation [94], etc. In more detail about the properties of Cu_2O material, Table 2.5 shows some of them.

Table 2.5: Properties of Cu_2O [89,90,97–100].

Material	**Cu_2O**
Crystal structure	**Cubic**
	a
Lattice constant, (Å)	4.27
Crystal density, *g* (g/cm^3)	5.749 – 6.140
Molecular weight, *M (amu)*	143.14
Melting point, T_m *(k)*	1508
Effective mass of electron, m_e^*	0.93 m_0
Effective mass of hole, m_h^*	0.56 m_0
Bandgap, *Eg* (eV)	2.2
Electron affinity, χ_e (eV)	3.3
spin-orbit coupling, Δ_{SO} (eV)	0.13
Dielectric ratio, ε_r	9
Electron mobility, μ_n (cm^2/Vs)	200
Hole mobility, μ_p (cm^2/Vs)	25
Electron Lifetime, (ns)	10
Hole Lifetime, (ns)	10
Refractive index, *n* at (580 nm)	3.054
Electrical resistivity, ρ (Ω.cm)	From 10^{-2} up to 10^3

In recent years, the Cu_2O substance has received enormously growing attention even though it has been known for many decades. This interest is due to a number of reasons, among which, its non-toxicity, low-cost, and abundance in the Earth's crust. Moreover, its numerous characteristics in terms of cellular inertness, good carrier mobility, relatively high minority carrier diffusion length, high optical absorption coefficient in the visible range, and good electrical properties make it attractive in the fabrication of many devices [94]. Among those applications (photocatalytic water splitting, thin-film transistors, resistive random access memory, spintronic devices) but the big focus was in the field of photovoltaic where it showed a good performance. Indeed, it is considered a good material for the fabrication of photovoltaic devices [91].

2.5 CdS/CdTe solar cells

The high absorption coefficient of Cadmium Telluride, which exceeds 5 × 10^5/cm and the direct band-gap of 1.5 eV, exactly matches to the solar spectrum and makes it a perfect candidate as a solar cell material capable of absorbing the majority of photons in the visible range, which have energy more than the band-gap ($E_{photon} \geq E_g$) to convert the maximum of sunlight into electricity [53]. Theoretically, according to the Schockley-Queisser limit with the CdTe bandgap, it could deliver a maximum efficiency of up to 32% [101], as plotted in Figure 2.13.

Since the middle of the last century, and exactly in 1959, for the first time Rappaport of RCA Lab observed the photovoltaic potential of CdTe, where he manufactured CdTe homojunction solar cells with 2% efficiency, via the diffusion of In into p-type single crystalline CdTe [102]. Since then, a lot of research has been devoted to CdTe solar cells. In1972, Bonnet et al. presented new results based on CdS/CdTe heterojunction, which exhibited a photoelectric conversion efficiency of 6%, thus these became the first to produce the CdS/CdTe thin-film solar cell.

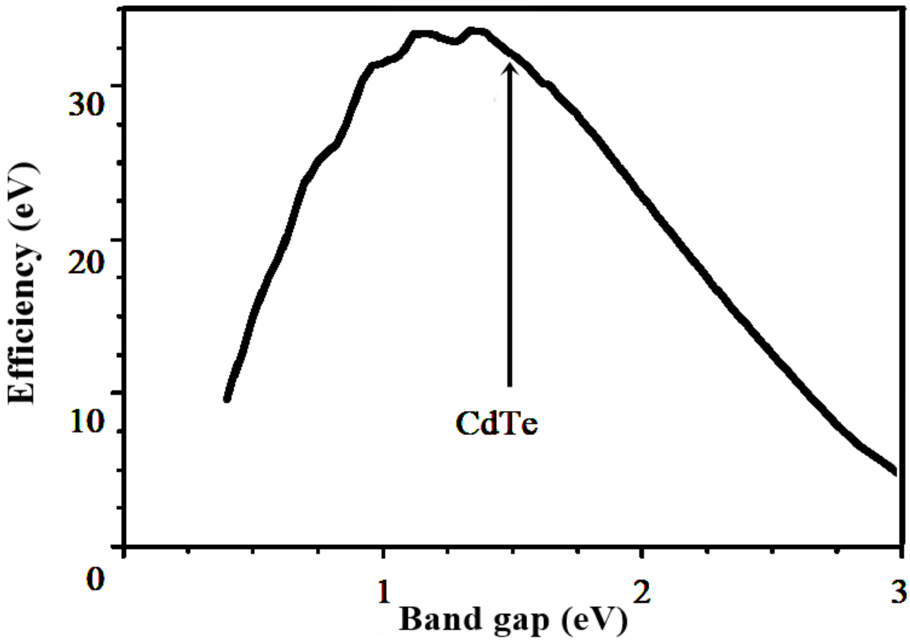

Figure 2.13: The Shockley-Queisser theoretical maximum efficiencies for CdTe solar cell. Adapted from Shockley et al [101].

At present, the CdTe solar cells offer low energy costs (~0.0387 $/kWh) [10], which makes it one of the most competitive kinds in the photovoltaic trade markets. Over more than 60 years, CdTe solar cells have known a great development in terms of manufacturing, thus remarkably improving the conversion efficiency from 2% in 1959 to 22.1% in 2020. Figure 2.14 shows the efficiency of CdTe solar cells over the years [9,35].

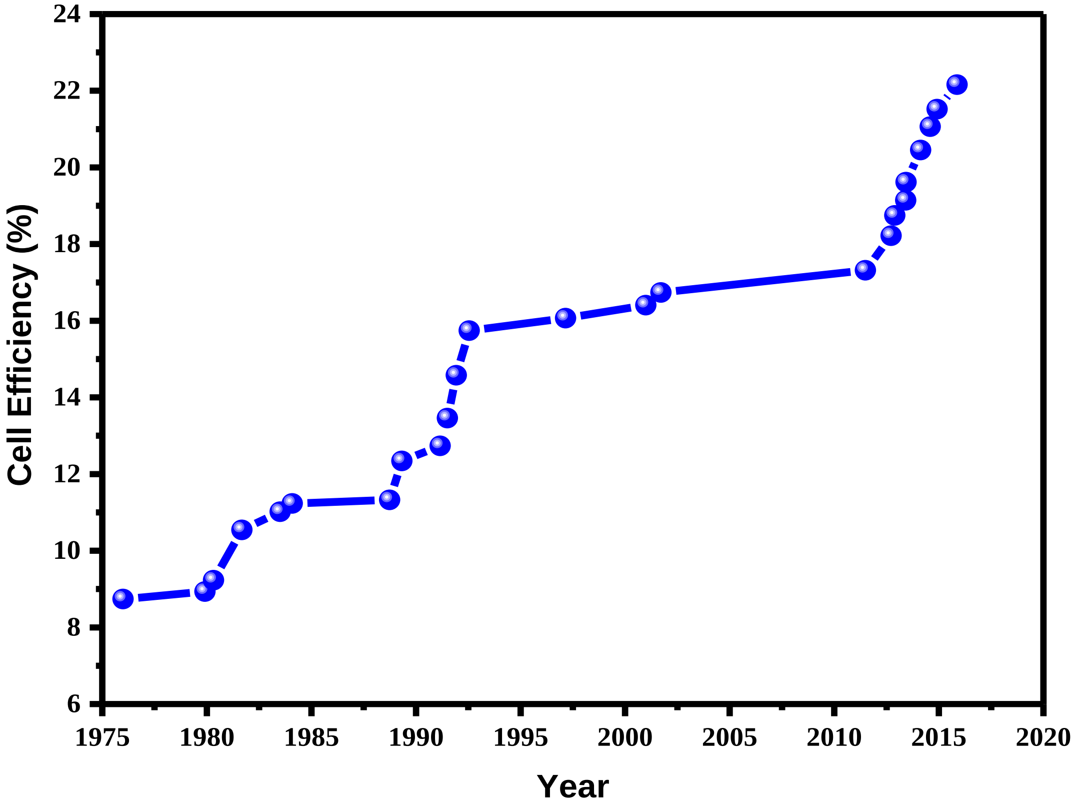

Figure 2.14: Evolution of CdTe thin-film solar cells efficiency over the years. Taken from the NREL efficiency chart [35].

2.5.1 CdS/CdTe solar cell structure

CdS/CdTe solar cells can be produced in two different configurations namely "substrate" or "superstrate" configuration [20,61,103] as illustrated in Figure 2.15. In general, the most commonly used structure is a superstrate configuration because it offers high efficiencies compared to the other configuration. In superstrate structure, the high resistive transparent (HRT), CdS, and CdTe layers are sequentially deposited onto a transparent-conducting oxide (TCO) coated glass substrate (which also serves as the transparent front surface), where the sunlight must pass through the glass in order to reach all layers of the cell, as shown clearly in Figure. 2.15 (left). As for the substrate configuration, it is an inverted structure of the superstrate structure. The CdTe, CdS, HRT, and TCO layers are sequentially deposited onto a substrate as a back surface.

In this configuration, light passes directly through the TCO layer and then reaches all layers of the cell as shown in Figure 2.15 (right). In this work, all investigations of CdS/CdTe solar cells were in superstrate configuration.

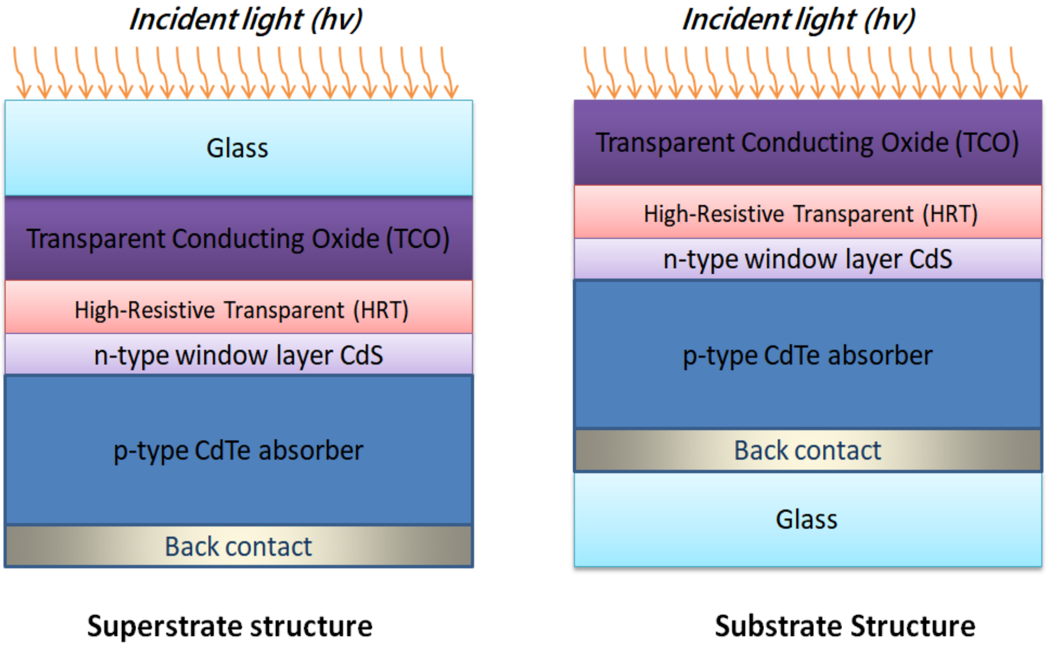

Figure 2.15: Structure of a standard CdTe solar cell in the superstrate and substrate configuration.

A standard structure of superstrate CdS/CdTe solar cells consists of a number of sequential layers, which are as follows:

- ✓ A glass substrate.
- ✓ A transparent-conducting oxide (TCO) serves as the front electrical contact to collect the lateral electric current.
- ✓ A high-resistive transparent (HRT) buffer layer.
- ✓ A window layer CdS acting as the n-type heterojunction partner layer.
- ✓ The p-type CdTe absorber layer to form the p-n heterojunction.
- ✓ A metallic back contact to collect the lateral electric current.

2.5.1.1 Transparent-conducting oxide (TCO) coated glass substrate

Typically, in solar cells, the most prevalent transparent substrate to be used is glass. There are many types of glass, among which soda-lime glass (SLG). The latter is the most common and widely used due to its low cost and sufficient strength to withstand external conditions.

Moreover, it is made by the float glass process making it well suited to thin-film deposition [30]. In addition to SLG, which is utilized at moderate temperatures, aluminosilicate or borosilicate glasses(ASG or BSG) are extensively used in cases that require high temperatures processing [104] but are expensive to fabricate. The SLG used in the superstrate CdS/CdTe solar cells is usually a few millimeters thick ranging from 3 to 3.2 mm [59,105], and as transparent as possible to allow as much light through to the CdTe absorber layer as possible.

On other hand, the heterojunction CdTe/CdS cell requires a transparent conducting oxide (TCO) layer at the front contact. This layer enables photons to access the cell and the active interface is considered as one of the electrodes for collecting current [106]. Among the specifications that must be taken into account in choosing the type of material for the TCO layer are transparency, which should be over 80%, and low resistance. For these reasons, TCO is generally a nearly degenerate doped (heavily doped) semiconductor, which is almost as conductive as a metal. Furthermore, the TCO layer has to be stable at the high process temperatures needed for the manufacture of the cell.

There are several kinds of these materials (TCOs) for CdS/CdTe photovoltaic cells, but the most commonly used are Al-doped ZnO (AZO) [107], tin-doped indium oxide (ITO) [108], and fluorine-doped tin oxide (FTO) [106]. AZO and ITO are known to be thermally unstable at high temperatures suffering from loss of conductivity and, therefore, are not suitable for CdS/CdTe PV due to the high-temperature device processing. So, in large-scale industry, the most used is an FTO due to its better thermal stability, low cost, and ease of manufacture [109].Usually, the thickness of the FTO layer used in CdS/CdTe solar cells is in the range of 100-500 nm.

2.5.1.2 High-resistive transparent (HRT) buffer layer

In high-efficiency CdS/CdTe solar cells, the use of high-resistive transparent (HRT) film between TCO and window layer, CdS would enhance the efficiency by limiting the effect of non-uniformity caused by thin CdS regions [110,111].

Without the HRT layer, if the rough surface of the TCO is applied on glass substrates conventionally, the major thinning of the CdS in order to reduce the parasitic absorption effect and boosts light transmission into the CdTe absorber layer mostly brings about low substrate coverage and hence localized TCO-absorber makes a poor junction, also where some pinholes may be created in the CdS layer leads to a shorting across the heterojunction [77,108]. Hence, these effects cause a reduction in the overall efficiency of the device. To minimize these unwanted effects, an HRT layer is used to reduce the surface roughness of the TCO and therefore, provides a suitable condition for deposition of CdS layers. The undoped Tin Oxide (i-SnO_2) or the undoped Zinc Oxide (i-ZnO) are among the materials used as an HRT layer. Also, there are many types as Zn_2SnO_4, MgZnO, Ga_2O_3 and In_2O_3, etc. In this context, there are various experimental and modeling studies about the effect of HRT on the performance of CdTe solar cells such as those of Williams et al.[108], Womack et al. [73], Baines et al.[103], Mahabaduge et al. [111], Perrenoud et al. [107], Kephart et al.[112], Doroody et al. [77], and Kartopu et al. [113], In general, they reported that incorporation of the HRT layer at the front contact lead to an efficiency boost via the shunt resistance (Rsh), fill factor (FF) and open circuit potential (Voc) parameters.

2.5.1.3 CdS window layer

In a CdTe-based device, an n-type material is also mandatory for creating a good p-n junction, which enables the photovoltaic effect. Cadmium sulfide (CdS) is a good candidate that has demonstrated an excellent capacity, with CdTe having a direct band-gap of ~2.42 eV in the visible spectrum and this value corresponds to an absorption edge close to 500 nm. Since CdS is a transparent material, solar light can penetrate through the CdTe layer and subsequently producing a photovoltaic effect [40,46,114]. A high-efficiency CdTe solar cell needs below 100 nm thickness of thin CdS films, where the use of thin CdS can lead to increased photocurrents and thus improved performance of the device [40,45]. The recommended CdS methods for CdS/CdTe solar cells that have given a good performance are sputtering [47] or CSS [45], which are suitable for large-scale production. Besides, CBD has also shown a good conversion efficiency [46].

2.5.1.4 CdTe absorber layer

To form a heterojunction with the n-type window layer CdS, a p-type CdTe is used as an absorber layer. By considering the material high absorption coefficient (5×10^5 cm^{-1}), a 2-µm-thick of CdTe is enough to absorb 99% of the incident photons with energy greater than the band gap ($E_{photon} \geq Eg_{cdte}$) [53]. However, solar cells are manufactured with a CdTe thickness typically ranging from 2 µm to 6 µm, depending on the deposition methods [115,116]. We have previously mentioned several deposition methods of CdTe material, however, CSS and VTD are the most favorable growth methods for producing high-efficiency polycrystalline CdTe thin-film solar cells [47]. They are the most widely used techniques in laboratories and production lines, which assure a very fast deposition with high crystalline quality.

Over the past twenty years, the doping concentration in typical polycrystalline CdTe has been in the low 10^{14} cm^{-3} range, and carrier lifetimes have been on the order of nanoseconds. Many recent studies have indicated V_{oc} and efficiency enhancements with increased carrier doping and lifetime of CdTe [105,117,118].Therefore, both are considered key to improving the conversion efficiency of CdTe cells. Recent efforts on both single-crystal and polycrystalline CdTe report significant increases in carrier concentration and lifetime beyond the values considered practical in most earlier models [117].

Carrier concentration is of critical importance in solar cell layers since it determines the strength of the field and junctions' position. Therefore, the carrier concentration of the CdTe absorber layer has to be finely controlled to achieve optimum performance while ensuring good stability of the device. Group V dopants such as P [118] and As [119] have demonstrated p-type doping capabilities and have shown a higher doping density (10^{16} -10^{17} cm^{-3}), and producing CdTe devices using these dopants is currently an extensive area of research in the CdTe community [109]. This latest interest in these dopants was after ascertaining the limitations of traditional copper (Cu) doping, where the highest acceptor concentration (regardless of how much Cu is used) does not exceed 10^{15} cm^{-3} only. This low active dopant level is due to severe self-compensation caused by the Cu_i which act as donors in CdTe layers. Additionally, the fast diffusion of Cu within semiconductors can cause long-term device instability [61,119].

On other hand, applications of CdTe in thin-Film solar cells have generally utilized polycrystalline material. The latter, as it is known, consists of many small crystals (the "grains"), and the areas where grains meet are known as grain boundaries (GBs) (see Figure 2.16).

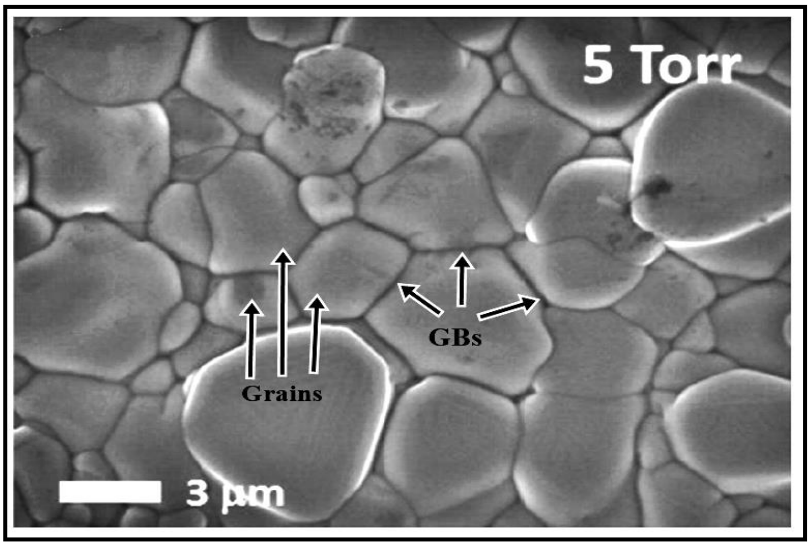

Figure 2.16: SEM images of CSS processed CdTe films grown at the pressure of 5 Torr [47].

These GBs act as recombination centers, which are considered as one of the causes for limiting the carrier lifetime to ~1 ns and low doping concentration in the CdTe absorber layer [119] resulting in deteriorated performances of solar cells. Kanevce et al. [117] and Jensen et al. [120] demonstrated via modeling for the former and experimental results for the latter that CdTe device performances improve with increasing CdTe grain size. Large grains are produced by high-temperature methods such as CSS, meaning the majority of high-efficiency devices utilize CdTe layers deposited via high-temperature methods [109].

2.5.1.5 The heat treatment in a chlorine (Activation)

Heat treatment in the presence of chlorine is an important process in the fabrication of polycrystalline CdS/CdTe solar cells in order to achieve high performance. This process is known as the activation step, and is performed after the deposition of the CdTe layer. This treatment is generally carried out by annealing the layers in the presence of a $CdCl_2$ film on top of CdTe by evaporation or by dipping the CdTe layer in a solution of $CdCl_2$-methanol at 400°C for at least several minutes ranging from 10-30 min [40,121].

In terms of toxicity, a $CdCl_2$ is very toxic, but there are several alternative solutions, such as $MnCl_2$, CsCl, $MgCl_2$, NaCl, etc. They differ in varying degrees in terms of effectiveness. The chlorine treatment reduces problems of doping and carrier lifetime mentioned previously; for more detail, the following points summarize the real role of chlorine heat treatment and its contribution to improving the performance of polycrystalline CdS/CdTe solar cells:

- chloride activation induces crystal regrowth in CdTe thin films which leads to improved crystalline quality, where after treatment the grain size becomes larger than before, thus reducing the grain boundary density and thereby improving performance [40,108].

- Chlorine concentrates along the grain boundaries and passivates them (i.e. acts as a passivating agent on the grain boundaries), reducing the level of recombination [53,104].

- Optimize inter-diffusion and therefore reduce lattice mismatch at the CdS/CdTe junction [47].

- The chlorine plays a role in stabilizing the p-type doping of CdTe forming the A-center, (V_{Cd}–Cl_{Te}). This A-center acts as a single acceptor and removes the mid bandgap V_{Te} states, which acts as a recombination center [109,122].

2.5.1.6 Back contact

As it is known, the work function of a material is defined as the difference between the Fermi level and vacuum level. By another definition, it is the minimum energy required to extract an electron from the Fermi level to the vacuum level. Metals work function is symbolized by ($Ø_m$). The work function of most common metals as measured in vacuum reported from [31] can be found on the left of Figure 2.17 (a), with the energy band diagram of p-CdTe. Through the cadmium telluride layer shown in Figure 2.17, which has an energy band of (E_g= 1.5 eV) and a high electron affinity of (χ_e = 4.28 eV), a back contact to the p-type CdTe would require a material (usually metal) with a work function of $\chi_e + E_g \approx 5.78$ eV to achieve flat-band conditions appropriate for hole transport [123]. As is evident, no metal has a work function $Ø_m \geq 5.78$, and thus a carrier-blocking Schottky barrier $Ø_B$ is inevitably formed at the p-CdTe/metal contact interface (see Figure 2.17 (b)). This metallic interface is calculated using equation (2.1). The formation of a Schottky barrier acts as a reversed biased diode to the CdS/CdTe junction, increasing the back contact resistance. This hole transport barrier when formed at the CdTe/metal interface reduces the carrier collection at the back contact and naturally limits the device performance [124].

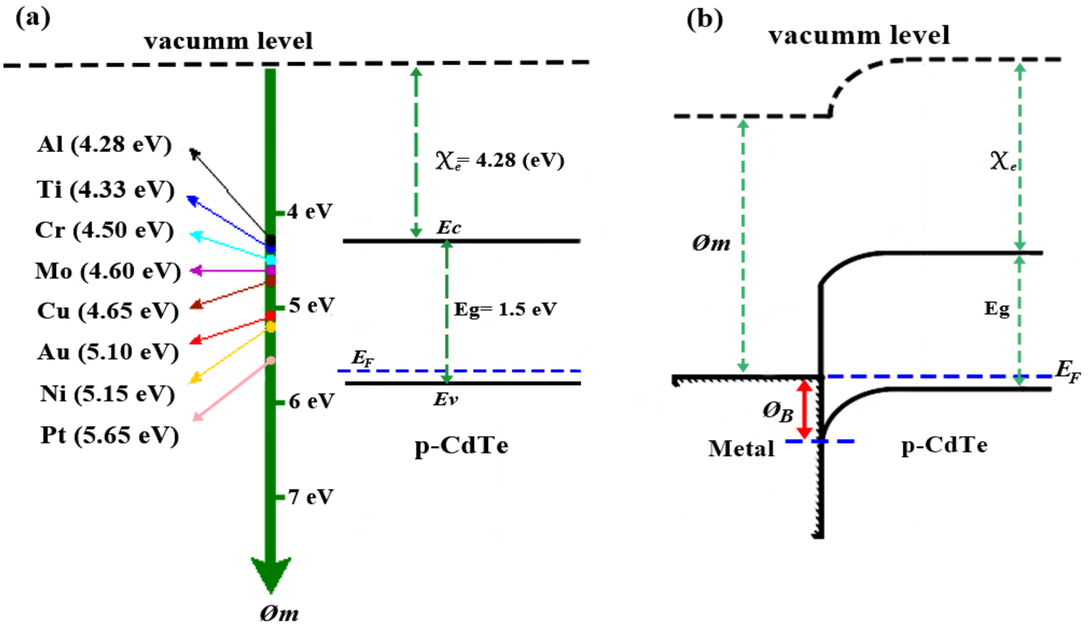

Figure 2.17: Energy band diagram of (a) a group of metals and p-CdTe, (b) a metal and p-CdTe after the contact.

$$Ø_B = \frac{E_g}{q} + (\chi_e - Ø_m) \tag{2.1}$$

Figure 2.18 shows the energy band diagrams with three values of back metal work function $Ø_m$ under illumination. The ideal and desirable situation is an ohmic contact, which is required to achieve a smooth carrier transport, as illustrated in Figure 2.18 (a). However, it is nearly impossible to find such an appropriate metal that has a work function $Ø_m$ greater than that of the CdTe absorber to form an ohmic contact. Therefore, the situations that always occur are are shown in Figure 2.18 (b) and (c). In those cases (Schottky contact), also among the problems that arise and which is considered a detrimental effect on the CdTe cells, a portion of the photo-generated electrons can diffuse to the back and recombine with holes at the back surface [125].

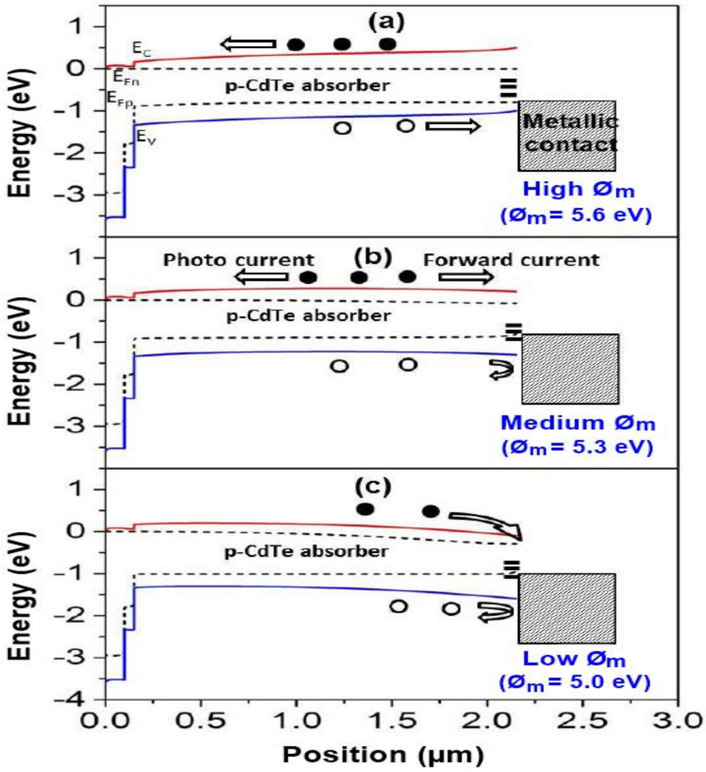

Figure 2.18: Energy band diagrams of CdTe solar cells with different metal work functions $Ø_m$ [125].

In superstrate CdS/CdTe solar cells, gold has a high work function compared to other metals, and due to the diffusivity of copper (Cu) in CdTe, which increases the carrier concentration, back contact is typically made by depositing no more than 5 nm of Cu onto a pre-treated CdTe surface followed by deposition of a metallic electrode (40-50) nm of gold (Au) [47,103,107]. This simple Cu/Au bi-layer proved a good potential in terms of efficiency due to the low Schottky barrier formed. However, this is insufficient. Furthermore, although Cu facilitates the formation of an ohmic contact, it causes instability of the device due to a high diffusion; but the latter is strictly correlated with Cu amount as well as the way of CdTe surface is prepared [126]. Besides, gold is very costly.

Currently, p-CdTe/Metal contacts is one of the major issues and an extensive area of research in the CdTe community. To form ohmic or pseudo-ohmic contacts in CdTe devices, there are several different strategies, among which are:

a) Te-rich back surface by etching

Chemical etching of the CdTe surface is considered one of the solutions to facilitate low resistance contact formation. This process is performed before deposition of the back electrode using dilute Hydrochloric acid (HCl), Bromine-Methanol (Br_2–CH_3OH), or a mixture of nitric and phosphoric acids (HNO_3 and H_3PO_4 (NP)) in water to produce a Te-rich layer., This etching procedure creates a heavily p-doped Te region resulting in a field at the back surface [127–129]. The valence band offset at the p-CdTe/Te interface is small (0.26 eV), which facilitates hole transfer from the absorber layer to the Te layer. And at the same time, it leads to a band bending at the CdTe/Te interface, which acts as the minority-carrier reflector to reduce recombination current on the back surface and at GBs, thus increasing the V_{oc} of the cell [128].

Perhaps this technique can be criticized for increasing the production cost. Furthermore, controlling the etching process is very difficult and can result in over-etched films where shunt resistance decreases dramatically causing shunt paths, thereby degrading device performance [127].

b) Doping

As mentioned earlier, another approach consists in using a few nanometers of Cu between the absorber layer and back electrode to forming a heavily doped p+ region at the back surface to achieve an ohmic contact in CdTe cells [40,61,115]. The inclusion of copper will gradually lower the back-contact barrier for holes, thus allowing current to flow and resulting in the solid band profiles shown schematically in Figure 2.19. The most common is the use Cu with a thickness of no more than 5 nm beside a back electrode of Au (40-50) nm, thus forming a Cu/Au bi-layer [47,103,107]. In this approach, Chou et al. [130] describe the nature of copper in these contacts. In their study of the effect of Cu thickness on cell performance, they observed that both series (R_s) and shunt (R_{sh}) resistances decreased with an increasing Cu thickness. For this reason, the thickness should not exceed 5 nm. However, this is insufficient for optimal performance and causes in the long-term instability of the cell. Alternatively, to form a pseudo-Ohmic contact, arsenic was also utilized for a heavily p doped CdTe as a layer at the rear surface [119].

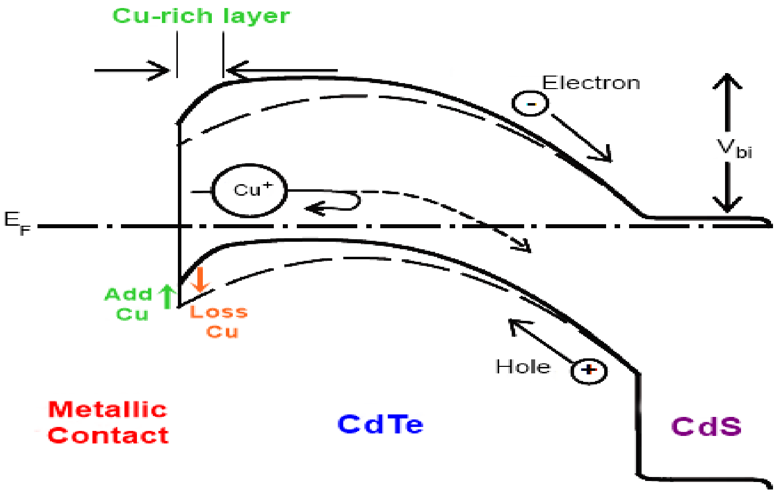

Figure 2.19: CdTe solar-cell band diagram and possible influences from Cu back-contact [131].

c) Interlayer’s

The third solution can provide an alternative solution to address the mentioned challenges and deliver a better contact than the two solutions discussed previously. This method is based on incorporating a layer of another semiconductor as an interlayer between the absorber CdTe layer and the back electrode.

The back interlayer should have a group of fundamental characteristics, including:

- ✓ A good electrical conductivity [20].
- ✓ A low valence-band offset compared to CdTe [132].
- ✓ A high conduction band offset compared to CdTe [132].
- ✓ The lattice mismatch with CdTe must be negligible [105].

The interlayer act as a barrier for the generated electrons, which repels them and thus will return in the direction of the CdS/CdTe heterojunction [20,62,133]. On the other hand, it provides a good hole transport due to the valence-band offset [134]. To understand the role of the interlayer Figure 2.20 shows the band diagram of CdS/CdTe with an interlayer.

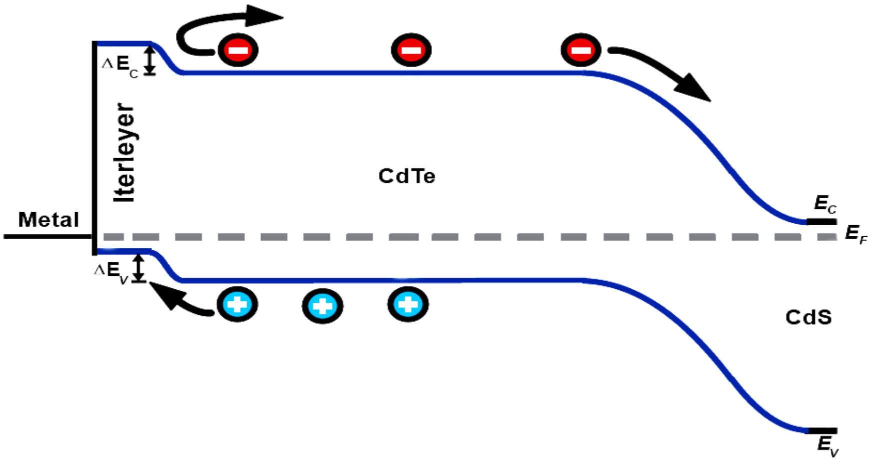

Figure 2.20: Illustration of the CdS/CdTe energy band diagram with an interlayer.

Different successful combinations were realized with this approach that minimizes losses of carriers at the back contact. Moreover, it reduces the carrier recombination at the back contact and thus improves cell efficiency. In the 80s, there were interesting studies regarding the back surface field (BSF) layer and its impact on the efficiency of solar cells [135–137]. In this respect, studies have shown that the use of the hole transport-electron blocking layer (HT-EBL) plays the same role as the (BSF) layer [138]. Also, it contributes to raising the performance of the solar cell. Among the materials used for this mechanism in CdTe solar cells, and which proved a high performance, we can list materials such as ZnTe [51,62,139–143], As_2Te_3 [134,144], Sb_2Te_3 [134,145], V_2O_5 [138,146], Cu_2O [133], Sb_2Se_3 [147].

In particular, a promising candidate material used as an HT-EBL layer in the CdTe solar cells is a cuprous oxide (Cu_2O) having a wide band-gap ranging from 2.1 to 2.61 eV and p-type conductivity [89–92] and a low electron affinity (χ_e=3.3 eV) compared with CdTe.Cu_2O is characterized as a non-toxic material that is easily available, inexpensive, and have a high absorption coefficient in the visible range [148]. J. Türck et al. carried out experimental studies and obtained good results for p-i-n CdTe solar cell using Copper Oxide as a back contact with conversion efficiency of 15.21% [133]. These results indicate that Cu_2O material may be used to enhance the efficiency of CdTe solar cell. In this work, we propose the incorporation of Cu_2O HT-EBL layer in CdTe solar cell to improve the cell performance and investigate the effect of this material, which will be discussed with details in chapter 4.

2.6 Conclusion

This chapter described the II-VI semiconductors and presented the different physical and optical properties of the principal materials, especially those used in this work. Also, we introduced and discussed the traditional structure of CdS/CdTe solar cell devices, which are commonly used in large-scale CdTe solar cells research, with special emphasis on limitations of the CdS/CdTe solar cell, particularly back contact problems, and the solutions possible to decrease this limitation for better conversion efficiency.

CHAPTER 3: Simulation software Silvaco and numerical models

3.1 Introduction

Simulation software for thin-film photovoltaic devices has received a lot of attention in recent years and has become indispensable tools, especially now that they are more mature and realistic than before. To this day, there have been a variety of modeling software developed for thin-film PV devices such as Silvaco, SCAPS, AMPS, AFORS-HET, ASA, etc. They differ in terms of capabilities and limitations, but the fundamental principles remain the same.

Simulation makes it possible to predict the behavior and performance of photovoltaic devices before their manufacture and to visualize the difficult physical phenomena involved in the operation of the component, such as the phenomena of generation and recombination of carriers and the electric field distribution. The operation of a photovoltaic device is modeled by a set of coupled and nonlinear differential equations (the Poisson’s equation, continuity and transport equations). The device is represented by a structure whose electrical and physical properties are discretized onto a mesh of nodes containing data about types of materials, doping profiles in specific regions, boundaries conditions, etc. A device simulator produces numerical solutions by solving the values of the unknowns (concentration of electrons, concentration of holes, potential, etc.) on a mesh of points in the device after internal discretization of the nonlinear equations through different iterative numerical methods.

In this third chapter, we will begin by describing in detail the fundamental equations in semiconductors: the Poisson's equation, the continuity equations, and the transport equations, in addition to the recombination processes, since the majority of semiconductor device simulators are based on it. In a second part, we will present the simulation software TCAD-SILVACO used in our simulation work of the solar cell, its operating mode, and the different commands (instructions) necessary for programming in ATLAS, allowing the reader to get a clear picture of this software.

3.2 Fundamental equations of semiconductors

Decades of research in the physics of semiconductor-based devices have led to the development of mathematical models that are capable of describing the operation of almost any semiconductor device. A fundamental set of equations link the electrostatic potential and the carrier densities within some simulation domains. These equations, which are solved using specific semiconductor device simulation software, are derived from Maxwell's equations. They are mainly: Poisson's equation, the continuity equations, and the transport equations. Poisson's equation relates variations in the electrostatic potential to local charge densities, whereas the continuity and transport equations describe the mode by which the densities of electrons and holes behave according to the processes of transport, generation and recombination [149].

3.2.1 Poisson's equation

Poisson's equation is derived from Coulomb’s law and Gauss’s theorem and is named after the French mathematician and physicist *Simeon-Denis Poisson*. This relationship between the electrostatic potential and local space charge densities is expressed by [14,17]:

$$div(\varepsilon \nabla \psi) = -\rho \tag{3.1}$$

Where ψ is the electrostatic potential, ε is the local permittivity, and ρ is the local space charge density.

The space charge in a semiconductor is determined by both the ionized impurity concentrations (N_D^+ and N_A^-) and the carrier concentrations (n and p).

$$\rho = q(p - n + N_D^+ - N_A^-) \tag{3.2}$$

The electric field is given by the relation:

$$\vec{E} = -\overrightarrow{grad}(\psi) \tag{3.3}$$

3.2.2 Continuity equations

Also of the basics are the continuity equations for electrons and holes. The continuity equation describes a basic concept, namely that a change in carrier density over time is due to the difference between the incoming and outgoing flux of carriers plus the generation and minus the recombination. The continuity equations for electrons and holes are expressed as [14,17]:

$$\frac{\partial n}{\partial t} = +\frac{1}{q} div \vec{J_n} + G_n - R_n \tag{3.4}$$

$$\frac{\partial p}{\partial t} = -\frac{1}{q} div \vec{J_p} + G_p - R_p \tag{3.5}$$

where n, $\vec{J_n}$, G_n, R_n are the electron concentration, current density, generation rate, and recombination rate, respectively. p, $\vec{J_p}$, G_p, R_p are hole concentration, current density, generation rate, and recombination rate, respectively.

3.2.3 Transport equations

Besides the fundamental equations (3.1), (3.4) and (3.5), which provide the general framework for device simulation, however, they are insufficient and need secondary equations to specify particular physical models with the mechanisms that govern them for $\overrightarrow{J_{p,n}}$, $G_{p,\mathrm{n}}$, and $R_{p,\mathrm{n}}$. The current density equations, or charge transport models, are usually derived from the Boltzmann Transport Equation. Among the simplest of these transport models are the drift-diffusion model, which is adequate for nearly all technologically feasible devices [14].

As is known, electrical currents are generated in a semiconductor due to the transport of charge by electrons and holes. The two basic transport mechanisms in a semiconductor are drift and diffusion. These last two mechanisms that we consider in this section are basic transport mechanisms in a semiconductor crystal, where drift is the movement of charge due to electric fields, and diffusion is the flow of charge due to density gradients.

3.2.3.1 Drift

The Drift mechanism is charged-particle motion in response to an electric field. In an electric field, the force $(\vec{F}=q\vec{E})$ acts on the charged particles in a semiconductor, which accelerates the positively charged holes in the direction of the electric field and the negatively charged electrons in the direction opposite to the electric field. The net drift of charge gives rise to a drift current. The resulting motion of electrons and holes can be described by average drift velocities $\vec{v}_{dn}$ and $\vec{v}_{dp}$ for electrons and holes, respectively. In the case of low electric fields, the average drift velocities are directly proportional to the electric field as given by [150]:

$$\vec{v}_{dn} = -\mu_n \vec{E} \tag{3.6}$$

$$\vec{v}_{dp} = \mu_p \vec{E} \tag{3.7}$$

where μ_n and μ_p are the electron and hole mobilities respectively.

In spite of the electrons moving in the opposite direction to the electric field, because the charge of an electron is negative, the resulting electron drift current is in the same direction as the electric field. The electron and hole drift current densities $(\vec{J}_{n,p.drift})$ are given as [150]:

$$\vec{J}_{n.drift} = -q.n.\vec{v}_{dn} = q.n \cdot \mu_n \vec{E} \tag{3.8}$$

$$\vec{J}_{p\cdot drift} = q \cdot p \cdot \vec{v}_{dp} = q \cdot p \cdot \mu_p \vec{E} \tag{3.9}$$

3.2.3.2 Diffusion

The second mechanism that can also generate a current in a semiconductor is the Diffusion. It is a process whereby particles tend from regions of high concentration toward regions of low concentration as a result of random thermal motion. Thus the currents due to from diffusion are proportional to the gradient in particle concentration, and this is what Fick's law of diffusion describes. The diffusion current for electrons and holes are can be given by [150]:

$$\vec{J}_{n.diff} = qD_n \nabla n \tag{3.10}$$

$$\vec{J}_{p.diff} = -qD_p \nabla p \tag{3.11}$$

where D_n and D_p are the electron and hole diffusion coefficients, respectively, and are defined by Einstein's relation [17,150]:

$$D_n = \frac{kT}{q}\mu_n \tag{3.12}$$

$$D_p = \frac{kT}{q}\mu_p \tag{3.13}$$

By combining these two types of currents together (Drift and Diffusion current), we come up with the following expressions for the total current density for electrons and holes:

$$\vec{J_n} = qn\mu_n\vec{E} + qD_n \nabla n \tag{3.14}$$

$$\vec{J_p} = qp\mu_p\vec{E} - qD_p \nabla p \tag{3.15}$$

3.2.4 Recombination process

When a semiconductor is taken out of thermal equilibrium, for instance by illumination, incident photons lead to the generation of EHP, which are named as carriers. The electron present in the CB is in a meta-stable state and is stabilized to a lower energy position in the VB. When the electron stabilizes back down to the VB, it effectively removes the hole. Eventually, electrons lose energy and stabilize back to the VB, recombining with a hole. Consequently, this process which is called recombination, acts to restore the non-equilibrium light generated EHP population to its thermal equilibrium value.

In solar cells, these generated carriers must be separated before recombination and emission of energy occur. As we discussed in Chapters 1 and 2, recombination affects the overall efficiency of a solar cell, which is considered the major cause of the loss of photo-generated carriers, and thus performance of cells is reduced. Recombination occurs spatially in the different regions of a solar cell. The generated carriers in proximity to the depletion region are separated by the electric field of the depletion region, whereas generated carriers in a solar cell at the bulk, front and far end have a less probability to get separated. Thus, generated carriers in these regions will again recombine with the emission of absorbed energy, and they will not contribute in the photovoltaic process [151]. So, key to improving the efficiency of solar cells is governing the recombination of the carriers. This phenomenon results in the release of energy, which stems from electrons jumping down from the CB to the VB, where this quantum of energy is equal to the difference of its original (E_c) and its final state (E_v). This can be done in three ways:

- Emit a photon (radiative recombination)
- kinetically excite another electron (Auger recombination)
- Emit a phonon (non–radiative recombination)

As we mentioned in Chapter 1, there are principally two types of recombination the recombination mechanisms in bulk (volume) and the surface recombination.

3.2.4.1 Recombination mechanisms in a bulk semiconductor

Recombination mechanisms in bulk semiconductors are of three different types:

1) Radiative or band-to-band recombination.

2) Auger recombination.

3) Non-radiative or indirect recombination (often referred to as Shockley-Read-Hall recombination (SRH)).

In fact, all three recombination mechanisms in bulk occur at the same time. These different processes are schematically illustrated in Figure 3.1.

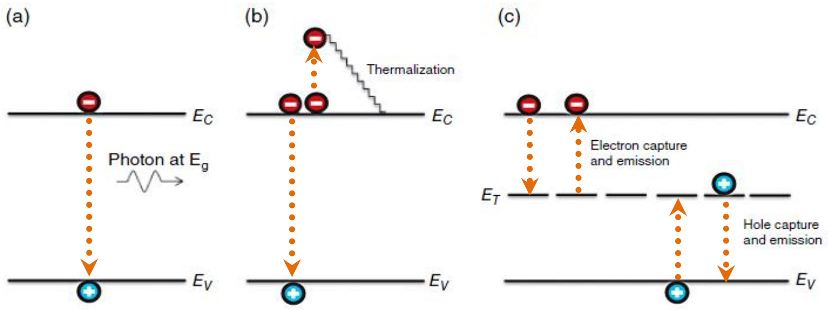

Figure 3.1: Carrier recombination mechanisms in semiconductors; (a) Radiative recombination, (b) Auger recombination, (c) Non-radiative recombination (SRH) [150].

3.2.4.1.1 Radiative recombination

Radiative recombination (or band-to-band recombination) in this mechanism, a free-electron falls directly from the CB to the VB with dissipation of the excess energy in the form of a photon as shown in Figure 3.1 (a). The energy of the emitted photon corresponds to the energy bandgap of the material. The radiative (optical) recombination process was described by the standard relation [14,30]:

$$U_r = B_r\left(np - n_i^2\right) \tag{3.16}$$

where B_r is the radiative recombination coefficient (cm^3/s), we can activate this process in Silvaco ATLAS in the `MODELS` statement by calling `OPTR` and by defining `COPT` in the `MATERIALS` statement.

3.2.4.1.2 Auger recombination

In contrast to radiative recombination, Auger recombination is a non-radiative mechanism in which the energy of the photogenerated carrier is dissipated not by photon emission but rather by its transfer to another electron or hole. If the third particle is an electron, it is excited into higher levels in the CB. This excited electron relaxes again, transferring its energy to vibrational energy of the lattice, or phonon modes, and finally thermally as illustrated in Figure 3.1 (b). Likewise, if the third particle is a hole, it is excited into deeper levels of the valence band, from where it rises back to the VB edge by transferring its energy to phonon modes. The expression for the net recombination rate due to Auger processes is [30]:

$$R_{Auger} = C_n\left(n^2p - nn_{ie}^2\right) + C_p\left(p^2n - pn_{ie}^2\right) \tag{3.17}$$

where C_n and C_p (cm^6/s) are Auger coefficients of electrons and holes respectively. In the simulation, the Auger recombination rate R_{Auger} is modeled in ATLAS as follows [14]:

$$R_{Auger} = AUGN\left(n^2p - nn_{ie}^2\right) + AUGP\left(p^2n - pn_{ie}^2\right) \tag{3.18}$$

We can invoke this process in the `MODELS` statement by calling `AUGER` and by defining `AUGN` and `AUGP` in the `MATERIALS` statement.

3.2.4.1.3 Non-radiative (Shockley-Read-Hall) recombination

Experimentally, it is not easy to grow semiconductors with extremely high purity. Therefore we find that most semiconductors contain some degree of impurities or vacancies that are incorporated into the crystal structure through material growth. These impurities cause spatially localized defect levels typically near the middle of the bandgap of the bulk semiconductors and are referred to as trap states or recombination centers. These energy levels within the bandgap are denoted as E_T as shown in Figure 3.1 (c). The electron falls from the CB to the defect level and then from the defect level to the VB, and the excess energy (E_C–E_T) and (E_T–E_V) are usually dissipated in the form of heat. This type of recombination normally dominates the net recombination rate in semiconductors devices in general and especially in solar cells. This recombination process theory was first derived by *W B. Shockley*, *W T. Read* and *R N. Hall* in 1952, therefore it is usually called as Shockley-Read-Hall (SRH) recombination [150]:

$$R_{SRH} = \frac{pn - n_i^2}{\tau_{n0}\left[p + n_{ie}\exp\left(\frac{E_i - E_T}{KT}\right)\right] + \tau_{P0}\left[n + n_{ie}\exp\left(\frac{E_T - E_i}{KT}\right)\right]} \tag{3.19}$$

where τ_{n0} and τ_{p0} are electron and hole lifetimes, respectively. Based on the Shockley-Read-Hall expression, ATLAS uses this model by calling `SRH` in the `MODELS` statement, and as for the carrier lifetimes, we can set it in the `MATERIALS` statement by the `TAUN0` and `TAUP0` parameters which represent electrons and holes lifetimes.

3.2.4.2 Surface recombination

This kind of recombination, occurs at surfaces and interfaces where it can have a significant effect on the behavior of semiconductor devices. Surface recombination occurs due to dangling bonds at the surface of a semiconductor (see Figure 3.2 (a)). This abrupt discontinuity of the lattice introduces a large number of energy states called surface states. These act as recombination centers, where excited electrons in the conduction band recombine with holes in the valence band via these surface states (Figure 3. 2 (b)).

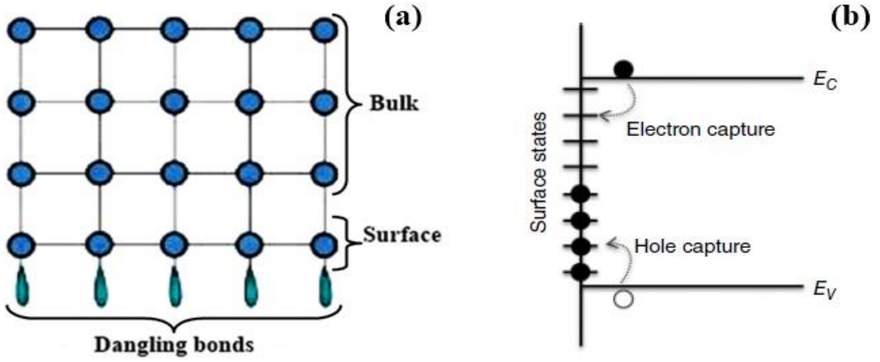

Figure 3.2 (a) Dangling bonds on a semiconductor surface, (b) Electron and hole capture at the surface of a semiconductor [150].

The standard model of surface recombination that represent this mechanism is very similar to R_{SRH}, which is given by the following expression [14]:

$$R_{surf} = \frac{pn - n_i^2}{\tau_n^{eff}\left[p + n_{ie}\exp\left(\frac{E_i - E_T}{KT_L}\right)\right] + \tau_p^{eff}\left[n + n_{ie}\exp\left(\frac{E_T - E_i}{KT_L}\right)\right]} \tag{3.20}$$

where the τ_n^{eff} and τ_p^{eff} are the effective lifetimes and are given as [14]:

$$\frac{1}{\tau_n^{eff}} = \frac{1}{\tau_n^i} + \frac{d_i}{A_i} S_n \tag{3.21}$$

$$\frac{1}{\tau_p^{eff}} = \frac{1}{\tau_p^i} + \frac{d_i}{A_i} S_p \tag{3.22}$$

τ_n^i and τ_p^i are the bulk lifetime calculated at node i, d_i and A_i are the length and area of the interface for node i. The S_n and S_p are the surface recombination velocities for electrons and holes respectively,

$$S_n = \sigma_n v_{th} N'_{st} \tag{3.23}$$

$$S_p = \sigma_p v_{th} N'_{st} \tag{3.24}$$

where N'_{st} *is* surface state density , σ_n an σ_p are the capture cross-sections for electrons and holes, respectively and v_{th} is the thermal velocity.

3.3 Silvaco

Silvaco is an American company (SilVaCo: Silicon Valley Corporation) that specializes in the creation of simulation software. Founded by Dr. Ivan Pesic in 1984, and in early 1987 Silvaco entered into the Technology Computer Aided Design (TCAD) market. By 1992 Silvaco became the dominant TCAD supplier with the Athena process simulator and Atlas device simulator [152]. Silvaco-TCAD is a 2D / 3D simulator software with tools that allow it to model not only the electrical, optical and thermal behavior of devices but also the manufacturing processes such as deposition, etching, and doping by implantation or diffusion, oxidation, etc.) of semiconductor-based components. Consequently, these simulations make it possible to optimize the various manufacturing parameters and to predict the behavior of semiconductor devices, in particular solar cells. These tools can be classified into two categories: core tools and interactive tools (see Figure 3.3).

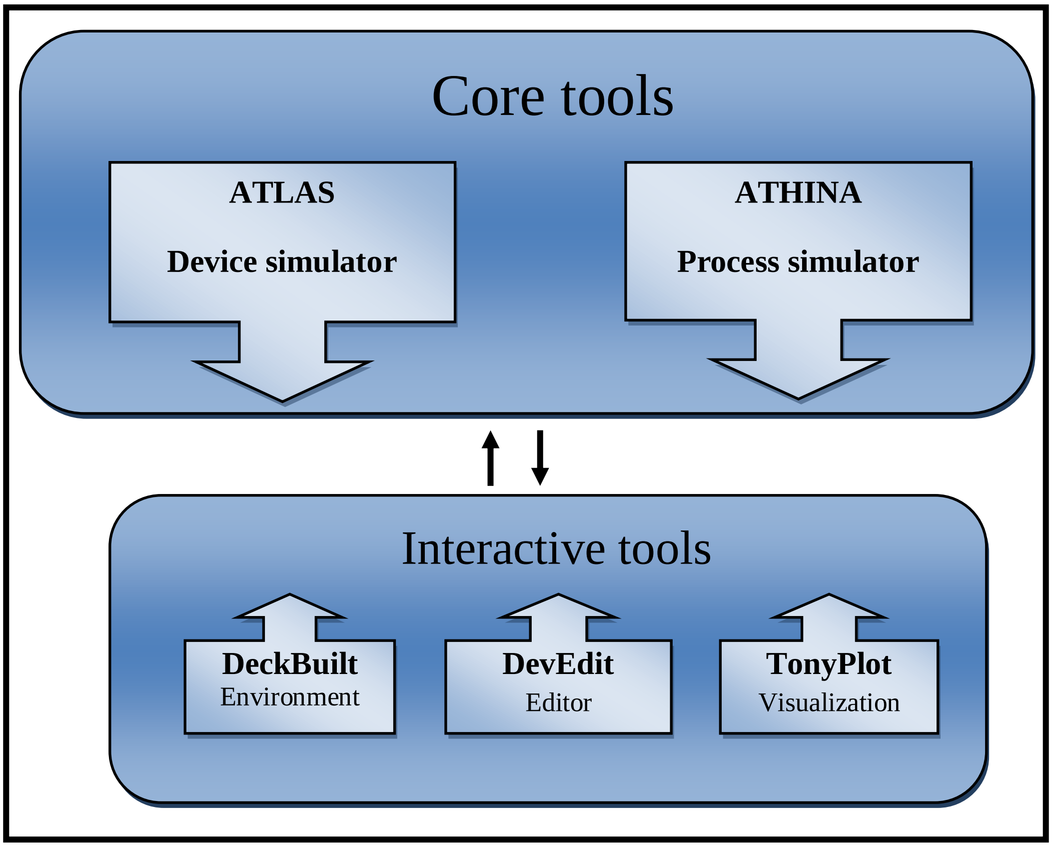

Figure 3.3: The main tools in Silvaco-TCAD.

3.3.1 Core tools

Both emulators ATLAS and ATHENA are performing the functions for which they are intended. For example, Atlas simulates in 2D and 3D the electrical characteristics of the semiconductor devices. As to ATHENA, it simulates in 1D and 2D all manufacturing processes.

3.3.2 Interactive tools

These are tools allow us to communicate with the simulators and visualize the results obtained. Among them, we mention DeckBuild, DevEdit, and TonyPlot.

- **DeckBuild:** is an interactive, graphic runtime environment for developing process and device simulation input decks. It is considered as the main window of Silvaco it allows to write commands to be executed and visualize the results of the code execution. One can also define the structure and its mesh. An example of a Deckbuild window is shown in Figure 3.4.

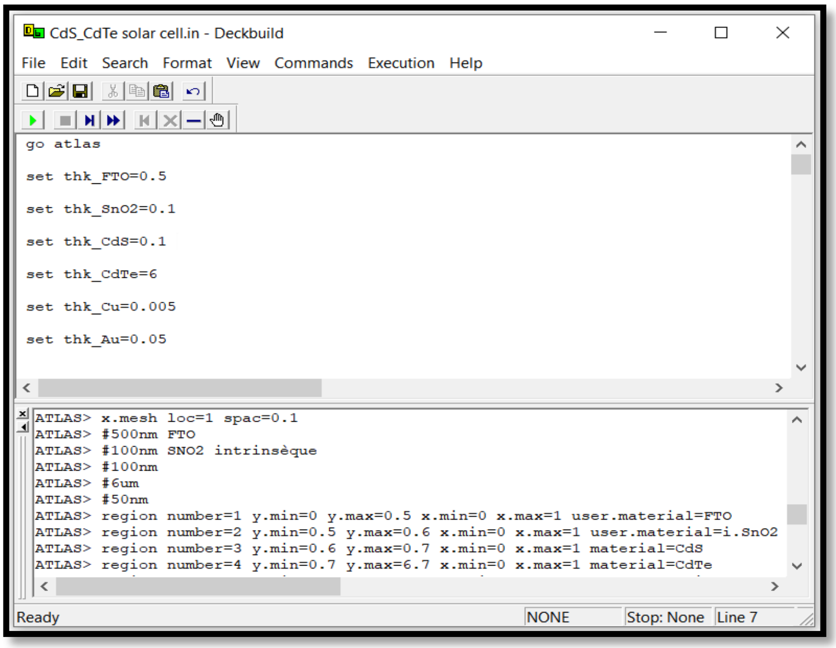

```
go atlas

set thk_FTO=0.5

set thk_SnO2=0.1

set thk_CdS=0.1

set thk_CdTe=6

set thk_Cu=0.005

set thk_Au=0.05
```

```
ATLAS> x.mesh loc=1 spac=0.1
ATLAS> #500nm FTO
ATLAS> #100nm SNO2 intrinsèque
ATLAS> #100nm
ATLAS> #6um
ATLAS> #50nm
ATLAS> region number=1 y.min=0 y.max=0.5 x.min=0 x.max=1 user.material=FTO
ATLAS> region number=2 y.min=0.5 y.max=0.6 x.min=0 x.max=1 user.material=i.SnO2
ATLAS> region number=3 y.min=0.6 y.max=0.7 x.min=0 x.max=1 material=CdS
ATLAS> region number=4 y.min=0.7 y.max=6.7 x.min=0 x.max=1 material=CdTe
```

Figure 3.4: The main window of DeckBuild.

- **DevEdit:** is a graphical editor that allows for structure editing, structure specification, and mesh generation.
- **TonyPlot:** is a visualization tool which plots the results of simulation. The data can be plotted as desired by the user either in 1D x-y data, 2D contour data, Smith charts or polar charts. With the possibility of importing the measured data as well.

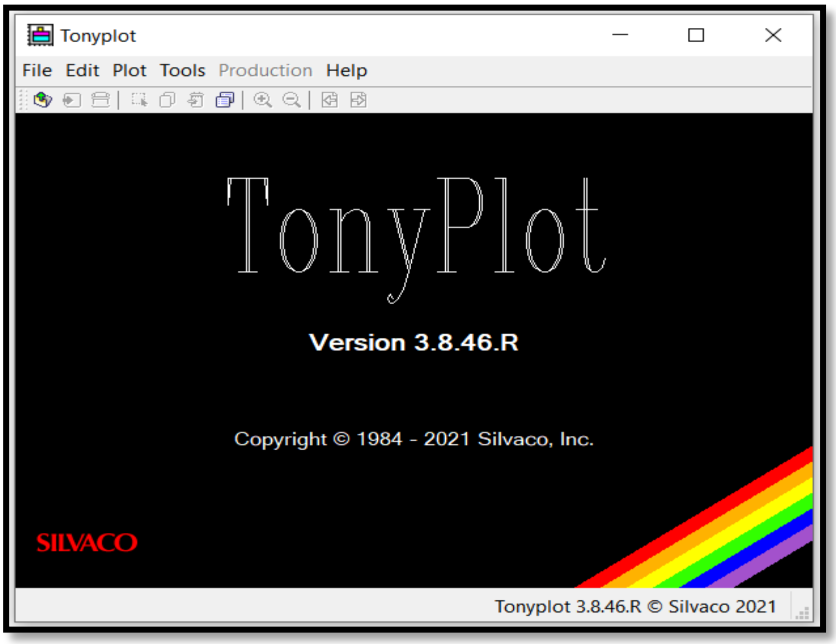

Figure 3.5: TonyPlot main window.

In this work, we used ATLAS simulator, which allows the prediction of the electrical, optical, and thermal behaviors of solar cells. So in this chapter, we will focus on the Atlas simulator and how it works.

3.3.3 ATLAS simulator

Atlas is a physically-based device simulator. Physically-based device simulators predict the electrical characteristics that are associated with specified physical structures and bias conditions. This is achieved by approximating the operation of a device onto a two or three-dimensional grid, consisting of a number of grid points called nodes. By applying a set of differential equations derived from Maxwell's laws onto this grid, we can simulate the transport of carriers through a structure. This means that the electrical performance of the device can be modeled in DC, AC, or transient modes of operation [14].

In Atlas, specify device simulation problems by defining [14]:

- The physical structure to be simulated.
- The physical models to be used.
- The bias conditions for which electrical characteristics are to be simulated.

To define a device through the Atlas command language, we must first define a mesh. This mesh or grid covers the physical simulation domain. The mesh is defined by a series of horizontal and vertical lines and the spacing between them. Then, regions within this mesh are allocated to different materials as required to construct the device. After the regions are defined, the location of electrodes is specified. The final step is to specify the doping in each region [14].

3.3.3.1 Atlas inputs and outputs

Figure 3.6 shows the types of information inputs and outputs that flow in and out of the Atlas.

- **Input files:** Most Atlas simulations use two input files, the first input file (Structure *Files*) is a text file that contains commands for Atlas to execute. As for the second input file (*Command File*), it is the structure file that defines the structure that will be simulated.
- **Outputs files:** On the other hand, Atlas produces three types of output files. The first type of output file is the *run-time output*, which gives us the progress and the error and warning messages as the simulation proceeds. The second type of output file is the *log file*, which stores all terminal voltages and currents from the device analysis. The third type of output file

is the *solution file*, which stores two-dimensional (2D) and three-dimensional (3D) data relating to the values of solution variables within the device at a given bias point [14]. The last two output files (*Log Files* and *Solution Files*) are processed by the *TonyPlot* visualization tool, which allows visualizing the results of the simulations (structure of the component, electrical characteristics, and all other physical quantities).

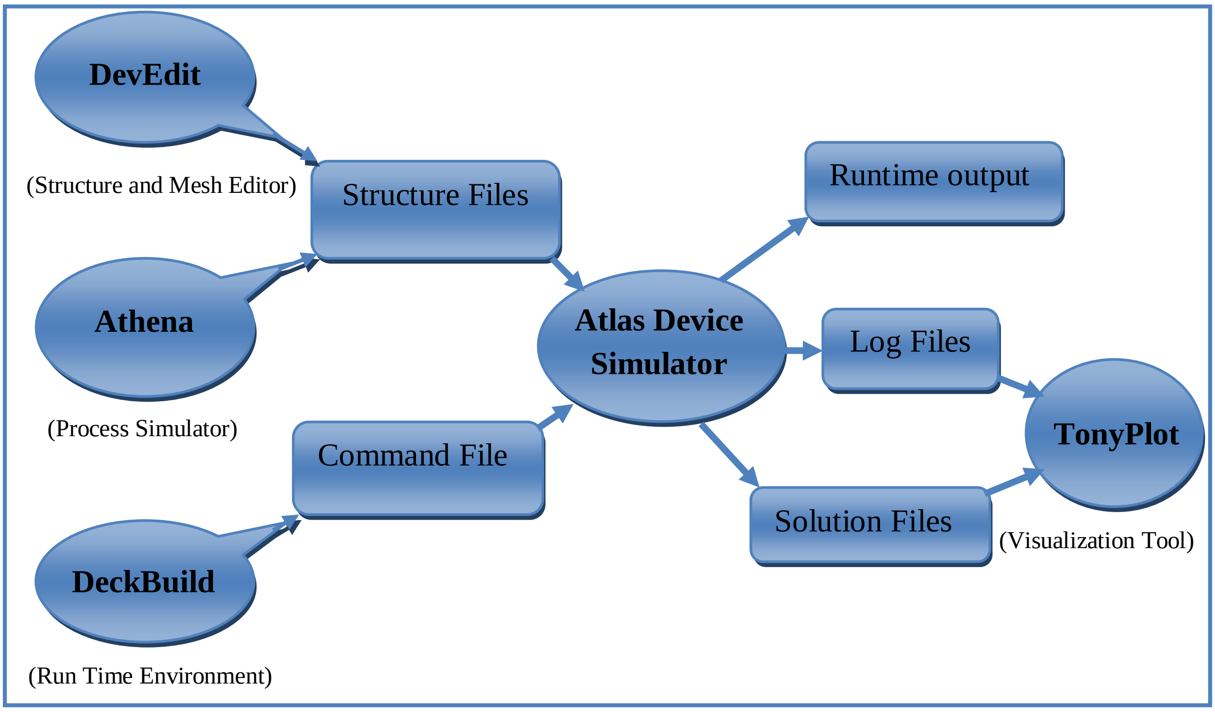

Figure 3.6: ATLAS inputs and outputs.

3.3.3.2 The order of Atlas commands

To run Atlas inside Deckbuild, the code must be started with the statement `go atlas`, also a single input file may contain several Atlas runs each separated with a go atlas line.

Following that command, the input file needs five groups of statements that must occur in the correct order, illustrated in Figure 3.7. The order in which statements occur in an Atlas input file is important. Otherwise, an error message will appear which may cause incorrect operation or termination of the program. For example, if the material parameters or models are set in the wrong order, then they may not be used in the calculations. The order of statements within the mesh definition, structural definition, and solution groups is also important. Otherwise, it may also cause incorrect operation or termination of the program [14].

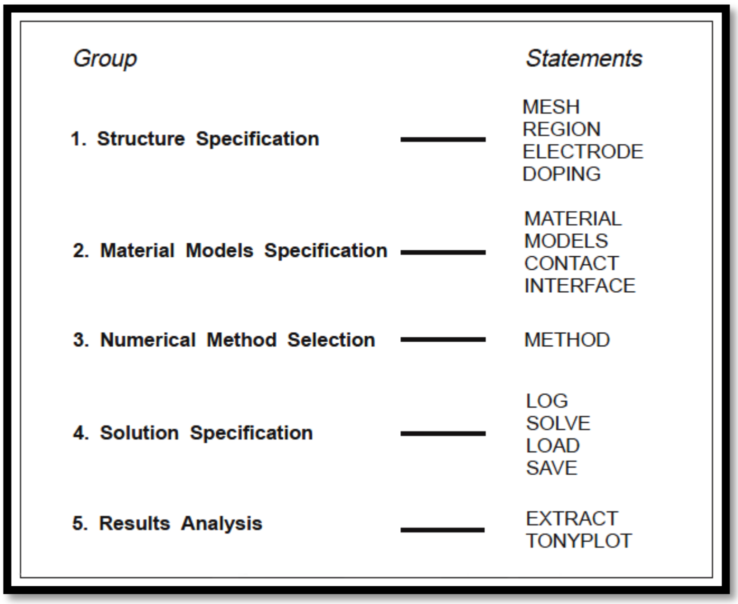

Group	*Statements*
1. Structure Specification	MESH REGION ELECTRODE DOPING
2. Material Models Specification	MATERIAL MODELS CONTACT INTERFACE
3. Numerical Method Selection	METHOD
4. Solution Specification	LOG SOLVE LOAD SAVE
5. Results Analysis	EXTRACT TONYPLOT

Figure 3.7: Atlas command groups with the primary statements in each group [14].

Each statement consists of a keyword that identifies the statement and a set of parameters. The general format is [14]:

```
<STATMENTS> <PARAMETER > = <VALUE>
```

For any `<STATEMENT>,` Atlas may have four different types for the `<VALUE>` parameter. These are: Real, Integer, Character, and Logical.

3.3.3.2.1 Structure specification

Structure specification contains four statements that include generation of mesh, defining regions and electrodes and doping levels for the device.

a) Mesh

The mesh consists of horizontal and vertical lines with a user-defined distance between them. It bounds the physical area of the device by creating a number of triangles in which the simulation will take place. Mesh specification also involves a tradeoff between accuracy and numerical efficiency. A fine defined mesh will lead to more accurate results, and on the other hand, a coarse mesh that minimizes the total number of grid points will lead to a larger numerical efficiency. Vertical and Horizontal mesh division, in microns, is specified with `x.mesh` and `y.mesh` commands and their associated spacing. The default value for the mesh scaling factor is one but can be changed at will.

The general format to define the mesh is through the following statements:

```
x.mesh location= <VALUE>   spacing= <VALUE>
y.mesh location= <VALUE>   spacing= <VALUE>
```

A coarse or fine mesh determines the accuracy of the simulation. A coarse mesh produces a faster simulation but less accurate results. A fine mesh produces a slower simulation but more accurate results. Therefore, the areas that have a finer mesh are of greatest interest in the simulation. Atlas sets some limits on the maximum number of grid nodes that can be used. But this shouldn't be viewed as a bottleneck to achieving simulation results. In the default version, 2D simulations have a maximum node limit of 100,000. 3D simulations have an upper limit of 40,000,000 nodes with no more than 100,000 nodes in any one Z plane and a maximum number of Z planes of 2,000 [14]. An example of the mesh statements is shown in Figure 3.8.

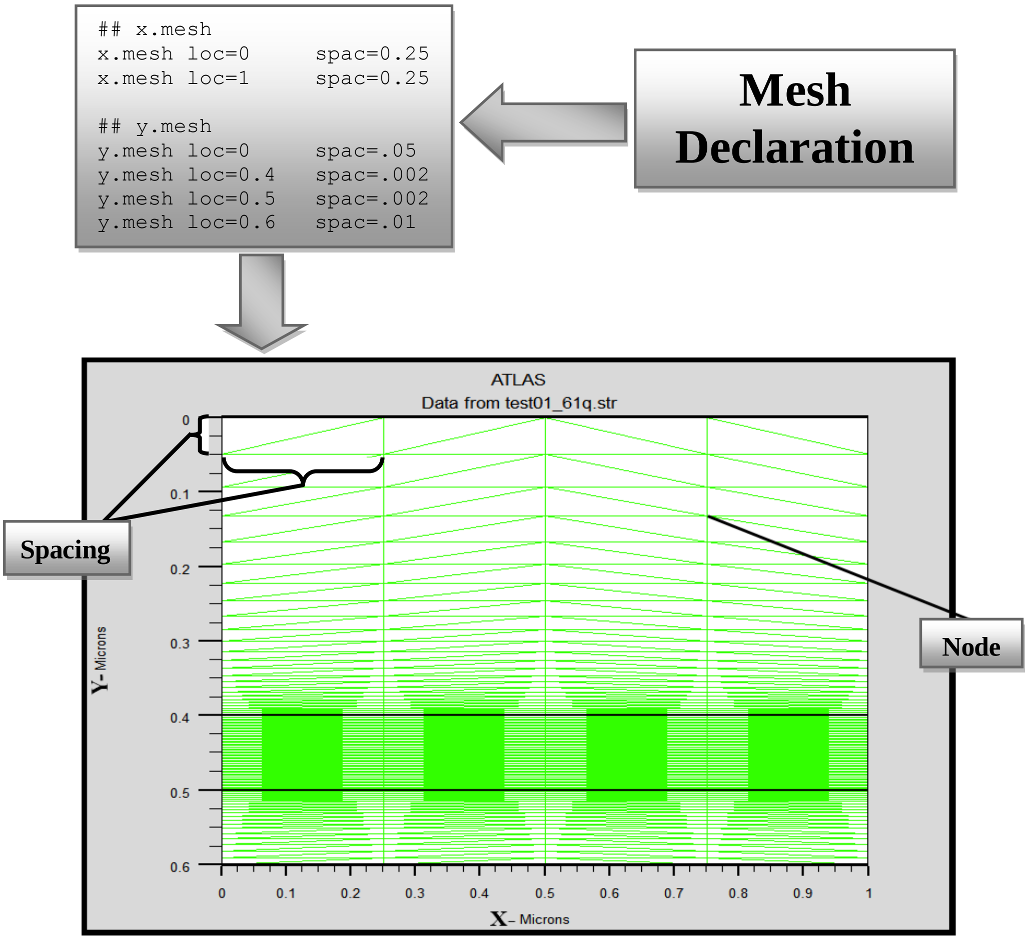

```
## x.mesh
x.mesh loc=0     spac=0.25
x.mesh loc=1     spac=0.25

## y.mesh
y.mesh loc=0     spac=.05
y.mesh loc=0.4   spac=.002
y.mesh loc=0.5   spac=.002
y.mesh loc=0.6   spac=.01
```

Figure 3.8: Meshing example in atlas.

Can be defined a third dimension Z by the width parameter. The WIDTH is the device width (the width of the layers) in microns defined on the MESH statement, and this value is considered as 1 µm by default. We can change that in the MESH statement which is defined as follows:

```
mesh width= <VALUE>
```

So in this case, the surface of the device is S=[x] × [width].

b) Regions

After defining the mesh, the next step is to determine the material type for every part. All locations of the mesh are divided into numbered areas, where each is associated with a specific material. One should take into consideration that the maximum regions that can be defined in atlas is 15000 [14]. The region numbers must start at 1 and are increased for each subsequent region statement. The format to define the regions is as follows:

```
REGION number=<integer> <material_type> <position parameters>
```

The position parameters are specified in microns using the `y.min`, `y.max`, `x.min`, and `x.max` parameters. For example, Figure 3.9 presents a structure consisting of four materials different created by Atlas.

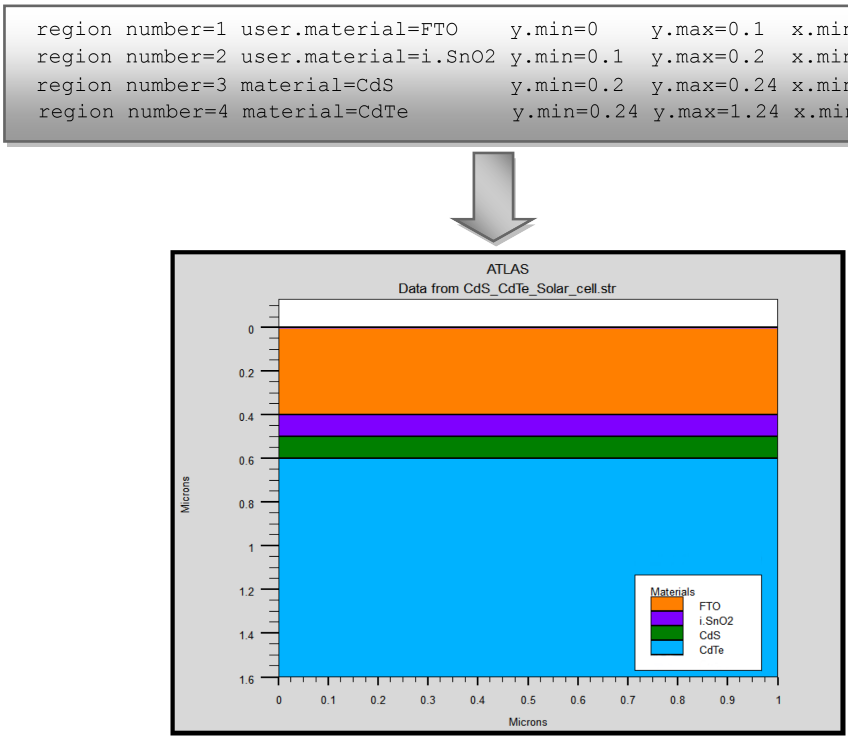

```
region number=1 user.material=FTO    y.min=0    y.max=0.1  x.min=0 x.max=1
region number=2 user.material=i.SnO2 y.min=0.1  y.max=0.2  x.min=0 x.max=1
region number=3 material=CdS         y.min=0.2  y.max=0.24 x.min=0 x.max=1
region number=4 material=CdTe        y.min=0.24 y.max=1.24 x.min=0 x.max=1
```

Figure 3.9: Schematic diagram example of a structure consisting of four regions created by Atlas.

c) Electrode

The next step is to define the electrodes of the device, their position and size must be entered. At least one electrode that contacts a semiconductor material must be defined.

The format to define electrodes is as follows:

```
ELECTRODE NAME=<ELECTRODE NAME> <POSITION_PARAMETERS>
```

Up to 50 electrodes can be specified. The position parameters are specified in microns using the `y.min`, `y.max`, `x.min`, and `x.max` parameters. Otherwise, the `BOTTOM` and `TOP` statements can be used to specify electrode placement along the bottom or top of the device, respectively. Also, additional information about their materials and work functions can be provided if necessary.

d) Doping

The last aspect of structure specification is about defining doping profiles for each region of the device, which can be specified either analytically or from an input file. The `doping` statement is used to define doping profiles, which should contain the distribution type of doping that can be Gaussian or Uniform, the doping concentration, the dopant type n or p-type, and the position parameters. The format of the DOPING statement is as follows:

```
Doping<distribution type> <dopant_type> <position parameters>
```

For position parameters, can be define by `y.min`, `y.max`, `x.min`, and `x.max` or by material type or by region number. Figure 3.10 is a clear example of doping by atlas.

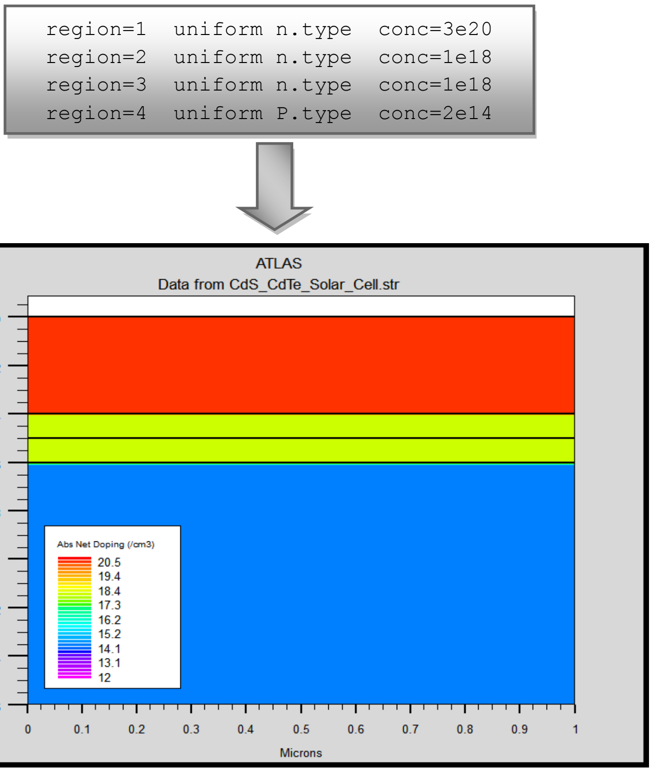

```
region=1  uniform n.type  conc=3e20
region=2  uniform n.type  conc=1e18
region=3  uniform n.type  conc=1e18
region=4  uniform P.type  conc=2e14
```

Figure 3.10: Atlas doping.

3.3.3.2.2 Materials model specification

After defining the specification of the structure, the turn comes on material parameters, physical model, the contact and interface specification must be given in this sequence to Atlas used during the device simulation. Therefore the material model specification is divided into four main statements.

a) Material

As we know, all materials are split into three classes: semiconductors, insulators, and conductors. Each class requires a different set of parameters to be specified. For semiconductors, these properties include a lot of parameters such as band gap, electron affinity, density of states, etc. [14]. There are default parameters for material properties used in device simulation for many materials but it is better to define the parameters manually. If a material does not exist, then it must be defined with the name of existing material using its own parameters values instead of the values of the existing material. The format for the material statement is as follows:

```
MATERIAL <LOCALIZATION> <MATERIAL_DEFINITION>
```

The localization can be defined by region if for example the same material constitutes several but with different parameters such as semiconductor with different alloy composition, or it can be done with the material statement, for example:

```
MATERIAL MATERIAL=CdTe EG300=1.5
```

Various other parameters can be defined as the material statement. Examples of these parameters are listed in the next table.

Table 3.1: Different parameters of the material statement in Atlas Silvaco.

Parameter	Description	Units
Eg300	Specifies energy gap at 300 K	(eV)
Nc300	Specifies the conduction band density of state at 300 K	(cm^{-3})
Nv300	Specifies the valence band density of state at 300 K	(cm^{-3})
AFFINITY	Specifies the electron affinity of the material	(eV)
permittivity	Specifies relative dielectric permittivity of a material	
MUN	Specifies the electron mobility	(cm^2/Vs)
MUP	Specifies the hole mobility	(cm^2/Vs)
TAUN0	Specifies the electron recombination lifetimes	(s)

TAUP0	Specifies the hole recombination lifetimes	(s)
Augn	Specifies the auger coefficient for electrons	(cm^6/s)
Augp	Specifies the auger coefficient for holes	(cm^6/s)
COPT	Specifies the radiative recombination rate coefficient	(cm^3/s)

Among the specific examples used in this thesis is:

```
material material= CdTe EG300=1.5 NC300=8e17 NV300=1.8e19 MUN=320 MUP=40
AFFINITY=4.28 Permittivity=9.4 taun0=1e-9 taup0=1e-9 COPT=4.72e-11
```

```
material material= CdTe index.file=CdTe.nk
```

In the first example, we specify the bandgap, the conduction and valence band density of state, electron and hole mobility, the electron affinity, permittivity, electron and hole lifetimes, and the radiative recombination rate coefficient of the CdTe material. In the second one, we specify the refractive and extinction indices of the material of CdTe which is in a .txt file whose name is CdTe.nk.

- **In case utilize unknown or undefined materials in Atlas device**

As indicated earlier, all materials in Atlas are classified as a semiconductor, an insulator, or a conductor. These classes are termed `user.group`. In order to correctly define a new material in Atlas, it must be determined [14]:

- The name of the new material (not known by Atlas) that was previously specified in the `REGION` statement using the `user.material` parameter.
- The `user.group` it belongs to.
- The known Atlas material is taken as a default material using the `user.default` parameter.

The general format is through the following statements:

```
material material= <name of the new material> user.group=<semiconductor
or conductor or insulator> user.default=<default material> EG300=<>
NC300=<> NV300=<> MUN=<> MUP=<> AFFINITY=<> Permittivity=<> taun0=<>
taup0=<> index.file=<>
```

b) Models

Physical models in semiconductors have been modeled as mathematical expressions that describe the physics of semiconductor devices. These models need to be robust, accurate, and computationally efficient. Except for impact ionization models, which are specified using `IMPACT` statements, physical models are specified using the `MODELS` statement. Atlas provides a comprehensive set of physical models, which are classified into five categories [14]:

- Mobility of Charge Carriers
- Generation-Recombination mechanisms
- Transport statistics
- Impact ionization
- Tunneling

The syntax of the model statement is as follows:

```
MODELS <model flag><general parameter> <model dependent parameters>
```

The choice of model depends on the materials chosen for the simulation. The example below shows some models:

```
models srh conmob fermi print
```

`srh`: activates Schokcley-Read-Hall recombination.

`fermi`: activates Fermi-Dirac statistics

`conmob`: is the concentration dependent model.

`print`: lists to the run time output the models and parameters, which will be used during the simulation. This allows the verification of models and material parameters.

c) Contact

Contact determines the attributes of the electrode. An electrode in contact with semiconductor material is assumed by default to be ohmic. If a work function is defined, the electrode is treated as a Schottky contact. The `contact` statement is used to specify the metal workfunction of one or more electrodes. The `name` parameter is used to identify which electrode will have its properties modified. The `WORKFUNCTION` parameter sets the workfunction of the electrode [14].

On other hand, the `contact` statement is used to determine surface recombination. The general syntax for contact is as follows:

```
contact name=<>
```

The following are examples of contact statement:

```
contact name=anode  WORKFUNCTION=5.1

contact name=anode  SURF.REC VSURFN=1e7 VSURFP=1e7
```

d) Interface

Indicates `interface` statement at interfaces between semiconductors and insulators. It is used to define the interface charge density and surface recombination velocity. Also, to define other parameters at the interface between other material such thermionic current between semiconductor-semiconductor. The interface statement can be written as:

```
interface <localization> <parameter>
```

The following example defines interface with surface recombination velocity Sn and Sp for electrons and holes respectively:

```
interface y.min=-1 y.max=-1 x.min=0 x.max=1 s.n=1e-9 s.p=1e-9
```

e) Light Beam

In cases where lighting is important to a device such as solar cells, Atlas provides the ability to use a number of light sources and adjust their location, orientation, and intensity. An optical beam is modeled as a collimated source using the `BEAM` statement of the form:

```
BEAM <parameters>
```

The origin of the beam is defined by parameters `X.ORIGIN` and `Y.ORIGIN`, the `ANGLE` parameter specifies the direction of propagation of the beam relative to the x -axis, while ANGLE = 90 describes a vertical illumination from the top of the device. The following example represents the "`BEAM`" command used for our simulation.

```
BEAM  NUM=  1  AM1.5  x.origin=0.5  y.origin=-5  WAVEL.START=0.1
WAVEL.END=1 WAVEL.NUM=50 ANGLE=90.0
```

3.3.3.2.3 Numerical method selection

After specifying models used in the simulation for a device, the next step should be to define a way of solving these different combinations of models. Atlas provides three types of solution techniques:

- decoupled (GUMMEL)
- fully coupled (NEWTON)
- BLOCK.

The `GUMMEL` method will solve for each unknown in turn keeping the other variables constant, repeating the process until a stable solution is achieved. The `NEWTON` method solves the total system of unknowns together. The `BLOCK` methods will solve some equations fully coupled while others are de-coupled [14].

Generally, the `GUMMEL` method is useful where the system of equations is weakly coupled but has only linear convergence. The `NEWTON` method is useful when the system of equations is strongly coupled and has quadratic convergence. However, the NEWTON method may spend extra time solving for quantities which are essentially constant or weakly coupled. `NEWTON` also requires a more accurate initial guess of the problem to obtain convergence. Thus, a `BLOCK` method can provide for faster simulations times in these cases over `NEWTON`. `GUMMEL` can often provide better initial guesses to problems. It can be useful to start a solution with a few `GUMMEL` iterations to generate a better guess. Then, switch to `NEWTON` to complete the solution [14]. The following example shows the use of the method statement.

```
METHOD NEWTON
```

3.3.3.2.4 Solution specification

Once the appropriate numerical method is chosen, the simulation is ready to be taken to the next step (the solution). This part of the input deck to Atlas is where the simulation does its calculations to solve for the device specified. It is broken down into four main statements: `LOG,` `SOLVE,` `LOAD`, and `SAVE`.

a) Log

The `LOG` statement creates a storage file where all results of a run will be saved; Any AC, transient, or DC data generated by `SOLVE` statements after the `LOG` statement will be saved [14].

Statement syntax:

```
LOG OUTFILE=<NAME.LOG>
```

The following shows an example of the LOG statement.

```
LOG OUTFILE=CdTe_SolarCell_outputfile.LOG
```

The example saves the current-voltage information into CdTe_SolarCell_outputfile.LOG.

b) Solve

The `SOLVE` statement calculates the solution at one or more bias points for A.C. or D.C. First, a simplified initial solution must be done (which solves only Poisson's equation) to get an initial guess for the final solution. We can use the syntax as follows:

```
SOLVE INIT
SOLVE VANODE=-0.1 NAME=ANODE VSTEP=0.025 VFINAL=1.1
```

In this example, we use the solve statement for a D.C analysis that ramps the Anode voltage from (-0.1 V) to (1.1 V) with (0.025 V) steps.

For an A.C as follows:

```
SOLVE VANODE=-0.1 NAME=ANODE VSTEP=0.025 VFINAL=1 AC FREQ=1E2
```

where `FREQ` is the frequency, which in this example equals 200 (Hz).

c) Load

The `LOAD` statement is used to load previous solution files as initial guesses to other bias points whenever required to assist in the solution. This statement requires that one of the following file parameter syntaxes be used [14].

```
LOAD INFILE=<filename>
```

or

```
LOAD IN1FILE=<filename> IN2FILE=<filename>
```

d) Save

The `SAVE` statement saves all node point information into an output file for visualization or for future use as an initial guess. Atlas provides the possibility of saving these data into a structure file (`.str`) using the `SAVE` statement. An example of the `SAVE` statement which stores the data into a file named (CdTe_SolarCell_outputfile) is:

```
save outf= CdTe_SolarCell_outputfile.str
```

3.3.3.2.5 Results analysis

a) Extract

The final section of the input deck is extracting the data, and the extract command is used to extract specific parameter values from the log file or the solution file. `EXTRACT` operates on the previous solved curve or structure file. It has a flexible syntax that allows the user to extract device parameters and construct specific EXTRACT routines. `EXTRACT` statements utilize the currently open log file by default. To override this default, supply the name of a file to be used by `EXTRACT` before the extraction routine. The declaration of this command is as follows:

```
EXTRACT INIT INF = <file name>
```

The following example shows how to calculate the photovoltaic characteristics (J_{sc}, V_{oc}, FF, and η) of a solar cell.

```
extract init infile="solar_cell.log"
extract name="IV" curve(v."anode", i."cathode")outf="IV_CdTe_
SolarCell.log"
extract name="Isc" y.val from
curve(v."anode",i."cathode")where x.val=0.0
extract name="JscmAcm2" $Isc*1e03/$"area"
extract name="Voc" x.val from curve(v."anode",i."cathode")
where y.val=0.0
extract name="Pm"max(curve(v."anode",(v."anode"*i."cathode")))
extract name="FF" ($"Pm"/($"Isc"*$"Voc"))*100
extract name="Opt_int" max(beam."1")
extract name="Eff" ($Pm/($"Opt_int"*$"area"))*100
```

b) Tonyplot

Besides extracting the data, it can be displayed graphically by the `TonyPlot` statement. TonyPlot is a graphical post-processing tool for use with all Silvaco simulators. All graphics in Atlas is performed by saving a file and loading the file into TonyPlot. Can plot a file or many files with tonyplot the statement are respectively:

```
TONYPLOT file name1.LOG
TONYPLOT - OVERLAY file name1.LOG file name2.LOG
```

In the example below, the `EXTRACT` statement obtains the current and voltage characteristics of a CdTe solar cell. This information is saved into the IVcurve.dat file. Then, `TonyPlot` plots the information in the "IV_CdTe_SolarCell.dat" file. Figure 3.11 shows the result of a curve obtained by the `TonyPlot` statement.

```
Extract name="IV" curve(v."anode", i."cathode") outf= "IV_
CdTe_SolarCell.log"

Tonyplot IV_CdTe_SolarCell.log
```

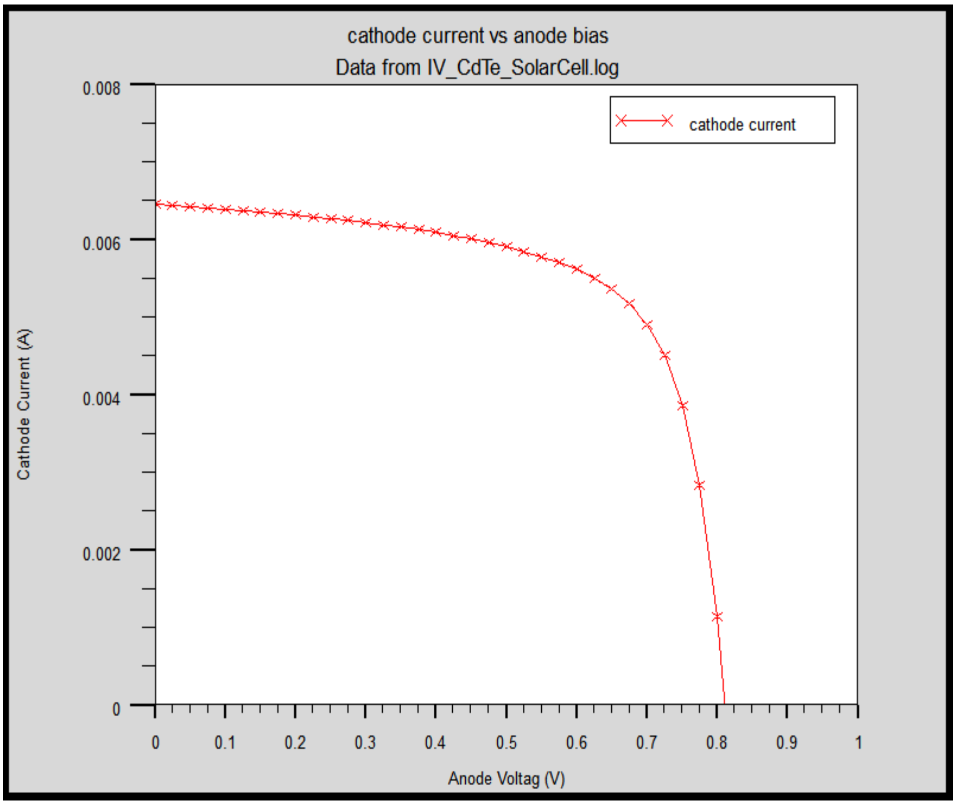

Figure 3. 11: TonyPlot IV curve.

3.4 Conclusion

In this chapter, we studied the fundamental equations in semiconductors to simulate a solar cell. Thus providing a basic understanding of the physical principles that underlie the operation of solar cells. The second part was devoted to explaining various SILVACO tools, particularly the ATLAS tool by introducing the principal operations and the main panels which can help us to understand and use this simulator. We focused especially on solar cells simulation and their various commands (instructions), beginning from defining the structure to extracting the solar cell's photovoltaic properties (J_{sc}, V_{oc}, FF, and η).

CHAPTER 4: Numerical simulation results and interpretation

4.1 Introduction

After having reviewed the essential axes for the study of PV cell devices, we will be able to proceed in this chapter with the simulation and optimization of a thin-film solar cell based on heterojunction CdS/CdTe in order to design a structure having the optimal electrical efficiency and deduce their optimal photovoltaic parameters such as the short-circuit current density (Jsc), the open-circuit voltage (V_{oc}), the fill factor (*FF*), and the conversion efficiency (η) and highlighting the input parameters that have the greatest impact on this performance.

In this work, CdTe solar cell has been investigated employing 2-dimensional numerical simulations using TCAD Silvaco-Atlas simulator. Initially, a reference structure of FTO/i-SnO_2/CdS/CdTe solar cell was simulated based on experimental data for the validity of the simulation and the extent to which present results agree to the experimental data. To reduce the minority carrier recombination loss, a new structure is proposed by incorporation of the cuprous oxide (p-type Cu_2O) layer at back-contact as a hole transport-electron blocking layer (HT-EBL), with optimization of the cell parameters in terms of thickness, doping concentration, and carrier lifetime. In the third part, we also investigated and compared between the SnO_2 and ZnO as an HRT layer for different thicknesses. Finally, the influences of temperature on the optimized CdTe solar cell performance are reviewed.

4.2 Description of the conventional structure of CdS/CdTe solar cell

At the beginning of this study, we simulate the reference cell [103], whose schematic structure is shown in Figure 4.1. The reference cell grown in superstrate configuration consists of the n-CdS/p-CdTe heterojunction with a doping concentration of 1×10^{18} cm^{-3} and 2×10^{14} cm^{-3}, respectively. Fluorine-doped tin oxide (FTO) layer is used as TCO to form the front-contact and an n-type doping concentration of 3×10^{20} cm^{-3}. Undoped SnO_2 is used as an HRT layer placed between front-contact TCO layer and CdS window layer. In addition, 5 nm/50 nm of (Cu/Au) are used to form the back contact. More information about the structure manufacturing was reported in Ref. [103].

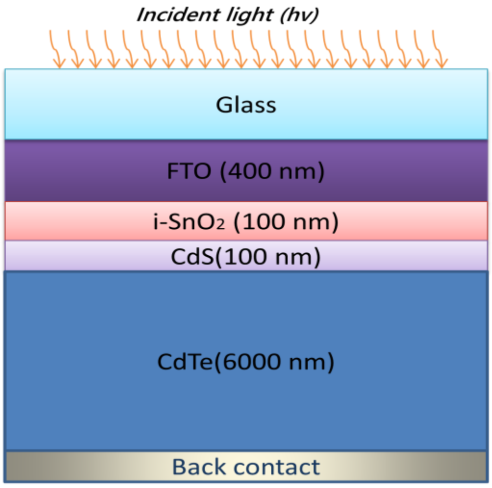

Figure 4.1: Schematic conventional structure of the CdTe solar cell.

4.3 Physical models

In this study, we used Silvaco-Atlas to design and optimize the CdTe solar cell structure. The calculation depends on several models, which in turn are based on different mathematical equations. As an example, the Poisson equation (3.2) and the continuity equations (3.5), (3.4) determine how electrons and holes densities develop as a consequence of transport (3.8), (3.9). They also determine the generation and recombination processes in the solar cell.

The generation introduced in the continuity equations (3.3) and (3.4) is due to external factors. In our case, the external factor is light, so we have an optical generation. Under the effect of light, charge carriers can be generated in the semiconductor where when photons with sufficient energy impinge onto a semiconductor, those photons may excite valence electrons up to the conduction band thus photo-generating an electron hole pair. This is the basis on which a solar cell operates upon the photo-generation rate is modeled in ATLAS as [14]:

$$G = \eta_0 \frac{P\lambda}{hc} \alpha e^{-\alpha y} \tag{4.1}$$

where η_0 is the internal quantum efficiency, which represents the number of carrier pairs generated per photon observed, P is a coefficient that tracks the cumulative effects of transmission, reflection, and loss throughout the device. λ is the optical wavelength, y is the relative distance for the ray in question, and α is the absorption coefficient given as follows [14]:

$$\alpha = \frac{4\pi}{\lambda} k \tag{4.2}$$

where k is the extinction coefficient (the imaginary part of the optical index of refraction).

ATLAS solves this photogeneration model at each node in a semiconductor material, where it is automatically invoked whenever a light source is included. The value for (4.1) determined at each node is then used as an input for the carrier continuity equations.

In order to model the losses in the structure, we take into account the Shockley- Read-Hall (SRH) recombination; they are modeled by the standard expression (SRH) [14]:

$$R_{SRH} = \frac{pn - n_i^2}{\tau_n\left[p + n_{ie}\exp\left(\frac{-E_{TRAP}}{KT}\right)\right] + \tau_p\left[n + n_{ie}\exp\left(\frac{E_{TRAP}}{KT}\right)\right]} \tag{4.3}$$

where E_{TRAP} is the difference between the trap energy level and the intrinsic Fermi level ($E_{TRAP} = E_T - E_i$) , which is assumed $E_{TRAP} = 0$, i.e. a single trap level corresponding to the most efficient recombination center. τ_n, and τ_p are the carrier lifetime for electrons and holes, respectively. The values of these two parameters for the materials used are in Table 4.1

We also utilized the phenomena of (direct) radiative recombinations, which is very frequent in direct-gap semiconductors, and it was modeled by the standard relation:

$$U_r = B_r\left(np - n_i^2\right) \tag{4.4}$$

where B_r is the radiative recombination coefficient assumed equal to 4.72×10^{-11} cm^3/s [153].

In addition to the recombination of the defects present on the front and back sides of the cell, they are modeled by the inclusion of surface recombination velocities of the electrons S_n and holes S_p chosen as being equal to 10^7 cm/s [143,154–156].

The band gap varies with temperature and experimental results show that the energy bands of most semiconductors decrease with increasing temperature [43,54]. The band gap variation with temperature is modeled in Atlas by a universal function (Varshni's law) [14,157]:

$$E_g(T) = E_g(0) - \left(\frac{\alpha T^2}{T+\beta}\right) = E_g(300) + \alpha\left[\frac{300^2}{300+\beta} - \frac{T^2}{T+\beta}\right] \tag{4.5}$$

Where, T is the temperature, $E_g(300)$ is the bandgap at 300 K, α and β are constants material parameters. In our case, the Eg(300) value for each material that is used in the simulations is in Table 4.1. As for the fitting parameters (for CdTe $\alpha = 4.6\times 10^{-4}$ eV K^{-1}, β=160.1 K [63]), (for CdS $\alpha = 3.86 \times 10^{-4}$ eV K^{-1}, β=103 K [63]) and (for SnO_2 $\alpha = 3.1\times 10^{-4}$ eV K^{-1}, β=530 K [158]).

4.4 Simulation parameters

The fundamental simulation parameters used as entry data in this study are summarized in Table 4.1. These values are consistent with recent literature on CdS/CdTe solar cells [51,62,103,143,159].

Table 4.1: Device parameters used in the simulation.

Parameter	Layers			
	FTO	i-SnO_2	CdS	CdTe
Thickness, t_m (nm)	400	100	100	6000
Bandgap, E_g (eV)	3.6	3.6	2.42	1.5
Electron affinity, χ_e (eV)	4.5	4.5	4.3	4.28
Dielectric ratio, E_{ps}	9	9	10	9.4
Electron mobility, μ_n (cm^2 /V s)	100	100	100	320
Hole mobility, μ_p (cm^2 /V s)	25	25	25	40
Valence band effective density of states, N_v(cm^{-3})	1.8×10^{19}	1.8×10^{19}	1.8×10^{19}	1.8×10^{19}
Conduction band effective density of states , N_c (cm^{-3})	2.2×10^{18}	2.2×10^{18}	2.2×10^{18}	8×10^{17}
Carrier concentration, N_d (cm^{-3})	3×10^{20}	-	1×10^{18}	-
Carrier concentration, N_a (cm^{-3})	-	-	-	2×10^{14}
Hole Lifetime (ns)	0.1	0.1	0.01	1
Electron Lifetime (ns)	100	100	0.01	1

For a given light source, the available photocurrent through the cell depends on the optical properties of the different materials. The optical properties of a material cover the properties due to the interaction of the material with light. They mainly include the refractive index and absorption coefficient. These properties are essential for optoelectronic components since they govern the movement of light in the component. For example, in a device composed of different materials, light tends to propagate into the materials with the highest refractive index.

The refractive index of a solar cell describes the propagation and absorption of light through the material. The refractive index is a complex value given by [12,50]:

$$\tilde{n} = n + ik \tag{4.6}$$

where n denotes the real part and the k is the imaginary part of the refractive index, and they are also referred to as the refractive index and extinction coefficient of the complex refractive index, respectively. The real part quantifies the phase velocity of light, whereas the imaginary part quantifies the absorption of light in the material. The following equation is used to calculate the refractive index of a semiconductor material [52,88]:

$$n = \left(\frac{1+R}{1-R}\right) + \sqrt{\frac{4R}{(1-R)^2} - k^2} \tag{4.7}$$

Where

$$k = \frac{\alpha\lambda}{4\pi} \tag{4.8}$$

and R denotes the reflectance, which is related to transmittance (T), absorption coefficients (α), and the thickness (d) of the thin films, as given by the following equation [86]:

$$T = (1-R)^2 \exp[-\alpha d] \tag{4.9}$$

In particular, the wavelength-dependent refractive index (n) and extinction coefficient (k) of the CdS and CdTe layers have been assumed according to [49]. At the same time, for SnO_2, these parameters were obtained from Ref. [160], Figure 4.2 and 4.3 shows the optical constants used for the different layers of the simulated cells. For the metal contact materials, optical constants available in the SOPRA database of the Silvaco–Atlas simulator were used in the simulation.

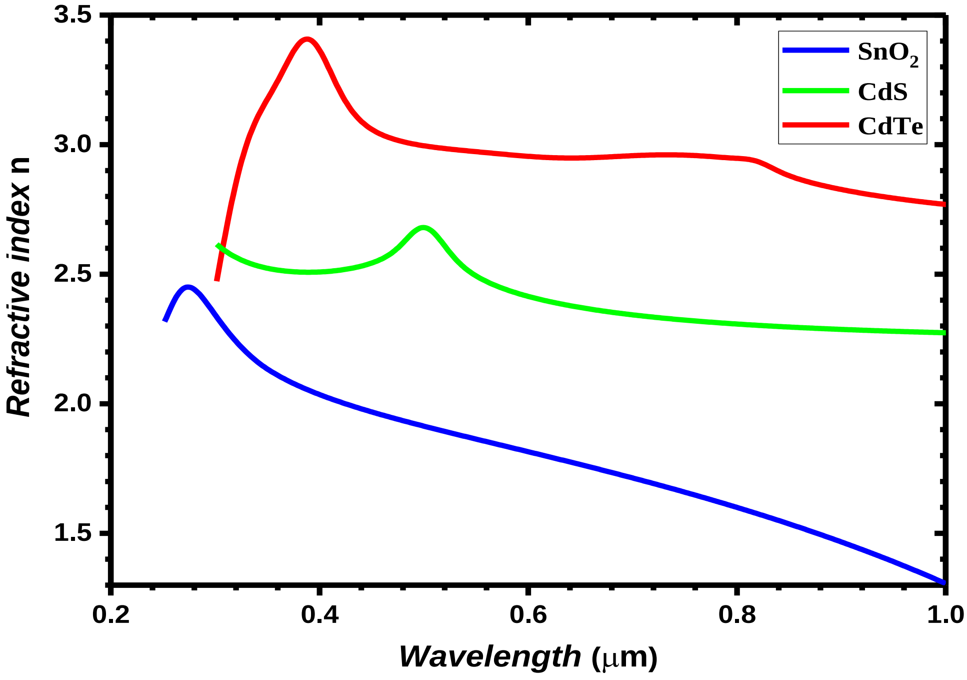

Figure 4.2: Refractive index used for the different layers of the simulated cells.

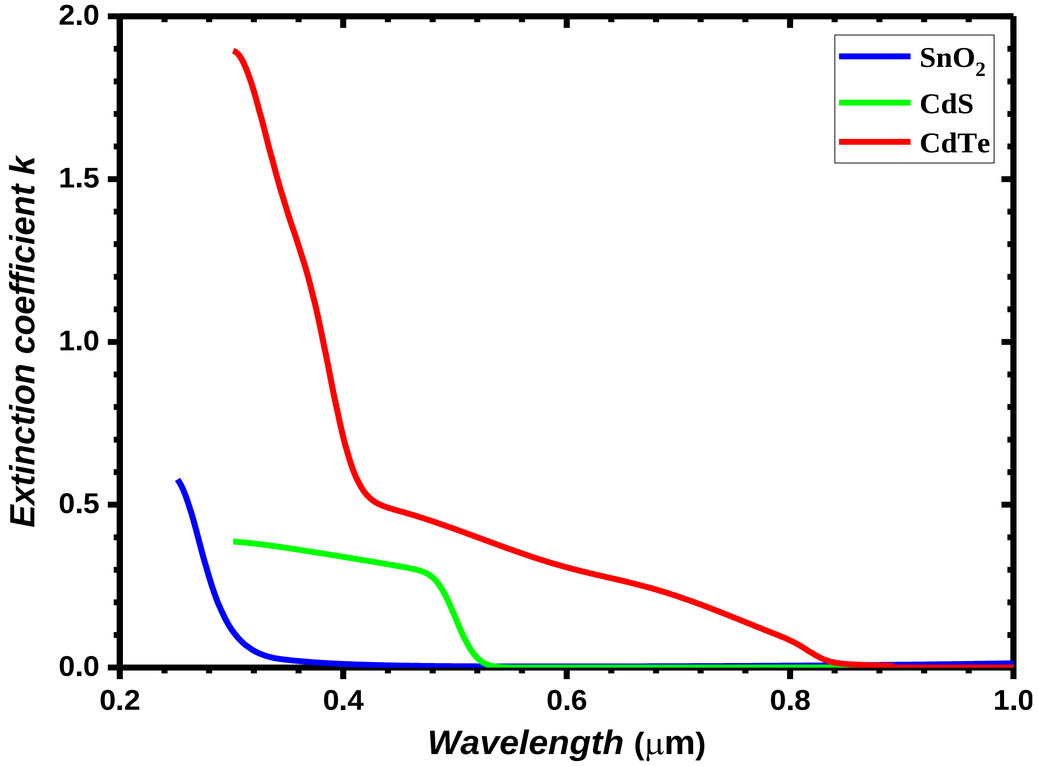

Figure 4.3: Extinction coefficient used for the different layers of the simulated cells.

4.5 Comparison and validation of simulated cell with an experimental cell

During the simulations, an area of 0.25 cm^2 was selected for this device. The simulation was performed under air mass 1.5 global spectrum (AM1.5G) with an incident irradiance of 1000 W/m^2 and at an operating temperature of 300 K. Figure 4.4 exhibits the energy band diagram of the reference cell obtained by simulation.

Firstly, to validate the assumed simulation models and parameters, Figure 4.5 shows the curves of current density-voltage *(J-V)* characteristics of the simulated structure and the experimental cell reported in Ref. [103]. A good proportion is noticed for both *J-V* curves. It means that reasonable input parameters have been used in the calculation.

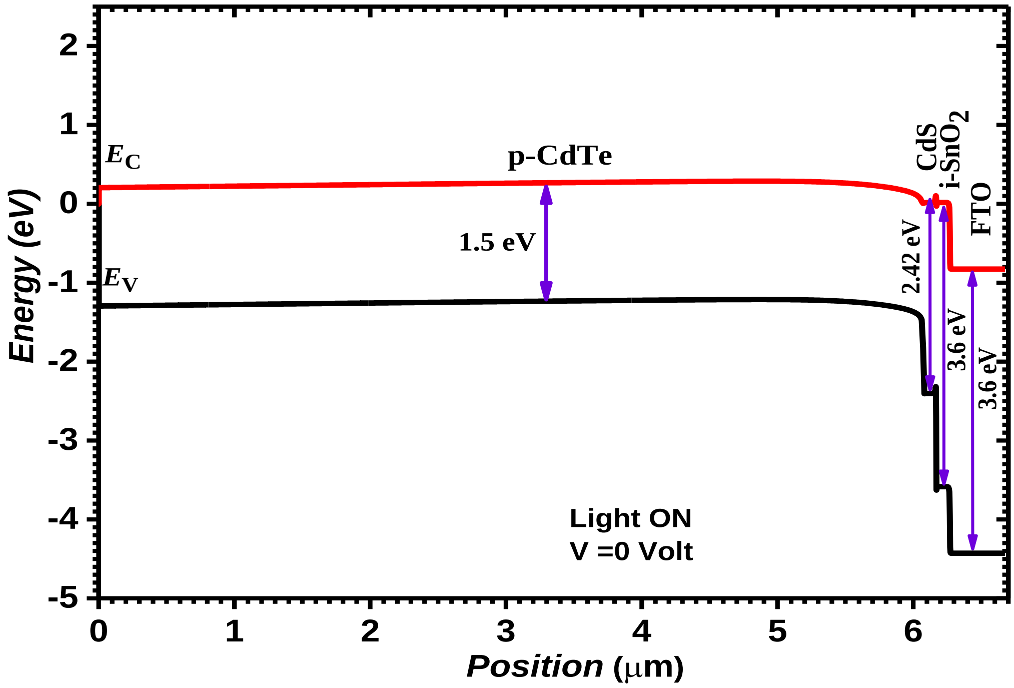

Figure 4.4: Energy band structure of the CdTe solar cell.

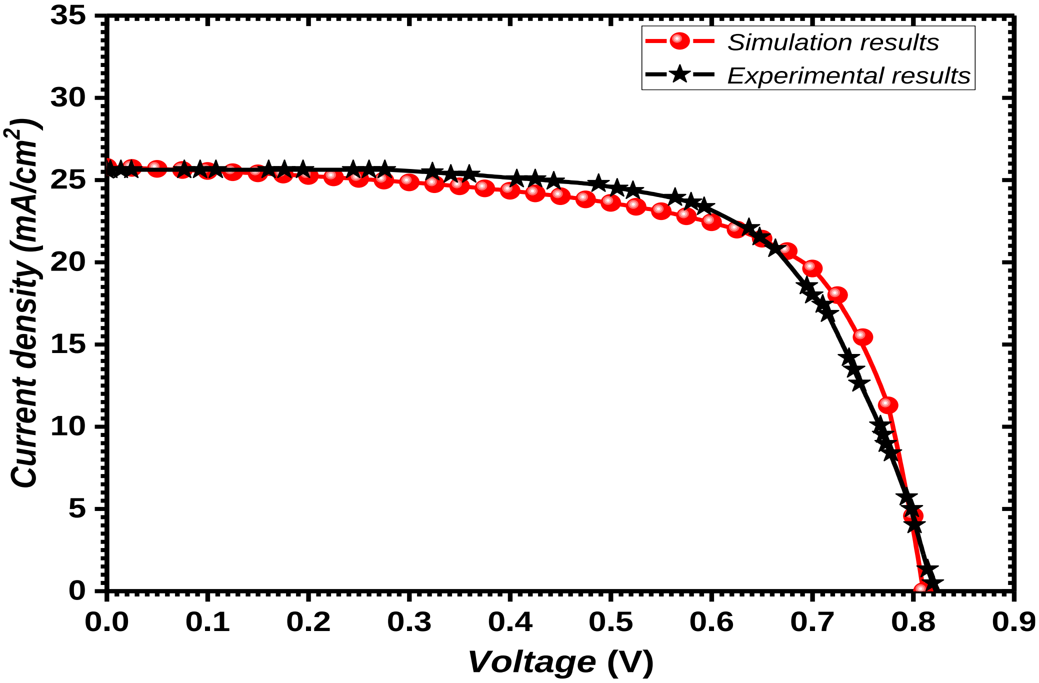

Figure 4.5: Current density-Voltage characteristics for both reference and experimental cells of CdTe solar cell.

Table 4.2 reveals the characteristics of the solar cell extracted from Figure 4.5, namely the short-circuit current density (J_{sc}), the open-circuit voltage (V_{oc}), the fill factor (FF), and the conversion efficiency (η). A good agreement between the simulation and experimental results demonstrates that the parameters and the models used in the simulation process are correct.

Table 4.2: Photovoltaic parameters obtained by simulation and experimental of CdTe solar cell.

Cell performances	J_{sc} (mA/cm^2)	V_{oc}(V)	FF (%)	η (%)
Simulation	25.79	0.81	66.76	13.96
Experiment [103]	25.6	0.82	66.4	14

4.6 Optimization of CdTe solar cell with incorporation of Cu_2O HT-EBL layer

To optimize the device parameters for efficient CdTe solar cell using a Cu_2O thin layer, we focus on the fundamental parameters, such as: thickness, carrier and doping concentrations. In this section, Cu_2O HT-EBL thin layer was incorporated between the absorber layer and the back-contact to improve the carrier recombination and thus the cell performance. Figure 4.6 illustrates the schematic structure of the proposed CdS/CdTe/Cu_2O solar cell structure. The parameters of Cu_2O material are listed in Table 4.3, and the optical properties are taken from Ref. [91].

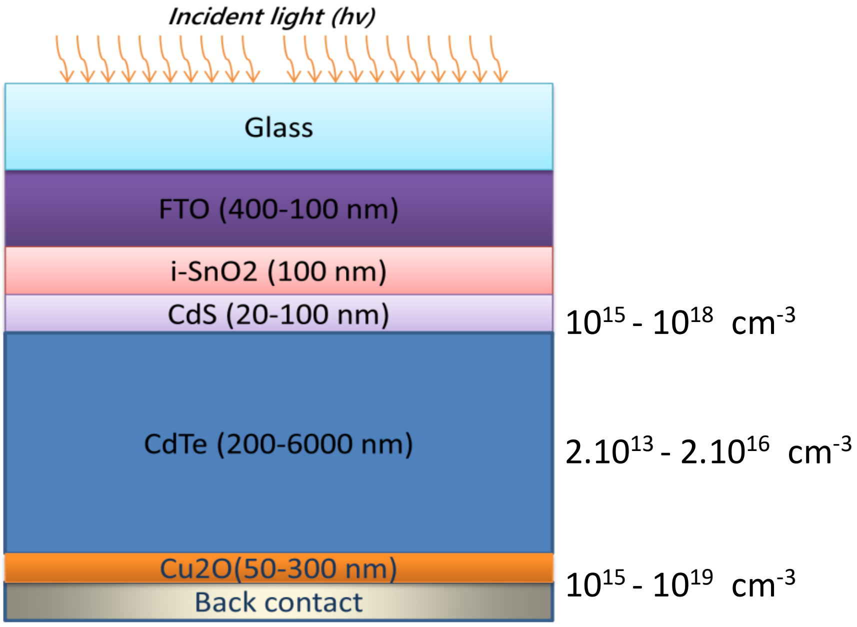

Figure 4.6: Schematic structure of the proposed solar cell.

Table 4.3: Physical parameters of Cu_2O layer used as an HT-EBL in the cell structure [90,99,161].

Parameter	Layers
	Cu_2O
Thickness, t_m (nm)	50
Bandgap, E_g (eV)	2.2
Electron affinity, χ_e (eV)	3.3
Dielectric ratio, E_{ps}	9
Electron mobility, μ_n (cm^2 /V s)	200
Hole mobility, μ_p (cm^2 /V s)	25
Valence band effective density of states, N_V(cm^{-3})	2.4×10^{19}
Conduction band effective density of states, N_c (cm^{-3})	1.8×10^{18}
Carrier concentration, N_A (cm^{-3})	1×10^{18}
Hole Lifetime (ns)	100
Electron Lifetime (ns)	100
Varshni coefficient α (eV K^{-1})	4.8×10^{-4}
Varshni coefficient β (K)	275

4.6.1 Influence of doping concentration and thickness of CdTe absorber layer

Figure 4.7 shows the efficiency curve as a function of the doping concentration of CdTe absorber layer, N_A(CdTe), from 2×10^{13} to 2×10^{16} cm^{-3}. It can be seen clearly that the conversion efficiency increases rapidly with increasing N_A(CdTe) until it reaches a saturation at N_A(CdTe) = 2×10^{16} cm^{-3} with a maximum efficiency of 16.53%. The saturation occurs at the CdS/CdTe interface as the space charge region becomes tighter by increasing the doping concentration. This tightness affects the buildup electric field, which decreases the free charge carrier recombination inside the CdTe absorber bulk and thus increases the efficiency. In the rest of this study, we will use the optimal value of 2×10^{16} cm^{-3} as a doping concentration of CdTe absorber layer. This concentration is in consistent to many previous studies [117,138,162].

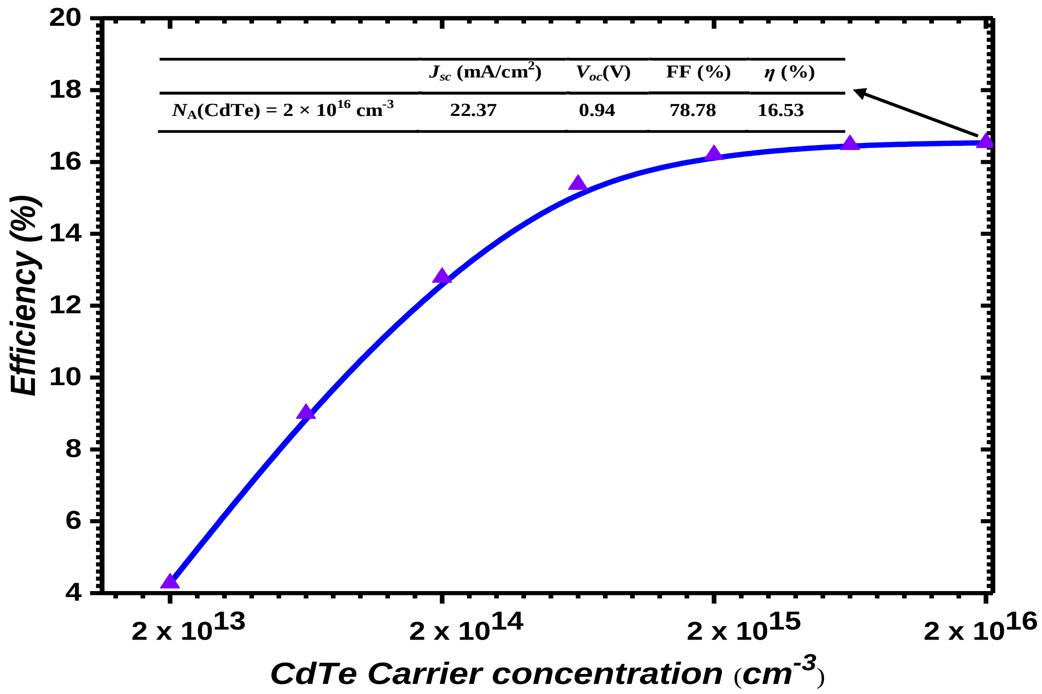

	J_{sc} (mA/cm^2)	V_{oc}(V)	FF (%)	η (%)
N_A(CdTe) = 2 × 10^{16} cm^{-3}	22.37	0.94	78.78	16.53

Figure 4.7: Cell efficiency as a function of the doping concentration of CdTe absorber layer.

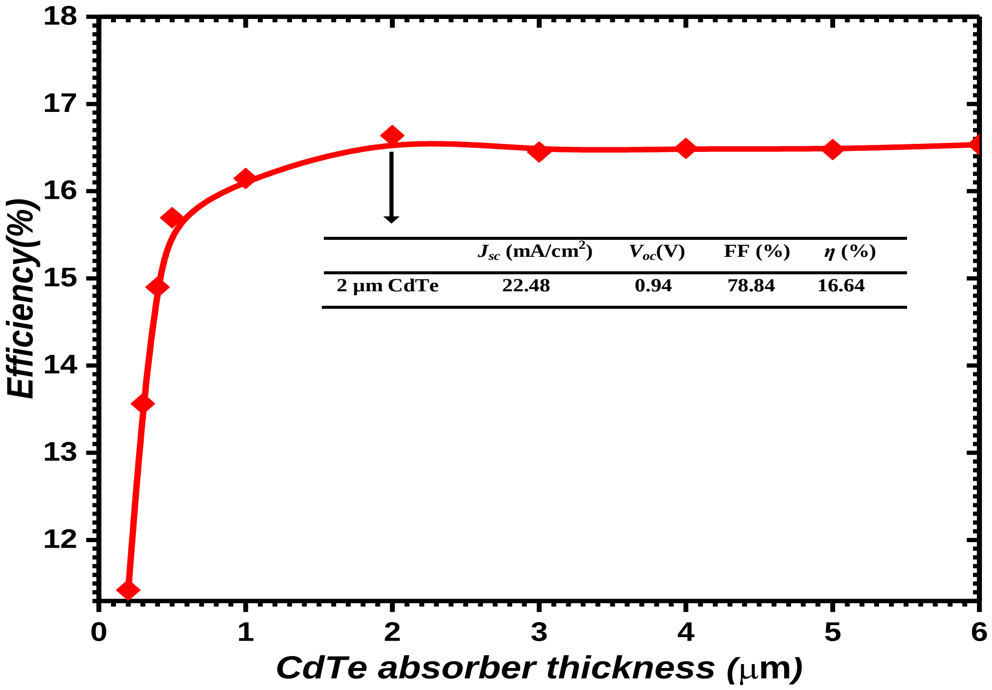

	J_{sc} (mA/cm^2)	V_{oc}(V)	FF (%)	η (%)
2 µm CdTe	22.48	0.94	78.84	16.64

Figure 4.8: Cell efficiency as a function of CdTe layer thickness.

After fixing N_A(CdTe) = 2 × 10^{16} cm^{-3}, the p-CdTe layer thickness has been varied from 20 nm to 6000 nm. The cell efficiency as a function of p-CdTe absorber layer thickness is shown in Figure 4.8. By increasing the thickness from 20 nm to 2000 nm, a rapid evolution is observed and then becomes stable from almost 2000 nm–6000 nm. With the increasing thickness, the absorption of the photons increases until reaches 2000 nm so that it could sufficiently absorb all the photons to get the highest efficiency of 16.64%. This value agrees well with the previous theoretical study [53] which reports that 2000 nm is enough to absorb 99% of photons [53]. Therefore, 2000 nm is used as an optimum thickness of CdTe absorber layer in the rest of this work. This value is in good agreement with the previously reported results [143,154].

4.6.2 Influence of doping concentration and thickness of CdS window layer on the cell performance

In this section, the impact of CdS window layer parameters on the cell efficiency has been investigated by varying the doping concentration and the thickness. Figure 4.9 presents the variation of the efficiency offset as a function doping concentration of window layer, N_D(CdS). A slight increase in efficiency with N_D(CdS) ranging from 1 × 10^{15} to 1 × 10^{16} cm^{-3} is noticed. The efficiency decreases rapidly from 18.07% to 16.78% when N_D(CdS) varying from 1 × 10^{16} to 5 × 10^{16} cm^{-3} and then it becomes almost constant at the value 5 × 10^{16} cm^{-3} and above. Hence, one can conclude that high doping concentration of CdS window layer negatively impacts on CdTe solar cell performance. Accordingly, the optimum donor concentration with conversion efficiency up to 18.07% is 1 × 10^{16} cm^{-3}.

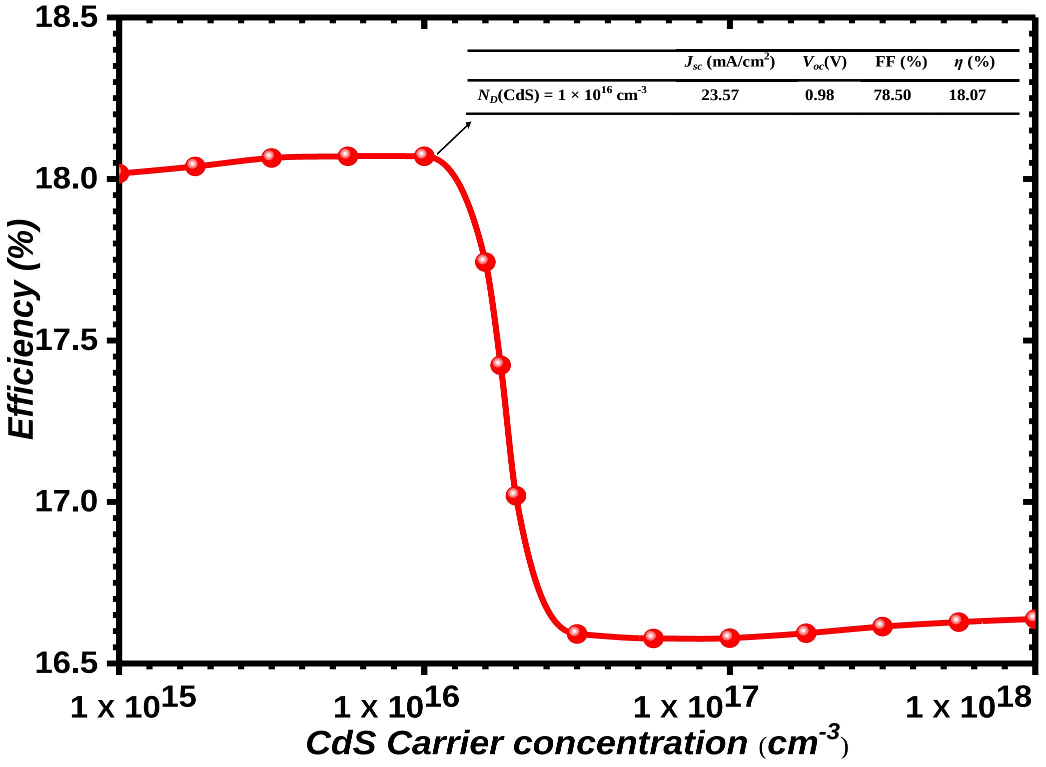

Figure 4.9: Cell efficiency as a function of the doping concentration of CdS window layer.

Figure 4.10 reveals the efficiency trend as a function of CdS window layer thickness, t(CdS), with N_D(CdS) = 1 ×10^{16} cm^{-3}. The efficiency increases firstly for t(CdS) lower than 40 nm and then decreases gradually when the thickness increases over 40 nm. A high efficiency of about 19.37% was obtained with t(CdS) = 40 nm. The decreasing efficiency at higher thickness may be due to decrease in photons reaching to the absorber layer. Nevertheless the photons missed by recombination process in the CdS/CdTe interface are increased. Therefore, it is desirable to use a small thickness of CdS window layer to augment the photocurrent [163] and the best thickness of CdS window layer is 40 nm. These results are in good agreement with the previous ones [156,164,165].

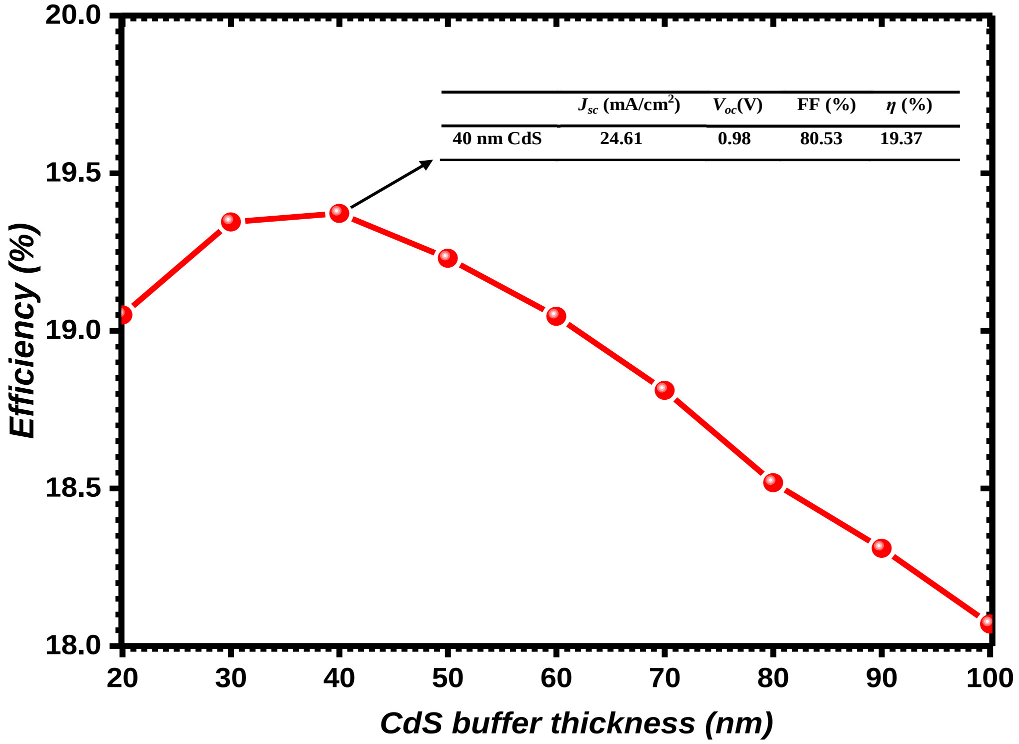

	J_{sc} (mA/cm^2)	V_{oc}(V)	FF (%)	η (%)
40 nm CdS	24.61	0.98	80.53	19.37

Figure 4.10: Cell efficiency as a function of the CdS layer thickness.

4.6.3 Effect of TCO layer thickness in the front side

The TCO front contact layer is the first part that is exposed to light in the cell structure. The TCO layer having band-gap of 3.3 eV is transparent to whole solar spectrum particularly for blue and ultraviolet regions. This increases the photoresponce of the layer as compare to the traditional semiconductors. The TCO layer not only helps in collecting the separated charge carriers but also acts as an antireflection coating. In this section, effect of the thickness of TCO layer on the cell efficiency, with a doping density equal to 3 × 10^{20} cm^{-3} is studied. The results of this investigation are shown in Figure 4.11. The figure reveals that the thickness of TCO layer doesn't substantially affect the cell efficiency. Therefore, a smaller thickness of TCO layer will be better to fabricate the device. The use of 100 nm is the best solution and this is in consistent to several published studies [166–168].

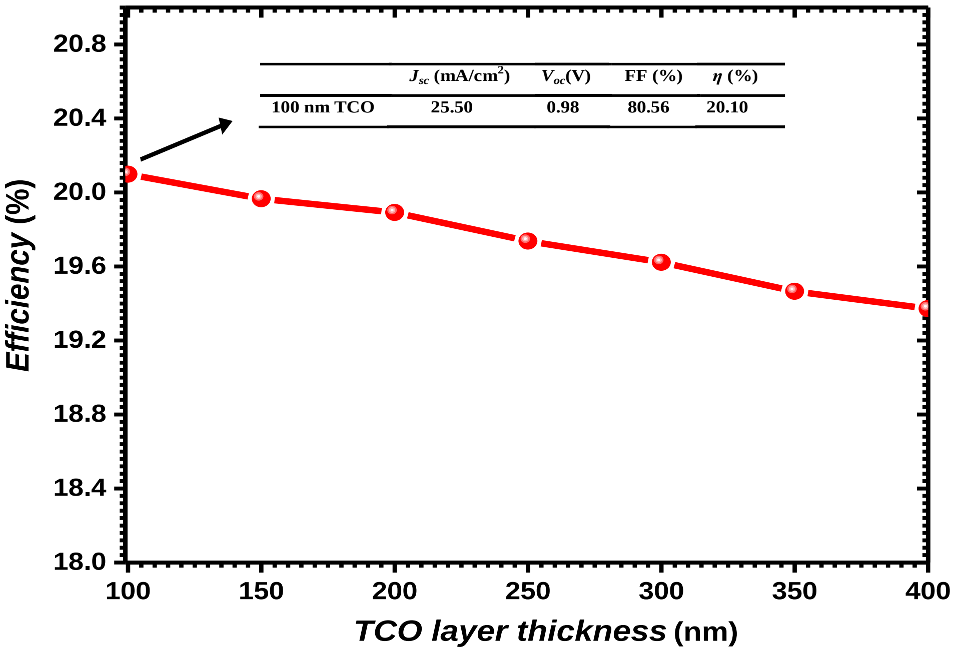

	J_{sc} (mA/cm^2)	V_{oc}(V)	FF (%)	η (%)
100 nm TCO	25.50	0.98	80.56	20.10

Figure 4.11: Cell efficiency as a function of the TCO layer thickness.

4.6.4 Effect of physical parameters of Cu_2O HT-EBL layer

Using the optimal parameters obtained in the previous sections for both CdS and CdTe layers, now we study the influence of Cu_2O HT-EBL layer on the solar cell performance. Figure 4.12 represents the conversion efficiency versus the doping concentration, $N_A(Cu_2O)$. From this curve, we notice an increase in efficiency up to 20% when $N_A(Cu_2O)$ increases above 1×10^{17} cm^{-3}. A good efficiency up to 20.1 % is achieved when the doping concentration reaches to 5×10^{18} cm^{-3}, therefore, this value will be used in the incoming sections. On the contrary, the efficiency is almost constant when the thickness of Cu_2O HT-EBL layer, $t(Cu_2O)$, increases (see Figure 4.13). Therefore, the thickness of 50 nm of Cu_2O HT-EBL layer is enough. This value agrees well with the experimental one [133]. Figure 4.14 demonstrates the energy-band diagram of the proposed cell, and it clearly shows a large band-gap of Cu_2O HT-EBL layer that acts as a barrier against the carriers passing.

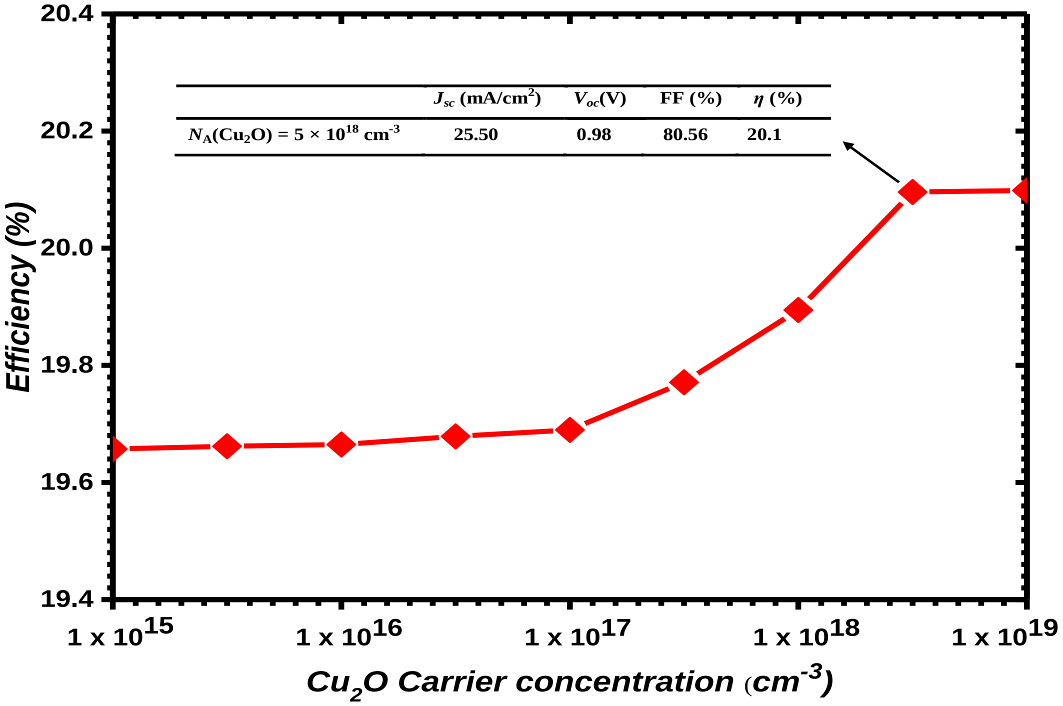

Figure 4.12: Cell efficiency as a function of the doping concentration of Cu_2O HT-EBL layer.

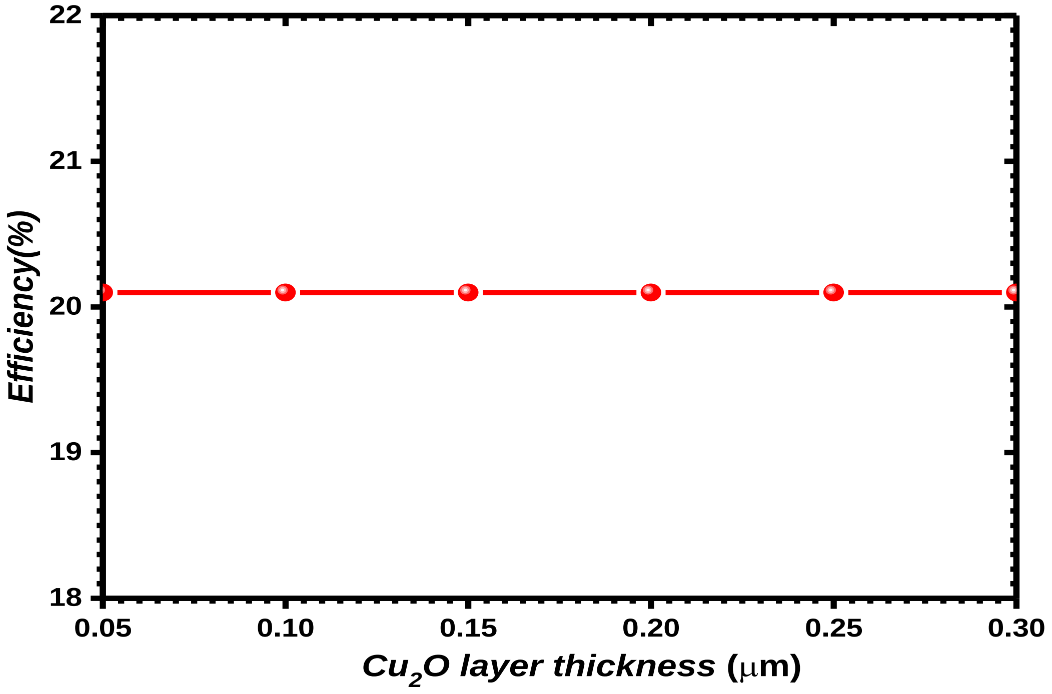

Figure 4.13: Cell efficiency as a function of Cu_2O layer thickness.

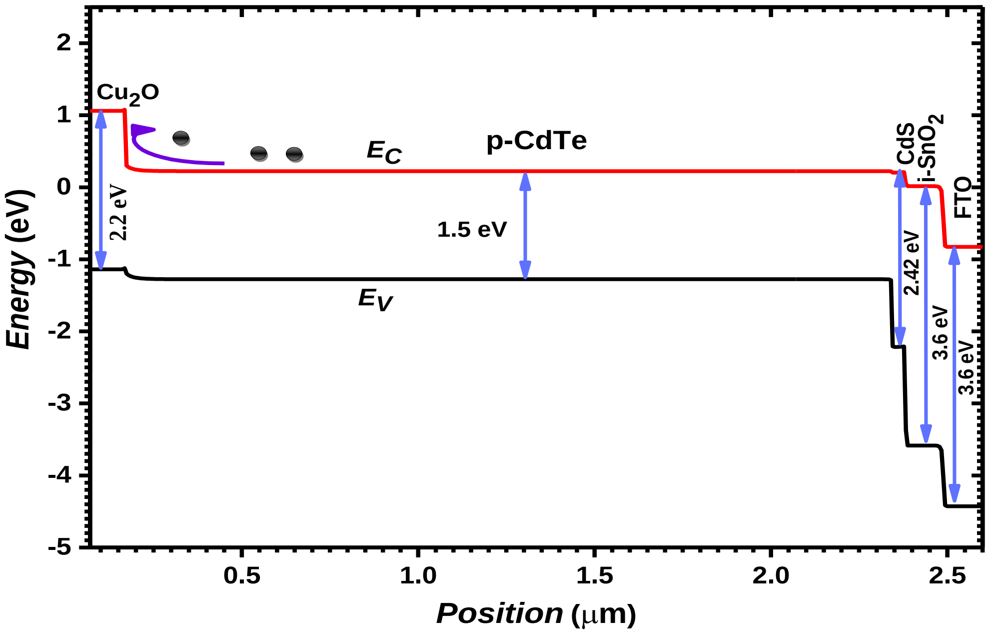

Figure 4.14: Energy-band structure of the proposed solar cell.

4.6.5 Influence of carrier lifetime of CdTe absorber layer on the cell performance

The carrier lifetime effect of CdTe absorber layer which is considered as one of the main parameters that affect the cell performance is investigated. The carrier lifetime is changed from 0.1 to 10 ns and the results are illustrated in Figure 4.15. As expected, the conversion efficiency increases from 14.6 to 24.35% with growing lifetime from 0.1 to 10 ns, showing a high impact of this parameter on device performance. An increase in the carrier lifetime results in step-up diffusion length of the carrier and thus raising the likelihood of the collecting of charge carriers in the back contact region. So, the desired value of carrier lifetime of CdTe layer is 10 ns, which agrees to the previous investigations [62,105].

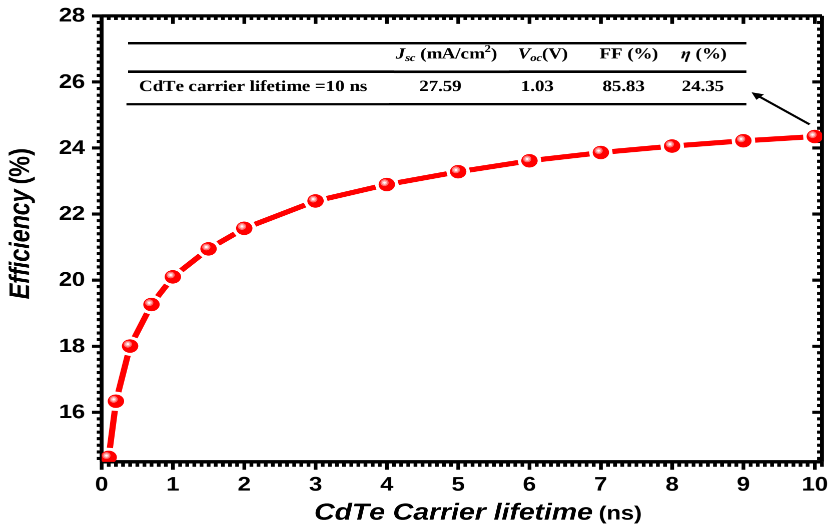

	J_{sc} (mA/cm^2)	V_{oc}(V)	FF (%)	η (%)
CdTe carrier lifetime =10 ns	27.59	1.03	85.83	24.35

Figure 4.15: Cell efficiency as a function of carrier lifetime of CdTe absorber layer.

4.7 Optimum design

Based on the obtained results, the optimal parameters are used in the model to extract the optimized structure. Figure 4.16 exhibits the optimal parameters of optimized structure which gives the maximum efficiency up to 24.35%. As a comparison, Figure 4.17 (a) and Figure 4.17 (b) represent the *J-V* and the *P–V* characteristics for both reference cell and optimized cell using Cu_2O HT-EBL layer. The photovoltaic parameters extracted from Figure V.17 (a) are summarized in Table 4.4. Experimentally, these modifications can be easily applied to the solar cell structures for more effective performance. It can help specialists in the field to improve CdTe thin-film solar cells and provide a clearer picture about it.

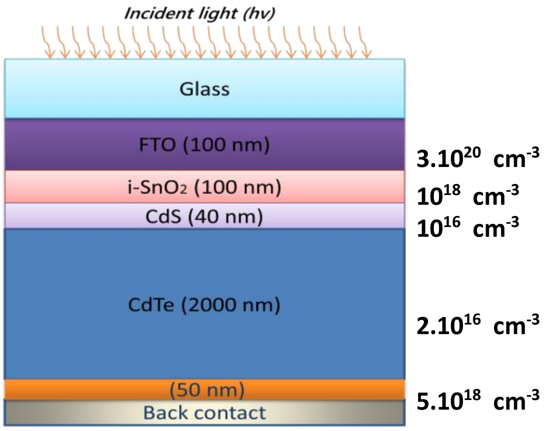

Figure 4.16: Schematic structure of the optimized solar cell structure.

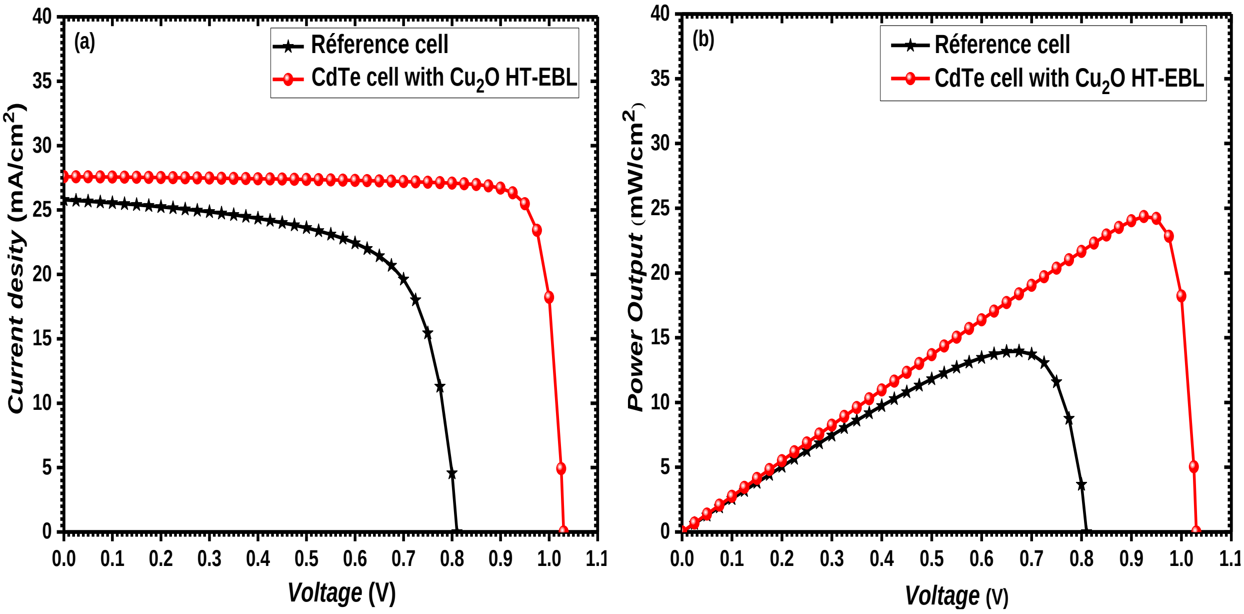

Figure 4.17: (a) Current density -Voltage characteristics of the reference and optimized cells, (b) Power-Voltage characteristics of the reference and optimized cells.

Table 4.4: Photovoltaic parameters extracted from the *J*-*V* curves for both the reference and the optimized cells.

Cell performances	J_{sc} (mA/cm^2)	V_{oc}(V)	FF (%)	η (%)
Reference cell	25.79	0.81	66.76	13.96
Optimal cell	27.59	1.03	85.83	24.35

4.7.1 Spectral response variation

It is very important to study how the optimized CdTe solar cell responds to the solar spectrum. So the external quantum efficiency (EQE) of the reference and proposed cells is calculated her. The EQE variation of the reference and optimized cells (according to the photovoltaic parameters listed in Table 4.4) are shown in Figure 4.18 along the wavelength ranging from 200 nm to 1000 nm. Expansion of the maximum absorption region of the optimized cell is located at 300–820 nm with an average EQE of 91%. In the reference cell, EQE is extending only from 500 to 820 nm with an average EQE of 85%. These results are also indication of excellent performance of proposed cell compared to the reference cell.

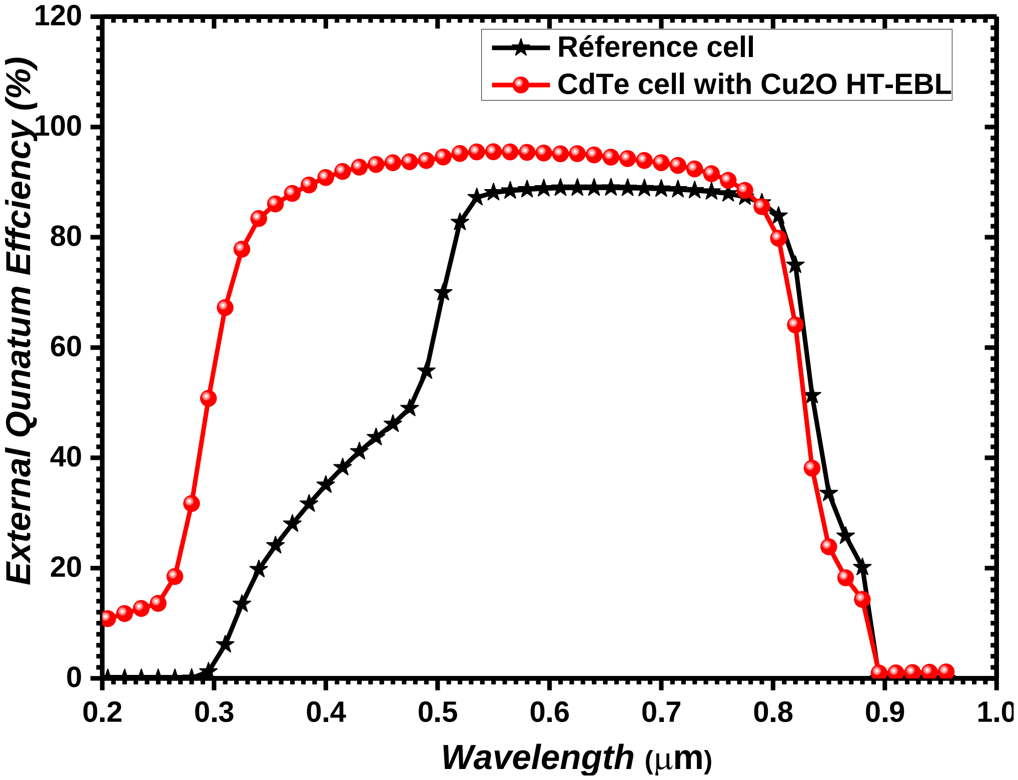

Figure 4.18: External Quantum Efficiency EQE behavior of the optimized structure.

4.8 Effect of high resistivity transparent (HRT) layer

Together with the presented analysis on the role of each layer on which the CdTe solar cell device is based, further investigations have been made considering different thicknesses of the SnO_2 region in the range of 20-120 nm, in addition to the use of ZnO as an alternative to SnO_2 and comparing them. Table 4.5 shows the simulation parameters utilized for ZnO as an HRT layer, and for the refractive index and extinction coefficient obtained from Ref. [169].

Table 4.5: Physical parameters of ZnO layer used as an HRT in the cell structure [74,77,78,165]

Parameter	Layers
	i-ZnO
Bandgap, E_g (eV)	3.3
Electron affinity, χ_e (eV)	4
Dielectric ratio, E_{ps}	9
Electron mobility, μ_n (cm^2 /V s)	100
Hole mobility, μ_p (cm^2 /V s)	25
Valence band effective density of states, N_v(cm^{-3})	2.2×10^{18}
Conduction band effective density of states, N_c (cm^{-3})	1.8×10^{19}
Carrier concentration, N_d (cm^{-3})	1×10^{17}
Hole Lifetime (ns)	0.1
Electron Lifetime (ns)	10

Figure 4.19 shows the efficiency of the solar cell with different HRT layer thicknesses. The simulations showed that this parameter has only a limited impact on the cell performance and the conversion efficiency has a variation in the limit of 0.2 %. This means that the performances of the solar cell device is unaffected by the HRT thickness variation from 20 nm to 120 nm and indicate that a very thin HRT layer is adequate for the purpose. This agrees with the previous results reported in Refs. [77,134]. On the other hand, the device based on SnO_2 showed the highest performance compared to ZnO. This difference may be due to the Bandgap and Electron affinity of SnO_2 being larger than that of ZnO, which makes the performance better. Therefore, SnO_2 can be a good choice as an HRT layer for CdS/CdTe solar cell device production, which is consistent with previous works [77,103].

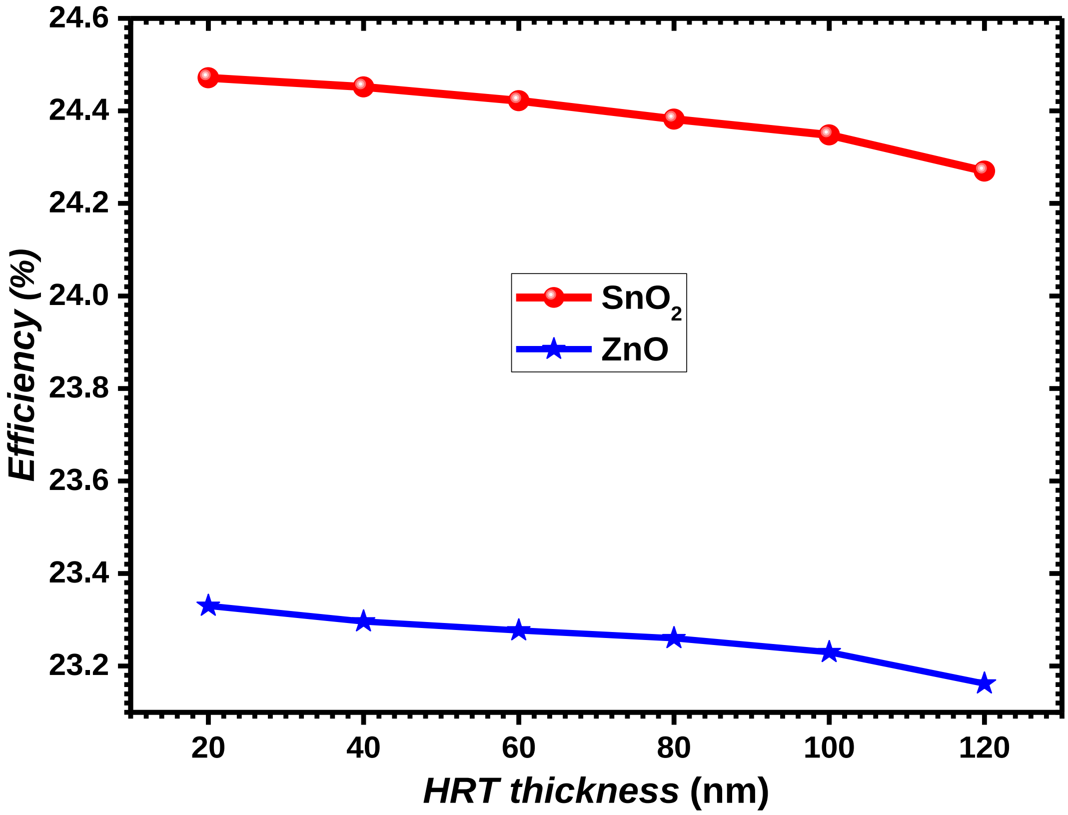

Figure 4.19: Cell efficiency as a function of the HRT layer thickness.

4.9 Influences of temperature on cell performance

Finally, one of the important factors that generally also affect the efficiency of cells is temperature, as it is well known that higher temperatures lead to lower efficiency. To investigate and understand the stability of the optimized CdTe solar cell with HT-EBL, the influence of temperature shifted from 270 to 330 K on the performance is studied, and the variation of efficiency is illustrated in Figure 4.20. As expected, we can see that the efficiency linearly declines with increasing temperature. Reasons for the decline in efficiency can be traced back to the materials parameters such as band gap, electron and hole mobility, and density of states in materials that are affected by temperature. The recombination between energy bands is accelerated due to the high temperature dependent EHP induced in the solar cell and, consequently, reducing the performance of the solar cell [151]. This study is in good agreement with reported literature [77,134,162,170].

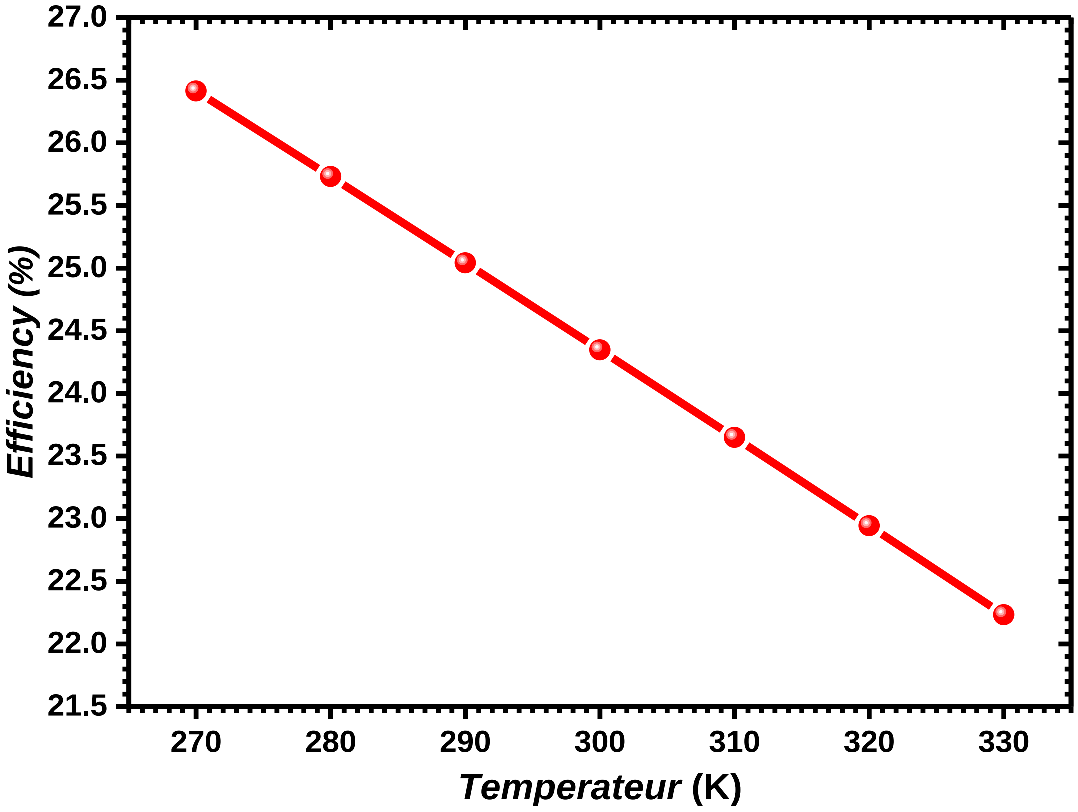

Figure 4.20: Cell efficiency as a function of temperature.

4.10 Conclusion

This chapter introduces the 2D-numerical simulation of the CdS/CdTe heterojunction solar cells using Silvaco-Atlas software. In the first step, a reference cell was studied and simulated. A good proportion was noticed in density current-voltage curves for both reference and experimental cells. A good performance was achieved by incorporating p-Cu_2O as a hole transport-electron blocking layer between the absorber layer CdTe and the metal back contact layer. This layer can contribute to increasing cell efficiency if the optimal values are given to the doping concentration, thickness, and carrier lifetime for each layer. Optimum conversion efficiency up to 24.35% was obtained for optimized cell structure. The optimized cell structure consists of Cu_2O, CdTe, CdS, SnO_2, and TCO layers. The thicknesses is about 50, 2000, 50, 100, and 100 nm with the doping concentrations of 5×10^{18} cm^{-3}, 2×10^{16} cm^{-3}, 1×10^{16} cm^{-3}, 1×10^{18} cm^{-3}, 3×10^{20} cm^{-3}, respectively. The calculations were made using 10 ns as a carrier lifetime of the CdTe absorber layer and with an incident irradiance of 1000 W/m^2 and at an operating temperature of 300 K. These obtained parameters are in good agreement with the previous ones. Also, as an alternative to the SnO_2 HRT layer, ZnO was used, and the results showed that SnO_2 has better performance than ZnO at the level of this region (HRT layer) in a CdTe solar cell. Finally, we studied the influence of temperature on the optimized CdTe solar cell, and as expected, we noticed a linear degradation in efficiency with increasing temperature. The performance results advocate developing CdS/CdTe/Cu_2O heterojunction solar cells experimentally.

GENERAL CONCLUSION

General conclusion

In this work, numerical modeling of II-IV compounds-based thin-film solar cells was performed. The goal was to optimize the structures of CdTe solar cells in order to obtain a better performance. We have chosen the parametric optimization method, which is the most widely used and effective method to improve the performance of these structures as we have already indicated. In addition, we tried to reduce the problems of recombination through the interlayer (HT-EBL or BSF), which is usually used at the level of the back contact. In the first part, we introduced some new statistics on electrical energy and its consumption in the world while explaining the necessity for people to move towards renewable energy sources, especially solar cells because of their capacity. to provide sufficient energy. We also discussed thin-films solar cells and the evolution of the production of CdTe solar cells compared to other thin-films solar cells, and showed that this type is good and capable of competing in the PV market. Since this thesis is devoted to solar cells, it was necessary to present some basic information on semiconductors and p-n junctions, as well as on the photovoltaic effect and solar radiation, besides the main characteristics and the different types of solar cells. Therefore, all this was brought up in the first chapter. Then we gave in the second chapter the properties of the materials utilized in our simulations, , namely II-VI compound semiconductors: CdTe, CdS, and ZnO. In addition to Tin and Cuprous oxide films (SnO_2 and Cu_2O). It was also in the same chapter that we presented and discussed the common structures of CdS/CdTe solar cells and the losses problems that limit cell efficiency. As solutions, we displayed different methods that can enhance the performance of cells, especially those that limit problems of recombination at the back contact. We moved after that to the third chapter where we described the fundamental equations in semiconductors such as Poisson's equation, continuity, and transport equations, plus the different types of recombination mechanisms, with the aim of presenting and comprehending the phenomena and the equations, on which most semiconductors devices simulator depend. The next step was to introduce the simulation software TCAD-SILVACO and Atlas tool used in our simulation work of the CdTe solar cells with explanation of the mode of working and the sequence of its commands, in addition to different models down to how to extract the Photovoltaic parameters (J_{sc}, V_{oc}, FF, and η) of solar cells. In the fourth chapter using Silvaco-Atlas software, we advanced to the numerical framing that deals with the performance analysis of CdTe thin-film solar cells by means of an accurate numerical simulation. Initially, we described the simulated conventional structure of the CdS/CdTe solar cell (reference cell), the physical models, and all parameters used in our simulations. The numerical simulation of the solar cell based on FTO/i-SnO_2/CdS/CdTe allowed us to calculate the photovoltaic parameters that characterize the solar cell, and we observed a good agreement between the simulation results and recent experimental data reported in literature. The following step after validating our simulation was to improve cell performances by incorporating p-Cu_2O as an HT-EBL layer, between the absorber layer CdTe and the metal back contact layer in order to form an ohmic contact and reduce carrier recombination losses. High performance was obtained by optimizing the cell parameters in terms of thickness, doping concentration, and carrier lifetime of the CdTe absorbent layer. The efficiency of the structure increased by 10.35% compared to the recent experimental results. Furthermore, the proposed structure consisting of FTO/i-SnO_2/CdS/CdTe/Cu_2O presented the best conversion efficiency of 24.35%, a short circuit current density of 27.59 mA/cm^2, an open-circuit voltage of 1.03 V and a fill-factor of 85.83%, under an air mass 1.5 global spectrum (AM1.5G) and at an operating temperature of 300 K. The ZnO film was investigated as an alternative HRT layer to SnO_2, and the simulation results indicated that i-ZnO is less effective than i-SnO_2. Finally, the last step in our simulations studies was assessing the effect of temperature on the optimal solar cell device, where it turns out that lower temperatures increase cell performances whereas higher temperatures cause its degradation. The performance results obtained with our simulations advocate the development of high-efficiency CdS/CdTe/Cu_2O solar cells experimentally, using high-purity materials and an appropriate fabrication method. The modeling results and analyses presented in this work are expected to lower costs, facilitate the design, and allow the CdTe PV community and the designers to focus on the parameters that make a difference in the final design of the CdTe cell. We also hope that our work will serve as a guide for future works specialized in the modeling and simulation of new solar cell devices and their optimization.

The perspectives that emerge from this work need to be researched and investigated in the future in order to reach even higher efficiencies. These specifically relate to the following points:

- A front contact of CdTe solar cell and anti-reflective coatings (ARC) technology.
- Other materials for the HT-EBL layer of CdTe solar cell and the search for other strategies for forming and facilitating an ohmic back contact.
- Investigation of alternative window layers to CdS such as MZO, ZrS_2 and ZnS, etc.
- Tandem and triple cells based on (CdTe, Perovskite, Si, and Sb_2Se_3).

REFERENCES

References

[1] Enerdata, Electricity domestic consumption, (n.d.). https://yearbook.enerdata.net/electricity/electricity-domestic-consumption-data.html (accessed January 25, 2022).

[2] I.E.A. Pvps, Trends 2021 in Photovoltaic applications, Report No. IEA-PVPS T1-41. (2021).

[3] B. IEA, Renewables 2020 Analysis and forecast to 2025, (2020).

[4] International Agency Energy (IEA), Evolution of Solar PV Module Cost by Data Source, 1970-2020. (n.d.). https://www.iea.org/data-and-statistics/charts/evolution-of-solar-pv-module-cost-by-data-source-1970-2020 (accessed March 7, 2022).

[5] P. Breeze, Power generation technologies, Newnes, 2019.

[6] T.L. Chu, S.S. Chu, Thin film II–VI photovoltaics, Solid-State Electronics. 38 (1995) 533–549.

[7] R.N. Bhargava, II-VI Semiconductor Materials and Devices—Recent Progress, in: Proceedings of the 17th International Conference on the Physics of Semiconductors, Springer, 1985: pp. 1531–1536.

[8] I.E. Tinedert, F. Pezzimenti, M.L. Megherbi, A. Saadoune, Design and simulation of a high efficiency CdS/CdTe solar cell, Optik. 208 (2020) 164112.

[9] M.A. Green, E.D. Dunlop, J. Hohl-Ebinger, M. Yoshita, N. Kopidakis, X. Hao, Solar cell efficiency tables (version 56), Progress in Photovoltaics: Research and Applications. 28 (2020) 629–638.

[10] D.E. Swanson, J.R. Sites, W.S. Sampath, Co-sublimation of CdSexTe1− x layers for CdTe solar cells, Solar Energy Materials and Solar Cells. 159 (2017) 389–394.

[11] Fraunhofer Institute for Solar Energy Systems, PHOTOVOLTAICS REPORT, (2021).

[12] H. Czichos, T. Saito, L. Smith, Springer handbook of materials measurement methods, Springer, Berlin, 2006.

[13] G. Schirripa Spagnolo, F. Leccese, M. Leccisi, LED as Transmitter and Receiver of Light: A Simple Tool to Demonstration Photoelectric Effect, Crystals. 9 (2019) 531.

[14] Silvaco Atlas User’s Manual Device Simulation Software, Santa Clara, CA, 2016.

[15] O. Manasreh, Semiconductor heterojunctions and nanostructures, McGraw-Hill, Inc., 2005.

[16] A. Iljinas, L. Marcinauskas, Formation of bismuth oxide nanostructures by reactive plasma assisted thermal evaporation, Thin Solid Films. 594 (2015) 192–196.

[17] S.M. Sze, M.-K. Lee, Semiconductor Devices: Physics and Technology: Physics and Technology, Wiley Global Education, 2012.

[18] M. Al Amin, M.A. Sayem, International Journal of Advanced Multidisciplinary Research, Int. J. Adv. Multidiscip. Res. 7 (2020) 1–8.

[19] A.P. Roth, J.B. Webb, D.F. Williams, Band-gap narrowing in heavily defect-doped ZnO, Physical Review B. 25 (1982) 7836.

[20] K. Mertens, Photovoltaics: fundamentals, technology, and practice, John Wiley & Sons, 2018.

[21] Y. MAROUF, Etude et simulation des cellules solaires multi-jonctions à base de matériaux semi-conducteurs III-V, Doctoral dissertation, Department of Electrical Engineering, Mohamed Khider University, 2019.

[22] SOLAR CELL OPERATIONAL PRINCIPLES, (n.d.). https://ocw.tudelft.nl/wp-content/uploads/solar_energy_section_8_1.pdf (accessed December 22, 2020).

[23] T.L. Floyd, Electronic devices: conventional current version, Pearson, 2012.

[24] G.K. Vijaya, III-V Dilute Nitride Multi-quantum Well Solar Cells for High Efficiency Photovoltaics, Doctoral dissertation, 2014.

[25] Reference Air Mass 1.5 Spectra Grid Modernization NREL, (n.d.). https://www.nrel.gov/grid/solar-resource/spectra-am1.5.html (accessed December 22, 2020).

[26] B. Zaidi, Introductory chapter: Introduction to photovoltaic effect, Solar Panels and Photovoltaic Materials; InTech Open: London, UK. (2018) 1–8.

[27] S. Limpert, S. Bremner, H. Linke, Reversible electron–hole separation in a hot carrier solar cell, New Journal of Physics. 17 (2015) 95004.

[28] A. KHIATI, Etude de Cellules Thermo-Photovoltaïques Solaires à base de Semi-conducteur II-VI à petit gap CdTe / CdS / CdSe / CdZnSe / CdZnTe, Magister memory, Department of Physique, University of Oran1 Ahmed Ben Bella,Oran, 2013, n.d.

[29] S. LAZNEK, Simulation numérique des caractéristiques électriques d'une cellule solaire pin à puits quantiques à base de mixture d'Aluminium et d'Arséniure de Galium, Doctoral dissertation, Department of Science Material, Mohamed Khider University, Biskra, 2019.

[30] T. Markvart, L. Castaner, Solar Cells: Materials, Manufacturing and Operation. (2005) 84.

[31] S.H. Demtsu, Impact of back-contact materials on performance and stability of cadmium sulfide/cadmium telluride solar cells, Colorado State University, 2006.

[32] G. AZZOUZI, Study of silicon solar cells performances using the impurity photovoltaic effect, Doctoral dissertation, Department of Physique, Ferhat Abbas University, Sétif, 2014.

[33] C.M. Hussain, Handbook of nanomaterials for industrial applications, Elsevier, 2018.

[34] J.A. Luceño-Sánchez, A.M. Díez-Pascual, R. Peña Capilla, Materials for photovoltaics: State of art and recent developments, International Journal of Molecular Sciences. 20 (2019) 976.

[35] Best research-cell efficiencies chart. NREL, (n.d.). https://www.nrel.gov/pv/cell-efficiency.html (accessed December 22, 2020).

[36] S. Chala, Design and investigate of II-VI thin film solar cells, Doctoral dissertation, Department of Science Material, Mohamed Khider University, Biskra, 2017.

[37] F. Tinjod, Mécanismes de formation des boîtes quantiques semiconductrices, application aux nanostructures II-VI et étude de leurs propriétés optiques, Doctoral dissertation, University of Joseph-Fourier-Grenoble I, 2003.

[38] M. Isshiki, J. Wang, Wide-Bandgap II-VI semiconductors: growth and properties, in: Springer Handbook of Electronic and Photonic Materials, Springer, 2017: p. 1.

[39] K.S. Ramaiah, R.D. Pilkington, A.E. Hill, R.D. Tomlinson, A.-K. Bhatnagar, Structural and optical investigations on CdS thin films grown by chemical bath technique, Materials Chemistry and Physics. 68 (2001) 22–30.

[40] A. Bosio, N. Romeo, S. Mazzamuto, V. Canevari, Polycrystalline CdTe thin films for photovoltaic applications, Progress in Crystal Growth and Characterization of Materials. 52 (2006) 247–279.

[41] G. Mandel, Self-compensation limited conductivity in binary semiconductors. I. Theory, Physical Review. 134 (1964) A1073.

[42] K. Nishidate, T. Sato, Y. Matsukura, M. Baba, M. Hasegawa, T. Sasaki, Density-functional electronic structure calculations for native defects and Cu impurities in CdS, Physical Review B. 74 (2006) 35210.

[43] E. Mourad, Doctorat LMD en Electronique Etude par simulation numérique d ’ une cellule solaire en CIGS à multi -jonction par le logiciel Tcad Silvaco, Doctoral dissertation, Department of Electrical Engineering, Mohamed Khider University, 2018.

[44] S.J.C. Irvine, V. Barrioz, D. Lamb, E.W. Jones, R.L. Rowlands-Jones, MOCVD of thin film photovoltaic solar cells—Next-generation production technology?, Journal of Crystal Growth. 310 (2008) 5198–5203.

[45] C.S. Ferekides, D. Marinskiy, V. Viswanathan, B. Tetali, V. Palekis, P. Selvaraj, D.L. Morel, High efficiency CSS CdTe solar cells, Thin Solid Films. 361 (2000) 520–526.

[46] J. Britt, C. Ferekides, Thin-film CdS/CdTe solar cell with 15.8% efficiency, Applied Physics Letters. 62 (1993) 2851–2852.

[47] N.R. Paudel, Y. Yan, Fabrication and characterization of high-efficiency CdTe-based thin-film solar cells on commercial SnO2: F-coated soda-lime glass substrates, Thin Solid Films. 549 (2013) 30–35.

[48] X.-D. Liu, T. Xing, First-principles calculations of electronic structures and optical

properties of group-IIIA elements doped wurtzite CdS, Solid State Communications. 187 (2014) 72–76.

[49] R.E. Treharne, A. Seymour-Pierce, K. Durose, K. Hutchings, S. Roncallo, D. Lane, Optical design and fabrication of fully sputtered CdTe/CdS solar cells, in: Journal of Physics: Conference Series, IOP Publishing, 2011: p. 12038.

[50] S. Adachi, Properties of semiconductor alloys: group-IV, III-V and II-VI semiconductors, John Wiley & Sons, 2009.

[51] H.P. Mahabaduge, W.L. Rance, J.M. Burst, M.O. Reese, D.M. Meysing, C.A. Wolden, J. Li, J.D. Beach, T.A. Gessert, W.K. Metzger, S. Garner, T.M. Barnes, High-efficiency, flexible CdTe solar cells on ultra-thin glass substrates, Applied Physics Letters. 106 (2015) 3–7. https://doi.org/10.1063/1.4916634.

[52] A.A.J. Al-Douri, F.Y. Al-Shakily, M.F.A. Alias, A.A. Alnajjar, Optical properties of Al- and Sb-doped CdTe thin films, Advances in Condensed Matter Physics. 2010 (2010).

[53] X. Wu, High-efficiency polycrystalline CdTe thin-film solar cells, Solar Energy. 77 (2004) 803–814. https://doi.org/10.1016/j.solener.2004.06.006.

[54] A.J. Strauss, The physical properties of cadmium telluride, Revue de Physique Appliquée. 12 (1977) 167–184.

[55] A.L. Fahrenbruch, II–VI compounds in solar energy conversion, Journal of Crystal Growth. 39 (1977) 73–91.

[56] A. Shepidchenko, S. Mirbt, B. Sanyal, A. Håkansson, M. Klintenberg, Tailoring of defect levels by deformations: Te-antisite in CdTe, Journal of Physics: Condensed Matter. 25 (2013) 415801.

[57] B.E. McCandless, R.W. Birkmire, W.A. Buchanan, Vapor transport deposition of cadmium telluride films, in: Conference Record of the Twenty-Ninth IEEE Photovoltaic Specialists Conference, 2002., IEEE, 2002: pp. 547–550.

[58] M. Arreguín-Campos, K.G. ZB, J.G. Quiñones-Galván, J. Santos-Cruz, S.A. Mayén-Hernández, O. Zelaya-Angel, M. de la L. Olvera, G. Contreras-Puente, F. de Moure-Flores, Fabrication of CdS/CdTe Heterostructures by Chemical Synthesis Using ap-Type CdTe Film Grown by Electrodeposition Employing EDTA as Strong Complexing Agent, Journal of Electronic Materials. 48 (2019) 3595–3602.

[59] A. Gupta, A.D. Compaan, All-sputtered 14% CdS⁄CdTe thin-film solar cell with ZnO: Al transparent conducting oxide, Applied Physics Letters. 85 (2004) 684–686.

[60] B.G. Mendis, D. Gachet, J.D. Major, K. Durose, Long lifetime hole traps at grain boundaries in CdTe thin-film photovoltaics, Physical Review Letters. 115 (2015) 218701.

[61] L. Kranz, C. Gretener, J. Perrenoud, R. Schmitt, F. Pianezzi, F. La Mattina, P. Blösch, E. Cheah, A. Chirilă, C.M. Fella, Doping of polycrystalline CdTe for high-efficiency solar cells on flexible metal foil, Nature Communications. 4 (2013) 1–7.

[62] S. Khosroabadi, S.H. Keshmiri, Design of a high efficiency ultrathin CdS/CdTe solar cell

using back surface field and backside distributed Bragg reflector, Optics Express. 22 (2014) A921. https://doi.org/10.1364/OE.22.00A921.

[63] I. Hernandez-Calderon, Optical properties and electronic structure of wide band gap II-VI semiconductors, in: II-VI Semiconductor Materials and Their Applications, Routledge, 2018: pp. 113–170.

[64] V.M. Fthenakis, Life cycle impact analysis of cadmium in CdTe PV production, Renewable and Sustainable Energy Reviews. 8 (2004) 303–334.

[65] V. Fthenakis, Sustainability of photovoltaics: The case for thin-film solar cells, Renewable and Sustainable Energy Reviews. 13 (2009) 2746–2750.

[66] E.A. Alsema, M.J. de Wild-Scholten, Environmental life cycle assessment of advanced silicon solar cell technologies, in: Presented at the 19th European Photovoltaic Solar Energy Conference, 2004: p. 11.

[67] V.M. Fthenakis, E.A. Alsema, M.J. de Wild-Scholten, Life cycle assessment of photovoltaics: perceptions, needs, and challenges, in: Conference Record of the Thirty-First IEEE Photovoltaic Specialists Conference, 2005., IEEE, 2005: pp. 1655–1658.

[68] V. Fthenakis, E. Alsema, Photovoltaics energy payback times, greenhouse gas emissions and external costs: 2004–early 2005 status, Progress in Photovoltaics: Research and Applications. 14 (2006) 275–280.

[69] V.M. Fthenakis, H.C. Kim, E. Alsema, Emissions from photovoltaic life cycles, Environmental Science & Technology. 42 (2008) 2168–2174.

[70] S. Kaczmar, Evaluating the read-across approach on CdTe toxicity for CdTe photovoltaics, in: Society of Environmental Toxicology and Chemistry (SETAC) North America 32nd Annual Meeting, 2011: pp. 13–17.

[71] H. Steinberger, Health, safety and environmental risks from the operation of CdTe and CIS thin-film modules, Progress in Photovoltaics: Research and Applications. 6 (1998) 99–103.

[72] J. Zayed, S. Philippe, Acute oral and inhalation toxicities in rats with cadmium telluride, International Journal of Toxicology. 28 (2009) 259–265.

[73] G. Womack, P.M. Kaminski, J.M. Walls, Optical optimization of high resistance transparent layers in thin film cadmium telluride solar cells, Vacuum. 139 (2017) 196–201.

[74] M. Nichterwitz, R. Caballero, C.A. Kaufmann, H.-W. Schock, T. Unold, Generation-dependent charge carrier transport in Cu (In, Ga) Se2/CdS/ZnO thin-film solar-cells, Journal of Applied Physics. 113 (2013) 44515.

[75] C. Klingshirn, ZnO: material, physics and applications, ChemPhysChem. 8 (2007) 782–803.

[76] Ü. Özgür, Y.I. Alivov, C. Liu, A. Teke, Ma. Reshchikov, S. Doğan, V. Avrutin, S.-J. Cho, and H. Morkoç, A comprehensive review of ZnO materials and devices, Journal of

Applied Physics. 98 (2005) 11.

[77] C. Doroody, K.S. Rahman, H.N. Rosly, M.N. Harif, F. Haque, S.K. Tiong, N. Amin, Impact of high resistivity transparent (HRT) layer in cadmium telluride solar cells from numerical simulation, Journal of Renewable and Sustainable Energy. 12 (2020) 23702.

[78] S. Dabbabi, T. Ben Nasr, N. Kamoun-Turki, Parameters optimization of CIGS solar cell using 2D physical modeling, Results in Physics. 7 (2017) 4020–4024.

[79] S. Fay, U. Kroll, C. Bucher, E. Vallat-Sauvain, A. Shah, Low pressure chemical vapour deposition of ZnO layers for thin-film solar cells: temperature-induced morphological changes, Solar Energy Materials and Solar Cells. 86 (2005) 385–397.

[80] A. Smith, R. Rodriguez-Clemente, Morphological differences in ZnO films deposited by the pyrosol technique: effect of HCl, Thin Solid Films. 345 (1999) 192–196.

[81] A.M. Peiró, J.A. Ayllón, J. Peral, X. Domènech, C. Domingo, Microwave activated chemical bath deposition (MW-CBD) of zinc oxide: Influence of bath composition and substrate characteristics, Journal of Crystal Growth. 285 (2005) 6–16.

[82] D.S. Ginley, J.D. Perkins, Transparent conductors, in: Handbook of Transparent Conductors, Springer, 2011: pp. 1–25.

[83] K. Bennaceur, Elaboration and characterization of SnO2: In thin films deposited by spray pyrolysis technique, Doctoral dissertation, Department of Science Material, Mohamed Khider University, Biskra, 2020.

[84] K.G. Godinho, A. Walsh, G.W. Watson, Energetic and electronic structure analysis of intrinsic defects in SnO2, The Journal of Physical Chemistry C. 113 (2009) 439–448.

[85] D. Zhang, L. Tao, Z. Deng, J. Zhang, L. Chen, Surface morphologies and properties of pure and antimony-doped tin oxide films derived by sol–gel dip-coating processing, Materials Chemistry and Physics. 100 (2006) 275–280.

[86] N. Najafi, S.M. Rozati, Structural and electrical properties of SnO2: F thin films prepared by chemical vapor deposition method, Acta Physica Polonica: A. 131 (2017) 222–225.

[87] D.B. Fraser, H.D. Cook, Highly Conductive, Transparent Films of Sputtered In2− x Sn x O 3− y, Journal of the Electrochemical Society. 119 (1972) 1368.

[88] N.A. Bakr, S.A. Salman, M.N. Ali, Effect of fluorine doping on structural and optical properties of SnO2 thin films prepared by chemical spray pyrolysis method, Advances in Materials. 5 (2016) 23–30.

[89] B.K. Meyer, A. Polity, D. Reppin, M. Becker, P. Hering, P.J. Klar, T. Sander, C. Reindl, J. Benz, M. Eickhoff, Binary copper oxide semiconductors: From materials towards devices, Physica Status Solidi (B). 249 (2012) 1487–1509.

[90] Y.H. Khattak, F. Baig, S. Ullah, B. Marí, S. Beg, K. Khan, Effect of Cu2O hole transport layer and improved minority carrier life time on the efficiency enhancement of Cu2NiSnS4 based experimental solar cell, Journal of Renewable and Sustainable Energy. 10 (2018) 43502.

[91] C. Malerba, F. Biccari, C.L.A. Ricardo, M. D'Incau, P. Scardi, A. Mittiga, Absorption coefficient of bulk and thin film Cu2O, Solar Energy Materials and Solar Cells. 95 (2011) 2848–2854.

[92] A. Chen, H. Long, X. Li, Y. Li, G. Yang, P. Lu, Controlled growth and characteristics of single-phase Cu2O and CuO films by pulsed laser deposition, Vacuum. 83 (2009) 927–930.

[93] R. Wick, S.D. Tilley, Photovoltaic and photoelectrochemical solar energy conversion with Cu2O, The Journal of Physical Chemistry C. 119 (2015) 26243–26257.

[94] A. Karapetyan, A. Reymers, S. Giorgio, C. Fauquet, L. Sajti, S. Nitsche, M. Nersesyan, V. Gevorgyan, W. Marine, Cuprous oxide thin films prepared by thermal oxidation of copper layer. Morphological and optical properties, Journal of Luminescence. 159 (2015) 325–332.

[95] V.F. Drobny, L. Pulfrey, Properties of reactively-sputtered copper oxide thin films, Thin Solid Films. 61 (1979) 89–98.

[96] A.Y. Oral, E. Menşur, M.H. Aslan, E. Başaran, The preparation of copper (II) oxide thin films and the study of their microstructures and optical properties, Materials Chemistry and Physics. 83 (2004) 140–144.

[97] A. Goltzené, C. Schwab, Impurity scattering effect on the cyclotron resonance of carriers in Cu2O, Physica Status Solidi (B). 92 (1979) 483–487.

[98] E. Fortin, P. Rochon, J.P. Zielinger, Photoconductivity and photovoltaic excitation spectra and their wavelength derivative in Cu2O, Journal of Physics and Chemistry of Solids. 36 (1975) 1299–1306.

[99] C. Chevallier, S. Bose, S.O.S. Hamady, N. Fressengeas, Numerical investigations of the impact of buffer germanium composition and low cost fabrication of Cu2O on AZO/ZnGeO/Cu2O solar cell performances, EPJ Photovoltaics. 12 (2021) 3.

[100] T. Minami, T. Miyata, Y. Nishi, Relationship between the electrical properties of the n-oxide and p-Cu2O layers and the photovoltaic properties of Cu2O-based heterojunction solar cells, Solar Energy Materials and Solar Cells. 147 (2016) 85–93.

[101] W. Shockley, H.J. Queisser, Detailed balance limit of efficiency of p-n junction solar cells, Journal of Applied Physics. 32 (1961) 510–519.

[102] P. Rappaport, The photovoltaic effect and its utilization, Solar Energy. 3 (1959) 8–18.

[103] T. Baines, G. Zoppi, L. Bowen, T.P. Shalvey, S. Mariotti, K. Durose, J.D. Major, Incorporation of CdSe layers into CdTe thin film solar cells, Solar Energy Materials and Solar Cells. 180 (2018) 196–204.

[104] J.M. Kephart, Optimization of the front contact to minimize short-circuit current losses in CdTe thin-film solar cells, (2015).

[105] T. Song, A. Moore, J.R. Sites, Te layer to reduce the CdTe back-contact barrier, IEEE Journal of Photovoltaics. 8 (2017) 293–298.

[106] P. Veluchamy, M. Tsuji, T. Nishio, T. Aramoto, H. Higuchi, S. Kumazawa, S. Shibutani, J. Nakajima, T. Arita, H. Ohyama, A pyrosol process to deposit large-area SnO2: F thin films and its use as a transparent conducting substrate for CdTe solar cells, Solar Energy Materials and Solar Cells. 67 (2001) 179–185.

[107] J. Perrenoud, L. Kranz, S. Buecheler, F. Pianezzi, A.N. Tiwari, The use of aluminium doped ZnO as transparent conductive oxide for CdS/CdTe solar cells, Thin Solid Films. 519 (2011) 7444–7448.

[108] B.L. Williams, J.D. Major, L. Bowen, L. Phillips, G. Zoppi, I. Forbes, K. Durose, Challenges and prospects for developing CdS/CdTe substrate solar cells on Mo foils, Solar Energy Materials and Solar Cells. 124 (2014) 31–38.

[109] T. Baines, Optimisation of CdTe (1-X) Se X and Mg X Zn (1-X) O Layers for CdTe PV Devices, Doctoral dissertation, The University of Liverpool (United Kingdom), 2020.

[110] S.D. Feldman, L. Mansfield, T.R. Ohno, V. Kaydanov, J.D. Beach, T. Nagle, Non-uniformity mitigation in CdTe solar cells: the effects of high-resistance transparent conducting oxide buffer layers, in: Conference Record of the Thirty-First IEEE Photovoltaic Specialists Conference, 2005., IEEE, 2005: pp. 271–274.

[111] H. Mahabaduge, K. Wieland, C. Carter, V. Plotnikov, D. Giolando, Sputtered HRT layers for CdTe solar cells, in: 2011 37th IEEE Photovoltaic Specialists Conference, IEEE, 2011: pp. 1302–1304.

[112] J.M. Kephart, J.W. McCamy, Z. Ma, A. Ganjoo, F.M. Alamgir, W.S. Sampath, Band alignment of front contact layers for high-efficiency CdTe solar cells, Solar Energy Materials and Solar Cells. 157 (2016) 266–275.

[113] G. Kartopu, B.L. Williams, V. Zardetto, A.K. Gürlek, A.J. Clayton, S. Jones, W.M.M. Kessels, M. Creatore, S.J.C. Irvine, Enhancement of the photocurrent and efficiency of CdTe solar cells suppressing the front contact reflection using a highly-resistive ZnO buffer layer, Solar Energy Materials and Solar Cells. 191 (2019) 78–82.

[114] J. Lee, Comparison of CdS films deposited by different techniques: Effects on CdTe solar cell, Applied Surface Science. 252 (2005) 1398–1403.

[115] Y. Deng, J. Yang, R. Yang, K. Shen, D. Wang, D. Wang, Cu-doped CdS and its application in CdTe thin film solar cell, Aip Advances. 6 (2016) 15203.

[116] M. Marwede, A. Reller, Estimation of life cycle material costs of cadmium telluride–and copper indium gallium diselenide–photovoltaic absorber materials based on life cycle material flows, Journal of Industrial Ecology. 18 (2014) 254–267.

[117] A. Kanevce, M.O. Reese, T.M. Barnes, S.A. Jensen, W.K. Metzger, The roles of carrier concentration and interface, bulk, and grain-boundary recombination for 25% efficient CdTe solar cells, Journal of Applied Physics. 121 (2017) 214506.

[118] J.M. Burst, J.N. Duenow, D.S. Albin, E. Colegrove, M.O. Reese, J.A. Aguiar, C.-S. Jiang, M.K. Patel, M.M. Al-Jassim, D. Kuciauskas, CdTe solar cells with open-circuit voltage breaking the 1 V barrier, Nature Energy. 1 (2016) 1–8.

[119] G. Kartopu, O. Oklobia, D. Turkay, D.R. Diercks, B.P. Gorman, V. Barrioz, S. Campbell, J.D. Major, M.K. Al Turkestani, S. Yerci, Study of thin film poly-crystalline CdTe solar cells presenting high acceptor concentrations achieved by in-situ arsenic doping, Solar Energy Materials and Solar Cells. 194 (2019) 259–267.

[120] S.A. Jensen, J.M. Burst, J.N. Duenow, H.L. Guthrey, J. Moseley, H.R. Moutinho, S.W. Johnston, A. Kanevce, M.M. Al-Jassim, W.K. Metzger, Long carrier lifetimes in large-grain polycrystalline CdTe without CdCl2, Applied Physics Letters. 108 (2016) 263903.

[121] T. Potlog, L. Ghimpu, P. Gashin, A. Pudov, T. Nagle, J. Sites, Influence of annealing in different chlorides on the photovoltaic parameters of CdS/CdTe solar cells, Solar Energy Materials and Solar Cells. 80 (2003) 327–334.

[122] S.-H. Wei, S.B. Zhang, Chemical trends of defect formation and doping limit in II-VI semiconductors: The case of CdTe, Physical Review B. 66 (2002) 155211.

[123] X. Liu, A.D. Compaan, J. Terry, Cu K-edge X-ray fine structure changes in CdTe with CdCl2 processing, Thin Solid Films. 480 (2005) 95–98.

[124] C. Potamialis, Process sensitivities and interface optimisation of CdTe solar cells deposited by close-space sublimation, Doctoral dissertation, Loughborough University, 2019.

[125] T. Song, Design strategies for high-efficiency CdTe solar cells, Doctoral dissertation, Colorado State University, 2017.

[126] A. Romeo, E. Artegiani, CdTe-Based Thin Film Solar Cells: Past, Present and Future, Energies. 14 (2021) 1684.

[127] X. Li, D.W. Niles, F.S. Hasoon, R.J. Matson, P. Sheldon, Effect of nitric-phosphoric acid etches on material properties and back-contact formation of CdTe-based solar cells, Journal of Vacuum Science & Technology A: Vacuum, Surfaces, and Films. 17 (1999) 805–809.

[128] S.G. Kumar, K.S.R.K. Rao, Physics and chemistry of CdTe/CdS thin film heterojunction photovoltaic devices: fundamental and critical aspects, Energy & Environmental Science. 7 (2014) 45–102.

[129] R. Ochoa-Landin, O. Vigil-Galan, Y. V Vorobiev, R. Ramírez-Bon, Chemically-deposited Te layers improving the parameters of back contacts for CdTe solar cells, Solar Energy. 83 (2009) 134–138.

[130] H.C. Chou, A. Rohatgi, E.W. Thomas, S. Kamra, A.K. Bhat, Effects of Cu on CdTe/CdS heterojunction solar cells with Au/Cu contacts, Journal of The Electrochemical Society. 142 (1995) 254.

[131] C.R. Corwine, A.O. Pudov, M. Gloeckler, S.H. Demtsu, J.R. Sites, Copper inclusion and migration from the back contact in CdTe solar cells, Solar Energy Materials and Solar Cells. 82 (2004) 481–489.

[132] W. Jaegermann, A. Klein, T. Mayer, Interface engineering of inorganic thin-film solar

cells–materials-science challenges for advanced physical concepts, Advanced Materials. 21 (2009) 4196–4206.

[133] J. Türck, H. Nonnenmacher, P.M.L. Connor, S. Siol, B. Siepchen, J.P. Heimfarth, A. Klein, W. Jaegermann, Copper (I) oxide (Cu2O) based back contact for p-i-n CdTe solar cells, Progress in Photovoltaics: Research and Applications. 24 (2016) 1229–1236.

[134] N. Amin, M.A. Matin, M.M. Aliyu, M.A. Alghoul, M.R. Karim, K. Sopian, Prospects of back surface field effect in ultra-thin high-efficiency CdS/CdTe solar cells from numerical modeling, International Journal of Photoenergy. 2010 (2010).

[135] R.P. Gale, J.C.C. Fan, G.W. Turner, R.L. Chapman, A new high-efficiency GaAs solar cell structure using a heterostructure back-surface field, in: 17th Photovoltaic Specialists Conference, 1984: pp. 1422–1425.

[136] P.D. DeMoulin, M.S. Lundstrom, R.J. Schwartz, Back-surface field design for n+ p GaAs cells, Solar Cells. 20 (1987) 229–236.

[137] P.D. DeMoulin, M.S. Lundstrom, Projections of GaAs solar-cell performance limits based on two-dimensional numerical simulation, IEEE Transactions on Electron Devices. 36 (1989) 897–905.

[138] A. Kuddus, M.F. Rahman, S. Ahmmed, J. Hossain, A.B.M. Ismail, Role of facile synthesized V2O5 as hole transport layer for CdS/CdTe heterojunction solar cell: validation of simulation using experimental data, Superlattices and Microstructures. 132 (2019) 106168.

[139] T.A. Gessert, S. Asher, S. Johnston, M. Young, P. Dippo, C. Corwine, Analysis of cds/cdte devices incorporating a znte: Cu/ti contact, Thin Solid Films. 515 (2007) 6103–6106.

[140] D. Rioux, D.W. Niles, H. Höchst, ZnTe: A potential interlayer to form low resistance back contacts in CdS/CdTe solar cells, Journal of Applied Physics. 73 (1993) 8381–8385.

[141] A. Mondal, B.E. McCandless, R.W. Birkmire, Electrochemical deposition of thin ZnTe films as a contact for CdTe solar cells, Solar Energy Materials and Solar Cells. 26 (1992) 181–187.

[142] N. Amin, A. Yamada, M. Konagai, Effect of ZnTe and CdZnTe Alloys at the Back Contact of 1-µm-Thick CdTe Thin Film Solar Cells, Japanese Journal of Applied Physics. 41 (2002) 2834.

[143] N. Amin, K. Sopian, M. Konagai, Numerical modeling of CdS/CdTe and CdS/CdTe/ZnTe solar cells as a function of CdTe thickness, Solar Energy Materials and Solar Cells. 91 (2007) 1202–1208.

[144] N. Romeo, A. and Bosio, A. Romeo, An innovative process suitable to produce high-efficiency CdTe/CdS thin-film modules, Solar Energy Materials and Solar Cells. 94 (2010) 2–7.

[145] N. Romeo, A. Bosio, V. Canevari, A. Podesta, Recent progress on CdTe/CdS thin film

solar cells, Solar Energy. 77 (2004) 795–801.

[146] K. Shen, R. Yang, D. Wang, M. Jeng, S. Chaudhary, K. Ho, D. Wang, Stable CdTe solar cell with V2O5 as a back contact buffer layer, Solar Energy Materials and Solar Cells. 144 (2016) 500–508.

[147] A. Kuddus, A.B.M. Ismail, J. Hossain, Design of a highly efficient CdTe-based dual-heterojunction solar cell with 44% predicted efficiency, Solar Energy. 221 (2021) 488–501.

[148] Y. Wang, P. Miska, D. Pilloud, D. Horwat, F. Mücklich, J.-F. Pierson, Transmittance enhancement and optical band gap widening of Cu2O thin films after air annealing, Journal of Applied Physics. 115 (2014) 73505.

[149] J. Piprek, Optoelectronic devices, Springer, 2005.

[150] A. Reinders, P. Verlinden, W. Van Sark, A. Freundlich, Photovoltaic solar energy: from fundamentals to applications, John Wiley & Sons, 2017.

[151] Y.H. Khattak, Modeling of high power conversion efficiency thin film solar cells, (2019).

[152] About Silvaco, (n.d.). https://silvaco.com.cn/company/30th-year.html (accessed October 29, 2021).

[153] D. Guo, D. Vasileska, 1D fast transient simulator for modeling CdS/CdTe solar cells, in: 2013 IEEE 39th Photovoltaic Specialists Conference (PVSC), IEEE, 2013: pp. 1961–1965.

[154] S. Boudour, I. Bouchama, N. Bouarissa, M. Hadjab, A study of CdTe solar cells using Ga-doped MgxZn1-xO buffer/TCO layers: Simulation and performance analysis, Journal of Science: Advanced Materials and Devices. 4 (2019) 111–115.

[155] R. Safa Sultana, A.N. Bahar, M. Asaduzzaman, K. Ahmed, Numerical modeling of a CdS/CdTe photovoltaic cell based on ZnTe BSF layer with optimum thickness of absorber layer, Cogent Engineering. 4 (2017).

[156] A. Haddout, A. Raidou, M. Fahoume, Influence of the layer parameters on the performance of the CdTe solar cells, Optoelectronics Letters. 14 (2018) 98–103.

[157] Y.P. Varshni, Temperature dependence of the energy gap in semiconductors, Physica. 34 (1967) 149–154.

[158] S.S. Pan, F.D. Li, Q.W. Liu, S.C. Xu, Y.Y. Luo, G.H. Li, Strong localization induced anomalous temperature dependence exciton emission above 300 K from SnO2 quantum dots, Journal of Applied Physics. 117 (2015) 173101.

[159] M.W. Rahman, S.N. Ahmed, S.I. Rahman, M.A. Hoque, Numerical analysis of CdTe thin film solar cells with CdS: O window layer and ZnO buffer layer, in: 2016 International Conference on Advances in Electrical, Electronic and Systems Engineering (ICAEES), IEEE, 2016: pp. 409–413.

[160] T.A.F. König, P.A. Ledin, J. Kerszulis, M.A. Mahmoud, M.A. El-Sayed, J.R. Reynolds, V. V Tsukruk, Electrically tunable plasmonic behavior of nanocube–polymer

nanomaterials induced by a redox-active electrochromic polymer, ACS Nano. 8 (2014) 6182–6192.

[161] D.W. Snoke, A.J. Shields, M. Cardona, Phonon-absorption recombination luminescence of room-temperature excitons in Cu 2 O, Physical Review B. 45 (1992) 11693.

[162] H.A.S. Al-shamiri, M.O. Sid-Ahmed, F.A. Hezam, Simulation of Performance of Cadmium Telluride Solar Cell Using AMPS-1D Program, Journal of Photonic Materials and Technology. 2 (2016) 14–19.

[163] T.L. Chu, S.S. Chu, Recent progress in thin-film cadmium telluride solar cells, Progress in Photovoltaics: Research and Applications. 1 (1993) 31–42.

[164] A.S. Mirkamali, K.K. Muminov, Simulation of the efficiency of CdS/CdTe tandem multi-junction solar cells, ArXiv Preprint ArXiv:1602.01583. (2016).

[165] M.-Y. Hsieh, S.-Y. Kuo, F.-I. Lai, M.-H. Kao, P.-H. Huang, H.W. Wang, M.-A. Tsai, H.-C. Kuo, Optimization of CdS buffer layer on the performance of copper indium gallium selenide solar cells, in: Conference on Lasers and Electro-Optics/Pacific Rim, Optical Society of America, 2011: p. C765.

[166] K. Sarkar, K. Ghosh, N. Mandal, Effect of TCO, BSF and back contact barrier on CdS/CdTe solar cell: modeling and simulation, J. Mech Contin. Math. Sci. 13 (2018) 128–140.

[167] A. Hima, A. Khechekhouche, I. Kemerchou, N. Lakhdar, B. Benhaoua, F. Rogti, I. Telli, A. Saadoun, GPVDM simulation of layer thickness effect on power conversion efficiency of CH3NH3PbI3 based planar heterojunction solar cell, International Journal of Energetica. 3 (2018) 37–41.

[168] S. Khelifi, A. Belghachi, Le rôle de la couche fenêtre dans les performances d’une cellule solaire GaAs, Rev. Energ. Ren. 7 (2004) 13–21.

[169] C. Stelling, C.R. Singh, M. Karg, T.A.F. König, M. Thelakkat, M. Retsch, Plasmonic nanomeshes: their ambivalent role as transparent electrodes in organic solar cells, Scientific Reports. 7 (2017) 1–13.

[170] F.M.T. Enam, K.S. Rahman, M.I. Kamaruzzaman, K. Sobayel, P. Chelvanathan, B. Bais, M. Akhtaruzzaman, A.R.M. Alamoud, N. Amin, Design prospects of cadmium telluride/silicon (CdTe/Si) tandem solar cells from numerical simulation, Optik. 139 (2017) 397–406.

PUBLICATIONS AND COMMUNICATIONS

Publications and communications

1. Publications:

[1] I.E. Tinedert, A. Saadoune, I. Bouchama, M.A. Saeed, Numerical modelling and optimization of CdS/CdTe solar cell with incorporation of Cu2O HT-EBL layer, Optical Materials. 106 (2020) 109970. https://doi.org/10.1016/j.optmat.2020.109970

[2] I.E. Tinedert, F. Pezzimenti, M.L. Megherbi, A. Saadoune, Design and simulation of a high efficiency CdS/CdTe solar cell, Optik. 208 (2020) 164112. https://doi.org/10.1016/j.ijleo.2019.164112

2. Communications:

[1] I.E Tinedert, A. Saadoune, Numerical simulation of the performance of CdTe solar cell using Silvaco Atlas software, ICEEB’2018 Second International Conference on Electrical Engineering, December 2-3 2018, Biskra, Algeria.

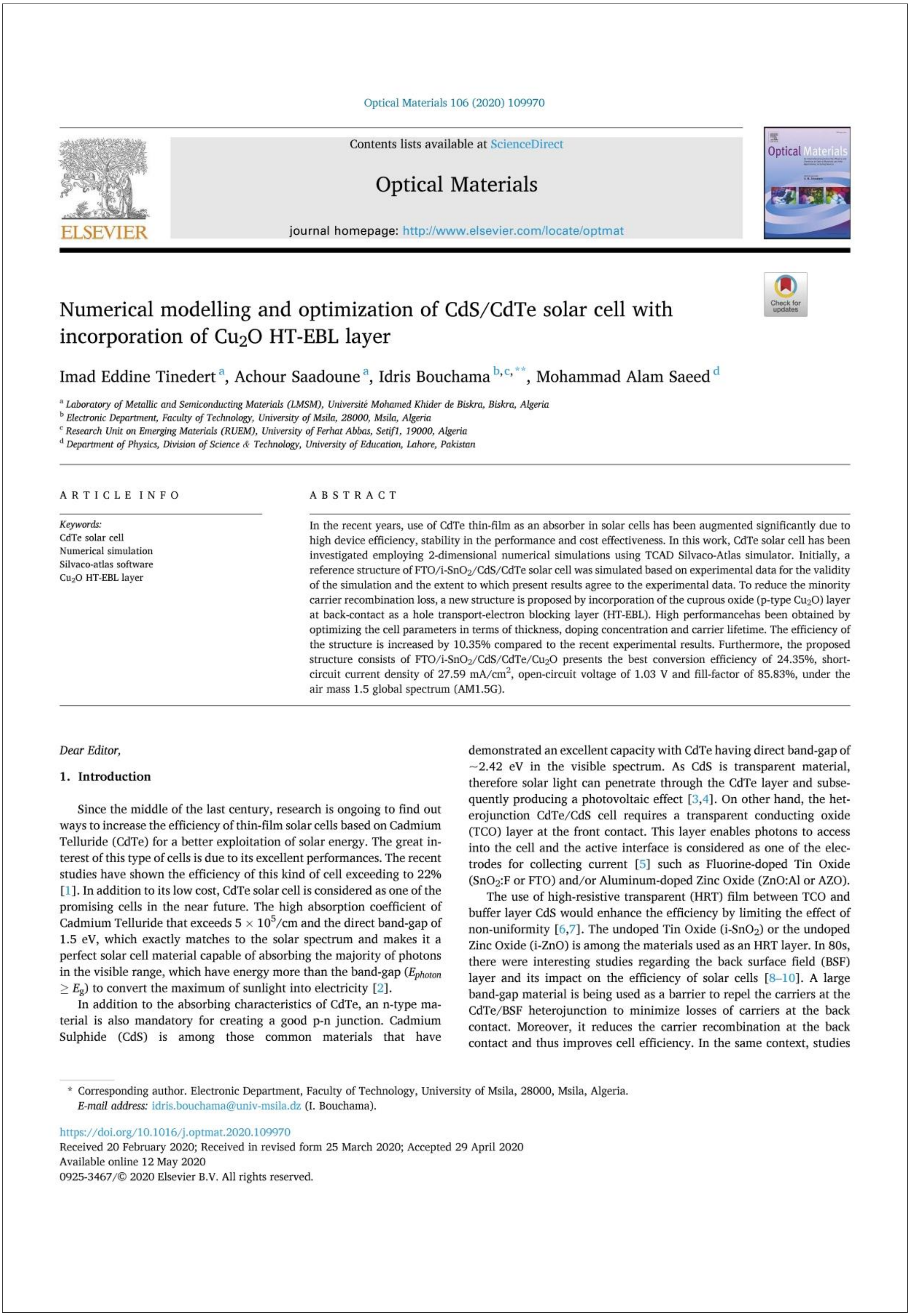

Optical Materials 106 (2020) 109970

Contents lists available at ScienceDirect

Optical Materials

journal homepage: http://www.elsevier.com/locate/optmat

Numerical modelling and optimization of CdS/CdTe solar cell with incorporation of Cu_2O HT-EBL layer

Imad Eddine Tinedert [a], Achour Saadoune [a], Idris Bouchama [b,c,**], Mohammad Alam Saeed [d]

[a] *Laboratory of Metallic and Semiconducting Materials (LMSM), Université Mohamed Khider de Biskra, Biskra, Algeria*
[b] *Electronic Department, Faculty of Technology, University of Msila, 28000, Msila, Algeria*
[c] *Research Unit on Emerging Materials (RUEM), University of Ferhat Abbas, Setif1, 19000, Algeria*
[d] *Department of Physics, Division of Science & Technology, University of Education, Lahore, Pakistan*

ARTICLE INFO

Keywords:
CdTe solar cell
Numerical simulation
Silvaco-atlas software
Cu_2O HT-EBL layer

ABSTRACT

In the recent years, use of CdTe thin-film as an absorber in solar cells has been augmented significantly due to high device efficiency, stability in the performance and cost effectiveness. In this work, CdTe solar cell has been investigated employing 2-dimensional numerical simulations using TCAD Silvaco-Atlas simulator. Initially, a reference structure of FTO/i-SnO_2/CdS/CdTe solar cell was simulated based on experimental data for the validity of the simulation and the extent to which present results agree to the experimental data. To reduce the minority carrier recombination loss, a new structure is proposed by incorporation of the cuprous oxide (p-type Cu_2O) layer at back-contact as a hole transport-electron blocking layer (HT-EBL). High performancehas been obtained by optimizing the cell parameters in terms of thickness, doping concentration and carrier lifetime. The efficiency of the structure is increased by 10.35% compared to the recent experimental results. Furthermore, the proposed structure consists of FTO/i-SnO_2/CdS/CdTe/Cu_2O presents the best conversion efficiency of 24.35%, short-circuit current density of 27.59 mA/cm^2, open-circuit voltage of 1.03 V and fill-factor of 85.83%, under the air mass 1.5 global spectrum (AM1.5G).

Dear Editor,

1. Introduction

Since the middle of the last century, research is ongoing to find out ways to increase the efficiency of thin-film solar cells based on Cadmium Telluride (CdTe) for a better exploitation of solar energy. The great interest of this type of cells is due to its excellent performances. The recent studies have shown the efficiency of this kind of cell exceeding to 22% [1]. In addition to its low cost, CdTe solar cell is considered as one of the promising cells in the near future. The high absorption coefficient of Cadmium Telluride that exceeds 5×10^5/cm and the direct band-gap of 1.5 eV, which exactly matches to the solar spectrum and makes it a perfect solar cell material capable of absorbing the majority of photons in the visible range, which have energy more than the band-gap ($E_{photon} \geq E_g$) to convert the maximum of sunlight into electricity [2].

In addition to the absorbing characteristics of CdTe, an n-type material is also mandatory for creating a good p-n junction. Cadmium Sulphide (CdS) is among those common materials that have demonstrated an excellent capacity with CdTe having direct band-gap of ~2.42 eV in the visible spectrum. As CdS is transparent material, therefore solar light can penetrate through the CdTe layer and subsequently producing a photovoltaic effect [3,4]. On other hand, the heterojunction CdTe/CdS cell requires a transparent conducting oxide (TCO) layer at the front contact. This layer enables photons to access into the cell and the active interface is considered as one of the electrodes for collecting current [5] such as Fluorine-doped Tin Oxide (SnO_2:F or FTO) and/or Aluminum-doped Zinc Oxide (ZnO:Al or AZO).

The use of high-resistive transparent (HRT) film between TCO and buffer layer CdS would enhance the efficiency by limiting the effect of non-uniformity [6,7]. The undoped Tin Oxide (i-SnO_2) or the undoped Zinc Oxide (i-ZnO) is among the materials used as an HRT layer. In 80s, there were interesting studies regarding the back surface field (BSF) layer and its impact on the efficiency of solar cells [8–10]. A large band-gap material is being used as a barrier to repel the carriers at the CdTe/BSF heterojunction to minimize losses of carriers at the back contact. Moreover, it reduces the carrier recombination at the back contact and thus improves cell efficiency. In the same context, studies

---

* Corresponding author. Electronic Department, Faculty of Technology, University of Msila, 28000, Msila, Algeria.
E-mail address: idris.bouchama@univ-msila.dz (I. Bouchama).

https://doi.org/10.1016/j.optmat.2020.109970
Received 20 February 2020; Received in revised form 25 March 2020; Accepted 29 April 2020

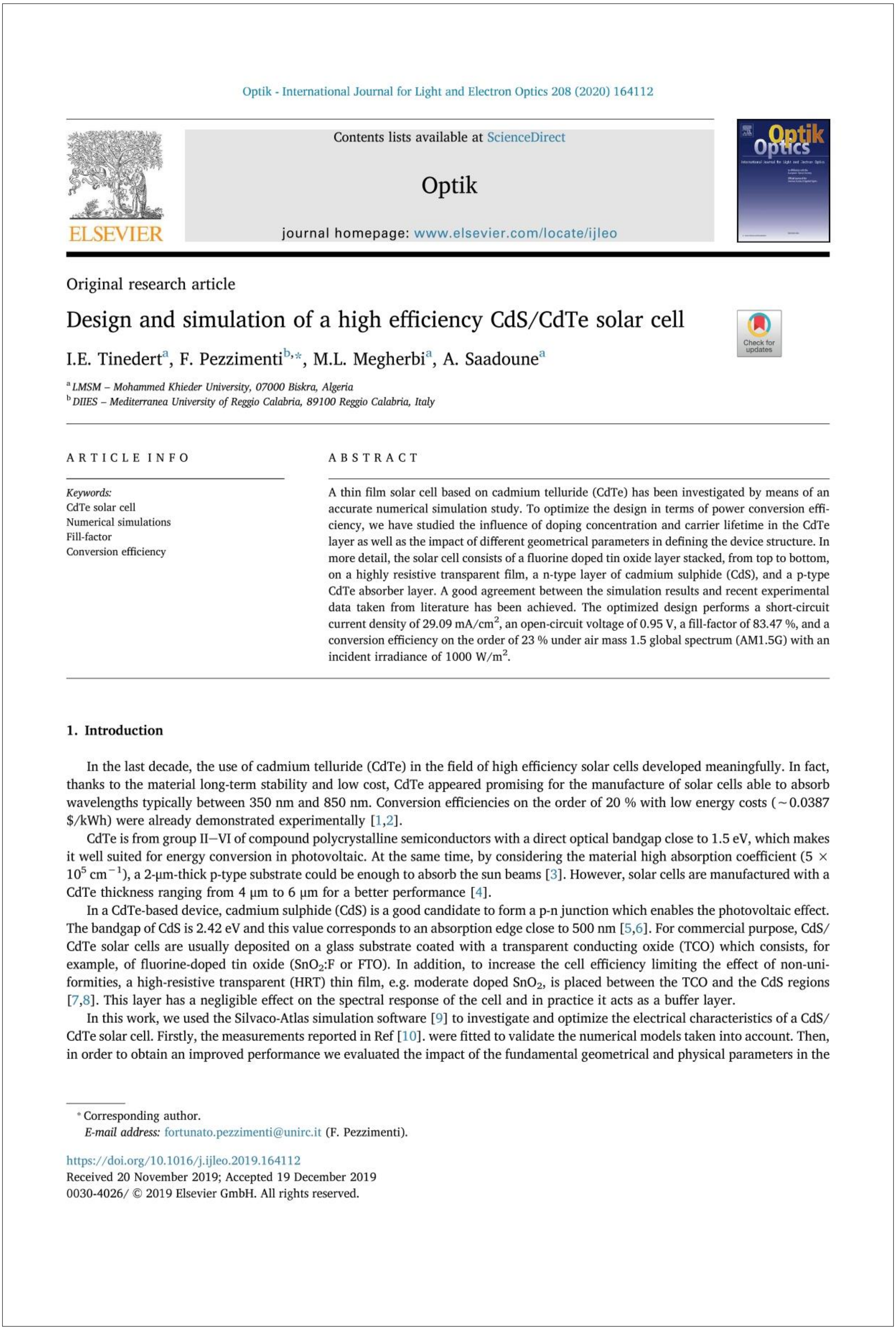

Optik - International Journal for Light and Electron Optics 208 (2020) 164112

Contents lists available at ScienceDirect

Optik

journal homepage: www.elsevier.com/locate/ijleo

Original research article

Design and simulation of a high efficiency CdS/CdTe solar cell

I.E. Tinedert[a], F. Pezzimenti[b,*], M.L. Megherbi[a], A. Saadoune[a]

[a] *LMSM – Mohammed Khieder University, 07000 Biskra, Algeria*
[b] *DIIES – Mediterranea University of Reggio Calabria, 89100 Reggio Calabria, Italy*

ARTICLE INFO

Keywords:
CdTe solar cell
Numerical simulations
Fill-factor
Conversion efficiency

ABSTRACT

A thin film solar cell based on cadmium telluride (CdTe) has been investigated by means of an accurate numerical simulation study. To optimize the design in terms of power conversion efficiency, we have studied the influence of doping concentration and carrier lifetime in the CdTe layer as well as the impact of different geometrical parameters in defining the device structure. In more detail, the solar cell consists of a fluorine doped tin oxide layer stacked, from top to bottom, on a highly resistive transparent film, a n-type layer of cadmium sulphide (CdS), and a p-type CdTe absorber layer. A good agreement between the simulation results and recent experimental data taken from literature has been achieved. The optimized design performs a short-circuit current density of 29.09 mA/cm^2, an open-circuit voltage of 0.95 V, a fill-factor of 83.47 %, and a conversion efficiency on the order of 23 % under air mass 1.5 global spectrum (AM1.5G) with an incident irradiance of 1000 W/m^2.

1. Introduction

In the last decade, the use of cadmium telluride (CdTe) in the field of high efficiency solar cells developed meaningfully. In fact, thanks to the material long-term stability and low cost, CdTe appeared promising for the manufacture of solar cells able to absorb wavelengths typically between 350 nm and 850 nm. Conversion efficiencies on the order of 20 % with low energy costs (~0.0387 $/kWh) were already demonstrated experimentally [1,2].

CdTe is from group II–VI of compound polycrystalline semiconductors with a direct optical bandgap close to 1.5 eV, which makes it well suited for energy conversion in photovoltaic. At the same time, by considering the material high absorption coefficient (5 × 10^5 cm^{-1}), a 2-µm-thick p-type substrate could be enough to absorb the sun beams [3]. However, solar cells are manufactured with a CdTe thickness ranging from 4 µm to 6 µm for a better performance [4].

In a CdTe-based device, cadmium sulphide (CdS) is a good candidate to form a p-n junction which enables the photovoltaic effect. The bandgap of CdS is 2.42 eV and this value corresponds to an absorption edge close to 500 nm [5,6]. For commercial purpose, CdS/CdTe solar cells are usually deposited on a glass substrate coated with a transparent conducting oxide (TCO) which consists, for example, of fluorine-doped tin oxide (SnO_2:F or FTO). In addition, to increase the cell efficiency limiting the effect of non-uniformities, a high-resistive transparent (HRT) thin film, e.g. moderate doped SnO_2, is placed between the TCO and the CdS regions [7,8]. This layer has a negligible effect on the spectral response of the cell and in practice it acts as a buffer layer.

In this work, we used the Silvaco-Atlas simulation software [9] to investigate and optimize the electrical characteristics of a CdS/CdTe solar cell. Firstly, the measurements reported in Ref [10]. were fitted to validate the numerical models taken into account. Then, in order to obtain an improved performance we evaluated the impact of the fundamental geometrical and physical parameters in the

---

[*] Corresponding author.
E-mail address: fortunato.pezzimenti@unirc.it (F. Pezzimenti).

https://doi.org/10.1016/j.ijleo.2019.164112
Received 20 November 2019; Accepted 19 December 2019

جامعة محمد خيضر - بســـكرة ,كلية العلوم و التكنولوجيا ,قسم الهندسة الكهربائية
University Mohamed Khider, Biskra, Faculty of Sciences & Technology
Departement of Electrical Engeneering

ICEEB2018
INTERNATIONAL CONFERENCE
DECEMBER 2-3, BISKRA ALGERIA

Second International Conference on Electrical Engineering,

ICEEB'18

CERTIFICATE OF PARTICIPATION

This is to certify that the paper entitled :

Numerical simulation of the performance of CdTe solar cell using Silvaco Atlas software

has been presented at the ICEEB'18

Authors : Imad Eddine Tinedert and Achour Saadoune

Pr. Mohamed Boumehraz
General Chair ICEEB'2018

رئيس الملتقى الدولي الثاني للهندسة الكهربائية
بومهراز محمد

December 2-3, 2018, Biskra, Algeria